Department of Physics and Astronomy
University of Canterbury, Private Bag 4800
Christchurch, New Zealand

PHYS 690 MSc Thesis

submitted in partial fulfilment of the requirements for

The Degree of Master of Science in Physics

Inhomogeneous Cosmological Models and the Cosmic Microwave Background

---

by

Lawrence H. Dam

Supervisor: Prof. David L. Wiltshire

2016

Contents

Acknowledgements

I would like to thank my supervisor, Prof. David Wiltshire, for his guidance and the huge amount of help he has offered in the execution of this thesis. His comments and suggestions are greatly appreciated. I would also like to thank Krzysztof Bolejko for help in the technical aspects relating to the numerical code. Thanks are also due to Asta Heinesen for her help in the proof reading of this thesis.

Abstract

The cosmic microwave background (CMB) dipole, measured in the heliocentric frame, is conventionally attributed entirely to a local Lorentz boost. However, recent work [1] suggests the CMB dipole may have a non-kinematic component arising from local expansion gradients in space, or *relativistic differential expansion*. In this thesis we examine the possibility of a non-kinematic dipole component using exact inhomogeneous cosmological models that naturally give rise to this notion of differential expansion. In particular, we investigate the spherically symmetric Lemaître-Tolman-Bondi (LTB) model describing a local void and a less symmetric Szekeres model describing both a void and a neighbouring overdense structure. We derive analytic formulae to estimate the non-kinematic dipole and find a non-kinematic component of $-0.12 \pm 0.22\,\mathrm{mK}$. As yet, a precise determination of a non-zero non-kinematic dipole is not possible given current measurements of the boost velocity of the heliocentric frame relative to the Local Group (LG) frame. We further characterise the extent to which observers in a local void, described by the LTB model, will see secondary effects attributed to a Lorentz boost, namely the aberration and modulation effects. We find that similar effects do arise for observers in the LTB model and therefore such effects are not unique to a Lorentz boost.

Chapter 1

Introduction

Unlike fields such as high-energy particle physics, in which theories can be tested in the lab, cosmology relies solely on observations of the universe. It can perhaps be said that the universe itself *is* the lab. The nature of cosmology means that data comes to us primarily from electromagnetic observations,[1] whether of type Ia supernovae (SNe Ia), Cepheid variable stars, luminous red galaxies or the cosmic microwave background (CMB) radiation. It is remarkable how much our understanding of the universe has changed in the last 20 years by merely looking out into the universe. For these reasons, it is essential that the universe is accurately modelled in order to reflect the way photons propagate in the realistic lumpy universe, as this ultimately determines how one interprets the data and what conclusions one draws.

1.1 The standard model of cosmology

At the time of decoupling approximately 380,000 years after the big bang, when photons began their transit through the universe mostly uninterrupted, the primordial plasma is thought to have been very homogeneous. This assumption, which is justified by the highly uniform CMB,[2] suggests that the universe was well described by a spatially homogeneous and isotropic Friedmann-Lemaître-Robertson-Walker (FLRW) model, a solution to the Einstein equations that treats the plasma as a perfect fluid. However, the fact that the universe was not *exactly* homogeneous is crucial. Slight inhomogeneities in the cosmic fluid formed the 'seeds' that developed through gravitational instability into the various structures we see today. The spatially homogeneous and isotropic FLRW background geometry, with initial metric perturbations, and their growth—often treated with Newtonian N-body simulation—together constitute the current *standard model of cosmology*.

[1] Astrophysical neutrinos [2] and gravitational waves [3] provide alternative windows on the universe, which are likely to dramatically change the range of physical phenomena accessible to observations in the coming decades.

[2] Deviations from isotropy occur at a level of 1 part in 100,000 when the CMB dipole has been subtracted.

The FLRW geometry is conveniently written in comoving coordinates,

$$\mathrm{d}s^2 = -\,\mathrm{d}t^2 + a^2(t)\left[\frac{\mathrm{d}r^2}{1-kr^2} + r^2\,\mathrm{d}\Omega^2\right], \tag{1.1}$$

in terms of a single cosmic scale factor, $a(t)$, where $k = -1, 0, 1$ is the spatial curvature and $\mathrm{d}\Omega^2$ is the metric on a 2-sphere. Independently of the energy-momentum tensor, the luminosity distance relation of any FLRW cosmology, can be Taylor expanded at low redshifts to give [4]

$$d_L(z) = \frac{c}{H_0}\left\{z + \frac{1}{2}\left[1-q_0\right]z^2 - \frac{1}{6}\left[1 - q_0 - 3q_0^{\,2} + j_0 + \frac{kc^2}{H_0^{\,2}a_0^{\,2}}\right]z^3 + \mathcal{O}(z^4)\right\} \tag{1.2}$$

where d_L is the luminosity distance to the observed galaxy; $a_0 = a(t_0)$ is the value of the scale factor at the present epoch[3], t_0; and $H_0 = H(t_0)$, $q_0 = q(t_0)$ and $j_0 = j(t_0)$ are respectively the present values of the Hubble parameter, deceleration parameter and jerk parameters, which are defined in general by

$$H(t) \equiv \frac{1}{a}\frac{\mathrm{d}a}{\mathrm{d}t}\,, \tag{1.3}$$

$$q(t) \equiv \frac{-1}{aH^2}\frac{\mathrm{d}^2a}{\mathrm{d}t^2}\,, \tag{1.4}$$

$$j(t) \equiv \frac{1}{aH^3}\frac{\mathrm{d}^3a}{\mathrm{d}t^3}\,. \tag{1.5}$$

Note: the deceleration parameter is positive if the Universe is decelerating, and negative if it is accelerating. In what follows, distances will be defined in units h^{-1}Mpc, where h is a dimensionless parameter related to the Hubble constant by $H_0 = 100\,h\,\mathrm{km\,s^{-1}\,Mpc^{-1}}$.

In the current paradigm, the background FLRW geometry is a solution to Einstein's equations with a spatially homogeneous isotropic perfect fluid consisting of two 'dark' components: non-relativistic 'cold' dark matter (CDM) made up of unknown non-baryonic particles that have yet to be directly detected, and dark energy in the form of a positive cosmological constant Λ (the simplest of dark energy proposals). There are four main, independent probes one uses to constrain this FLRW model:

1. the luminosity distance-redshift relation of SNe Ia ('standard candles'), and to a lesser extent, gamma ray bursts using various empirical correlations;

2. anisotropies in the CMB as measured by the *Wilkinson Microwave Anisotropy Probe* (*WMAP*) [5] and *Planck* satellite [5, 6];

3. baryon acoustic oscillations (BAO) seen through spatial correlations in the galaxy field ('standard rulers');

[3] In what follows we will choose units with $a_0 = 1$.

4. large-scale galaxy clustering.

In the context of the FLRW model, these observations indicate that the universe at the present epoch is (i) undergoing accelerated expansion, (ii) almost spatially flat, and (iii) its energy density consists of approximately 70 % dark energy, 25 % dark matter and 5 % baryonic matter. This is the standard ΛCDM model of cosmology, or the concordance model, offering the broadest and most in-depth picture of the universe.

The extent to which individual datasets, such as SNe Ia, support these observations involve matters of some debate [7] given unknown systematic uncertainties. Furthermore, there are various tensions between different datasets [8] and the particular problem of the primordial lithium abundance, which is anomalous at the $5.3\,\sigma$ level [9], unless new particles such as decaying gravitinos are assumed [10] or improvements in the determination of observational systematics from the measurement of light element abundances are made. Nonetheless, at present the ΛCDM model has been successfully tested against more datasets than any other model.

1.1.1 The dark energy problem

The first compelling evidence for cosmic acceleration came[4] from interpreting the luminosity distance-redshift relation of distant ($z \sim 0.5$) supernovae [12, 13]. Prior to these seminal papers, the universe was thought to be matter dominated, possibly open[5] and decelerating due to the universal attraction of gravity. However, supernovae appeared fainter than expected from a such a cosmology—possible if the expansion of the universe is accelerating. With the data instead favouring a universe with a cosmological constant, cosmologists now had to reckon with the knowledge that the energy density of the present universe is ostensibly dominated by dark energy.

Despite the success of the standard model, there are still major theoretical issues to be resolved. In particular, the precise nature of dark energy, which appears to dominate the energy density and drive the recent accelerated expansion of the universe, is not well understood. The inclusion in the standard model without any direct evidence of an exotic substance that violates the strong energy condition[6] has led to many other proposals. A

[4]Over time the direct evidence for cosmic acceleration from supernovae alone has not improved to become decisive, as was noted in the mid-2000s [7, 11].

[5]By the early 1990s there was considerable observational evidence [14,15] for a matter density parameter $\Omega_{m0} \simeq 0.2 \pm 0.1$. In the context of FLRW models this meant that either the universe was negatively curved, or that there was a cosmological constant—a possibility favoured by some [14], given that a total energy density parameter close to unity was theoretically preferred from the inflationary universe paradigm. Direct evidence for spatial curvature being close to zero only arrived with the measurement of the angular scale of the first acoustic peak in the CMB anisotropy spectrum by BOOMERANG in 2000 [16].

[6]Ordinary self gravitating matter which clusters gravitationally (whether baryonic or CDM) satisfies the strong energy condition $w > -1/3$. A cosmological constant has negative pressure with $p = -\rho$, saturating the dominant energy condition $p = w\rho$, with $-1 \leq w \leq 1$. "Phantom energy" with $w < -1$ would violate known physical laws such as causality and is pathological [17] (if assumed to be a fluid in the

brief survey of recent `arXiv` postings reveals a range of alternative theories including the existence of scalar fields (so-called quintessence); modifications to general relativity on cosmological scales such as $f(R)$ gravity, massive gravity etc. (See the review [18]; for a critique on the status of dark energy see [19, 20]).

If dark energy is a cosmological constant then the question of why it takes a particular value represents a fine-tuning problem, which can only be resolved by invoking the anthropic principle [21]. However, the cosmic coincidence problem still remains: namely why is the value of Ω_Λ comparable to Ω_m just at the present epoch so that cosmic acceleration started only recently, and is not yet dominant?

1.1.2 Overview of the CMB

The cosmic microwave background (CMB) radiation is the most important observational evidence justifying use of the FLRW geometry. It is also one of the most important tools in cosmology today providing a glimpse into the early universe. The CMB is a relic of the big bang—radiation that can be directly traced back to the time of *recombination* when photons, baryons and leptons formed a hot dense plasma generally known as the *baryon-photon plasma*. The plasma was opaque due to Thomson scattering of photons from free electrons (and also protons and helium nuclei to a lesser extent). When protons and electrons combined to form neutral atoms, the rate of scattering dropped to a point that photons could stream freely throughout space. This time is called *freeze out* and the interval between the time of recombination and freeze out is known as *last scattering*.

The CMB is a near ideal blackbody spectrum, perhaps one of the best examples in nature. Furthermore, the spectrum is isotropic over the sky with a mean temperature $T_0 = 2.7255\,\mathrm{K}$ [22] that is uniform to a few parts in 100,000, indicating that the entire observed universe was in thermal equilibrium at the epoch of last scattering. Since scales greater than roughly one degree apart cannot have been in causal contact in FLRW models with ordinary matter and radiation this leads to the *horizon problem* of the standard cosmology, which is usually circumvented by introducing primordial scalar fields and gives an epoch of inflation at very early times [23].

Inflation is also generically assumed to stretch an initial spectrum of density perturbations to arbitrarily large scales, giving rise to an almost scale-free matter spectrum by the epoch that inflation ceases during a period of reheating to subsequent radiation domination. The potential wells generated by these density perturbations on the surface of last scattering give rise to additional redshifts and blueshifts that generate anisotropies in the blackbody spectrum we observe. Indeed, it is these highly revealing anisotropies

energy–momentum tensor), but is often considered for parameter constraints neglecting its fundamental origin. Physically non-pathological dark energy requires an equation of state with $-1 \leq w \leq -1/3$, while $w \simeq -1$ is found by many observational tests.

that have provided a great deal of information about the early universe essential to the precise determination of cosmological parameters.

There are two types of anisotropies: (i) primary anisotropies that have their origin before the time of recombination and are therefore related to the physics of the early universe and, (ii) secondary anisotropies that are generated after recombination when structure began to form. Processes that can cause secondary anisotropies include inverse Compton scattering in ionised gas associated with cosmic structures (or the Sunyaev-Zel'dovich effect), weak gravitational lensing, and the integrated Sachs Wolfe (ISW) effect, which we will discuss further in chapter 2.

1.1.3 The CMB dipole

In order to investigate the primary and secondary anisotropies, it is first necessary to subtract the CMB dipole, which is the largest contribution to the CMB anisotropy with a magnitude [24] of

$$3.3645 \pm 0.0020\,\mathrm{mK}, \tag{1.6}$$

in the direction

$$(l, b) = (263.99^\circ \pm 0.14^\circ, 48.26^\circ \pm 0.03^\circ), \tag{1.7}$$

as measured in the heliocentric frame. By comparison the primordial CMB fluctuations are two orders of magnitude smaller, (i.e. $\sim 10\,\mu\mathrm{K}$).

The large dipole in the CMB is usually attributed to the peculiar velocity of the solar system barycentre relative to the CMB rest frame, i.e., the frame in which the CMB appears most isotropic. In this thesis we will examine the light propagation in inhomogeneous solutions of Einstein's equations in which this assumption is revisited. It is therefore first important to understand the effect of a boost on the CMB blackbody spectrum in the standard FLRW model.

There are also two secondary effects on the observed CMB sky, associated with a local Lorentz boost. These are the *aberration* and *modulation effects*. Both are special relativistic effects related to how objects appear to boosted observers, e.g., in transforming between the CMB and heliocentric rest frames. The aberration effect is the phenomenon that shifts the observed direction of light rays towards the direction of the boost. This effect is well-known in popular culture: space ships moving at relativistic speeds see a convergence of light rays in the direction of travel, with light that would otherwise not be seen coming into the field of view. The sky in the direction of the boost appears more squashed together, while the opposite side appears more stretched out.

The boost direction divides the sky into two hemispheres. For the hemisphere that the observer is moving towards, the magnitude of the CMB fluctuations increases, while on the other hemisphere it decreases. Thus, hot (cold) spots appear hotter (cooler) on

one hemisphere, while hot (cold) spots appear cooler (hotter) on the other (see fig. 1.1). This is known as the modulation effect.

Suppose an observer $\mathcal{O}$ sees a photon in the sky arriving from the direction $\hat{\boldsymbol{n}}$ with frequency ν. According to such an observer, the photon has a 4-momentum $p^\mu = E(1, -\hat{\boldsymbol{n}})$ with energy $E = h\nu$. Another observer, $\mathcal{O}'$, boosted with respect to $\mathcal{O}$, will measure a 4-momentum $p'^\mu \equiv E'(1, -\hat{\boldsymbol{n}}') = \Lambda^\mu{}_\nu\, p^\nu$ with

$$\Lambda^\mu{}_\nu = \begin{pmatrix} \gamma & -\gamma\boldsymbol{\beta}^T \\ -\gamma\boldsymbol{\beta} & I + (\gamma-1)\hat{\boldsymbol{\beta}}\hat{\boldsymbol{\beta}}^T \end{pmatrix}, \qquad \boldsymbol{\beta} = (\beta_x, \beta_y, \beta_z). \tag{1.8}$$

Here $\hat{\boldsymbol{\beta}} = \boldsymbol{\beta}/\beta$, $\gamma = (1-\beta^2)^{-1/2}$ is the Lorentz factor and $\beta = |\boldsymbol{\beta}| = v/c$ the boost parameter. Evaluating the transformation $\Lambda^\mu{}_\nu\, p^\nu$ results in two equations. The first is the well known Doppler shift

$$\nu' = \gamma(1 + \boldsymbol{\beta}\cdot\hat{\boldsymbol{n}})\nu, \tag{1.9}$$

while the second

$$\hat{\boldsymbol{n}}' = \frac{\hat{\boldsymbol{n}} + [\gamma\beta + (\gamma-1)\hat{\boldsymbol{\beta}}\cdot\hat{\boldsymbol{n}}]\hat{\boldsymbol{\beta}}}{\gamma(1+\boldsymbol{\beta}\cdot\hat{\boldsymbol{n}})}, \tag{1.10}$$

gives the relativistic *aberration effect*, whereby boosted observers measure photons arriving in directions shifted (or aberrated) relative to an unboosted observer.

Although the above formulae relate quantities in the unboosted frame to the boosted frame, it turns out to be more convenient to write the measured frequency ν' in terms of $\hat{\boldsymbol{n}}'$, since this is what will be measured. To do this we apply an equivalent boost in the opposite direction, that is, we undo the original boost. Observe that

$$\nu' \quad \longrightarrow \quad \gamma(1-\boldsymbol{\beta}\cdot\hat{\boldsymbol{n}}')\nu' = \gamma^2(1-\boldsymbol{\beta}\cdot\hat{\boldsymbol{n}}')(1+\boldsymbol{\beta}\cdot\hat{\boldsymbol{n}})\nu. \tag{1.11}$$

Projecting (1.10) onto $\boldsymbol{\beta}$ (i.e. taking the dot product $\boldsymbol{\beta}\cdot\hat{\boldsymbol{n}}'$) and some simple algebra we of course find

$$\gamma^2(1-\boldsymbol{\beta}\cdot\hat{\boldsymbol{n}}')(1+\boldsymbol{\beta}\cdot\hat{\boldsymbol{n}}) = 1. \tag{1.12}$$

Rearranging (1.11) we obtain the Doppler shift in terms of the direction the boosted observer actually measures:

$$\nu' = \frac{\nu}{\gamma(1-\boldsymbol{\beta}\cdot\hat{\boldsymbol{n}}')}. \tag{1.13}$$

Indeed, since $T'/T = \nu'/\nu$ we can rewrite in terms of temperature as

$$T'(\hat{\boldsymbol{n}}') = \frac{T(\hat{\boldsymbol{n}})}{\gamma(1-\boldsymbol{\beta}\cdot\hat{\boldsymbol{n}}')}. \tag{1.14}$$

This is one of the main equations we will be using in later sections. We can go one step further and write unboosted blackbody temperature $T(\hat{\boldsymbol{n}})$ in terms of $\hat{\boldsymbol{n}}'$, that is, we will need to invert (1.10). However, based on symmetry considerations this is just

$$\hat{\boldsymbol{n}} = \frac{\hat{\boldsymbol{n}}' - [\gamma\beta + (\gamma-1)\hat{\boldsymbol{\beta}}\cdot\hat{\boldsymbol{n}}]\hat{\boldsymbol{\beta}}}{\gamma(1-\boldsymbol{\beta}\cdot\hat{\boldsymbol{n}})}, \tag{1.15}$$

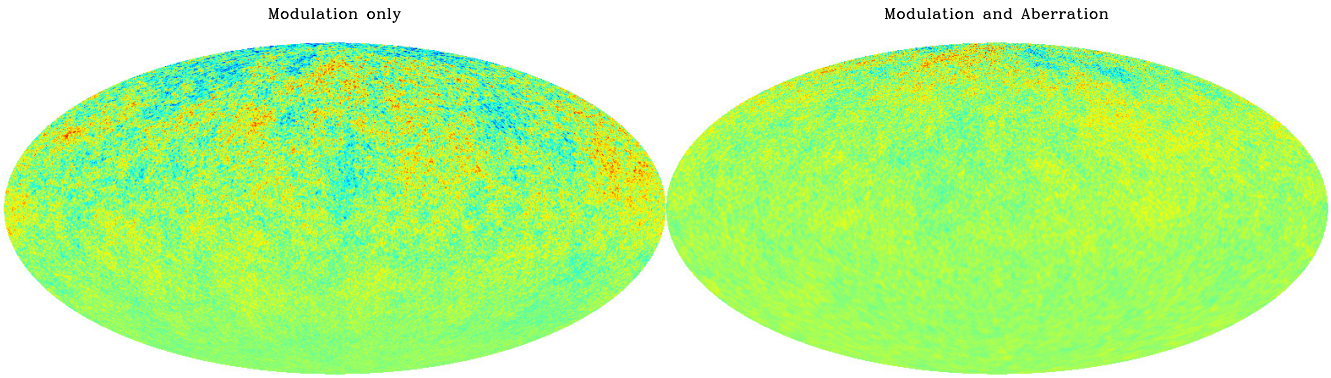

Figure 1.1: Modulation and aberration effects for a boost along the z-axis (exaggerated for effect with $\beta = 0.8$). In reality the effects are much more subtle.

i.e., we replace $\boldsymbol{\beta} \to -\boldsymbol{\beta}$. We emphasise the above equations are entirely general, applying to any blackbody spectrum and, naturally, there is no better example of a blackbody than the CMB. We thus turn our attention to the CMB dipole and secondary effects as it relates to a Lorentz boost.

We begin with the simplest case of an isotropic temperature field $T(\hat{\boldsymbol{n}}) = T_0 = 2.7255\,\mathrm{K}$. It is commonly assumed the dipole in the heliocentric frame is entirely the result of a boost $\beta = 1.23 \times 10^{-3}$, or $v = \beta c = 369\,\mathrm{km\,s^{-1}}$, relative to the CMB rest frame. The small boost permits a Taylor expansion:

$$\begin{aligned} T'(\hat{\boldsymbol{n}}') &= T_0 \left(1 + \boldsymbol{\beta}\cdot\hat{\boldsymbol{n}}' + (\boldsymbol{\beta}\cdot\hat{\boldsymbol{n}}')^2 - \frac{1}{2}\beta^2 + \mathcal{O}(\beta^3)\right) \\ &\approx T_0(1 + \boldsymbol{\beta}\cdot\hat{\boldsymbol{n}}') \end{aligned} \tag{1.16}$$

Clearly, a boost induces a dipole on the CMB (along with a small quadrupole etc). Including primordial fluctuations $\delta T(\hat{\boldsymbol{n}}')$ so that $T'(\hat{\boldsymbol{n}}') = T_0 + \delta T(\hat{\boldsymbol{n}}')$, (1.16) to linear-order becomes

$$\begin{aligned} T'(\hat{\boldsymbol{n}}') &\approx (T_0 + \delta T(\hat{\boldsymbol{n}}'))(1 + \boldsymbol{\beta}\cdot\hat{\boldsymbol{n}}') \\ &= T_0 + T_0\,\boldsymbol{\beta}\cdot\hat{\boldsymbol{n}}' + (1 + \boldsymbol{\beta}\cdot\hat{\boldsymbol{n}}')\,\delta T(\hat{\boldsymbol{n}}') \end{aligned} \tag{1.17}$$

The first and second terms are of course just the monopole and dipole respectively; the third term represents a modulation in $1+\boldsymbol{\beta}\cdot\hat{\boldsymbol{n}}'$, and also an aberration, since the observed direction $\hat{\boldsymbol{n}}'$ will be related to $\hat{\boldsymbol{n}}$ through (1.10). The two effects are shown in fig. 1.1 for a map generated using an underlying *Planck* best-fit power spectrum. The modulation effect can be seen to amplify anisotropies on one side of the sky, making hot fluctuations hotter and cold fluctuations colder, while doing the opposite on the other side of the sky. Also notice the stretching and squashing in the lower and upper hemispheres respectively, from photons being aberrated towards the boost direction.

1.1.4 Structure formation in the standard model

The standard model approach to structure formation is based on cosmological perturbation theory (which we discuss further in chapter 2). The Einstein equations are solved 'order-by-order', in that the zeroth-order equations are just the background Friedmann equations—preserving the FLRW dynamics—while the first-order equations govern the evolution of large-scale structure on the fixed FLRW background. As such, the first-order perturbations do not modify the background expansion rate, implying no backreaction. Put another way, the inhomogeneities do not "inform" the average cosmic evolution.

On large scales, one speaks of the *linear regime*, when fluctuations are small in amplitude and the growth is linear. However, implicit in this is a notion of averaging as one assumes that the local density, when averaged over sufficiently large scales, is close to the background density with the fluctuations represented by small perturbations.[7] On small scales ($\lesssim 10\,\mathrm{Mpc}$) the density can differ significantly from the uniform background density as here one finds structures such as galaxies ($\delta_\rho \sim 10^5$) and near-empty voids ($\delta_\rho \sim -1$). It is on these scales that linear perturbation theory breaks down and one enters the *nonlinear regime*. In the standard model, one then resorts to Newtonian N-body simulations [26], in which gravitational clustering is Newtonian and the evolution of perturbations is tracked against the rigidly expanding FLRW background. In this framework, the crucial assumption is that the small scale dynamics break away from the evolution of the background.

Although a FLRW model with first-order perturbations and linear evolution seems to be a reasonable approximation of the universe at high redshifts, the late universe is evidently very inhomogeneous, having since transitioned from the linear regime to the highly nonlinear regime of structure formation. The effects of small-scale structure on large-scale structure is precisely the issue of backreaction. Is it possible that the average cosmic expansion has since departed from the standard FLRW evolution?

While perturbation theory allows a semi-analytical approach to structure formation, there is no substitute for full, nonlinear general relativity. Using exact solutions with no approximations one can study the nonlinear regime, and in particular, the effect these structures have on light propagation.

1.2 The cosmic web

At late times matter is no longer smoothly distributed in a fluid-like continuum, as had been the case at decoupling, but is instead locked up in regions of virialised structure. Galaxies and clusters of galaxies are found to form sheets, filaments and knots, that surround and thread large void regions, forming a complex cosmic web [27, 28]. The

[7] There is also a notion of smoothing scale involved in specifying the local density of matter [25].

voids dominate the late epoch Universe by volume [29], and often have density contrasts, $\delta_\rho \equiv (\rho - \overline{\rho})/\overline{\rho}$, relative to the background density, $\overline{\rho}$, that are not much larger than the minimum $\delta_\rho = -1$ corresponding to complete emptiness. Furthermore, the void distribution also has characteristic scales, with voids of a typical diameter $30h^{-1}$Mpc and visible matter[8] density contrast $\delta_\rho \lesssim -0.94$ alone accounting for $\sim$40 % of the volume of the present epoch Universe [34, 35].

This leads to a vastly more complex picture of the late epoch Universe than in the early Universe. It potentially demands a more sophisticated cosmological model than a homogeneous and isotropic solution of Einstein's equations will allow. Whether the universe rigidly evolves in a FLRW-like manner—preserving uniform spatial curvature—at late times is far from obvious. The fluid approximation breaks down, as soon as the geodesics of the initial particles cross to form condensed matter concentrations, and the distribution of matter can only be considered homogeneous and isotropic in some statistical or averaged sense, once we coarse grain over all the virialised galaxy clusters. Despite this, the current paradigm of cosmology makes the implicit assumption that the FLRW metric continues to hold on all cosmologically relevant spatial scales.

1.2.1 Light propagation and the lumpy universe

If we retain an average expansion governed by the FLRW geometry, but try to embed more realistic nonlinear structures such as voids and matter overdensities within the FLRW geometry, then it turns out that the average effect of light propagation through such structures can differ from light propagation on the average background. Light originating from low redshift sources traverses mainly underdense regions and implies important consequences on supernovae observations.

A typical beam size, (i.e., the cross-section of a light-ray bundle) of SNe Ia is narrow. For example, an observation of SNe Ia at $z \sim 1$, have an angular size of about 10^{-7} arc seconds [36]. This is much smaller than the typical distance between objects the beam might encounter, such as stars, galaxies, hydrogen clouds etc. Beams of this size tend to propagate in regions where the local density is lower than the cosmic average. On these scales the perfectly smooth cosmic fluid fails to capture the relevant physics, even in some average sense. Thus, light does not necessarily propagate in a FLRW manner, or for that matter, according to the average model, but is affected by local matter inside

[8]These density contrasts are based on the galaxy-galaxy correlation function and do not probe dark matter directly. However, dark matter and baryonic matter are highly correlated in models of structure formation and so the galaxy population has to be very significantly biased if this density contrast δ_ρ determined from galaxy surveys is to deviate strongly from the overall contrast including dark matter. One can fit lensing profiles to voids including dark matter to obtain lower density contrasts, e.g. $\delta_\rho \sim -0.4$ [33]. However, this is of course a fit to the ΛCDM model rather than a direct measurement. Comparisons of void statistics to N-body simulations is a test of the ΛCDM model. However, given the astrophysical uncertainties, this is a subject of ongoing debate [30–32] that will take decades of future observations to resolve.

and outside the beam path.

Light propagation in a lumpy universe need not have the same average behaviour as a completely uniform medium since the size of the beam may not sample under and overdense regions in equal measure [37]. How matter affects beams depends on whether it is inside or outside the beam. A beam which encounters very little matter will undergo a different kind of focusing related to the Weyl curvature as compared to a beam that propagates in smoothed out continuum of matter, which is related to the Ricci curvature. Indeed, the Weyl curvature vanishes in the standard model, so that distortion and magnification effects associated with inhomogeneous mediums are absent. This idea was first pointed out by Zel'dovich [38] for the special case of light propagation in a vacuum and then generalised by Dyer and Roeder to beams partially filled with matter [39]. Recent studies show that this underdense 'selection effect' results in a shift in the Hubble diagram as well as introducing dispersion [36, 40, 41].

1.2.2 Non–Copernican solutions to the dark energy problem

Another alternative in general relativistic approaches to inhomogeneous cosmology, which takes an opposite extreme to the small scale nonlinear inhomogeneities in a FLRW background discussed in Section 1.2.1, is to consider exact inhomogeneous solutions of the Einstein equations with dust as background solutions for the whole Universe in the epoch of matter domination. Given the evidence of the CMB that anisotropies are small, the only solution that can be practically used in these circumstances is the spherically symmetric Lemaître-Tolman-Bondi (LTB) model [42–44]. This model contains a spherically symmetric inhomogeneous dust source, $\rho(t, r)$, and scale factor $R(t, r)$, and a varying spherically symmetric spatial curvature function, $E(r)$, on the spatial hypersurfaces formed by observers comoving with the dust. These parameters are defined in detail in Section 3.1, as we will study the same solutions as models for small scale inhomogeneities (rather than models of the whole late epoch Universe) in Chapters 3 and 4.

Given that there are two free functions in the LTB model it is possible to solve the Einstein equations for a given present epoch dust profile $\rho(t_0, r)$ so as to fit a huge class of luminosity distance–redshift relations. Indeed, one can readily match SNe Ia data [12, 13] even *without* a cosmological constant [45, 46], even better than any FLRW model with $\Lambda \geq 0$. While large voids, with radii of hundreds of Mpc are typically assumed [45, 46], the model that fits best actually has a hump in the density profile [47].

This is an interesting toy model, as it shows that cosmological data for the average expansion history can be accounted for just as well as in FLRW models. As a realistic solution to the dark energy problem, however, this scenario encounters two significant problems. Firstly, in order to fit supernova data, observers must be placed very near the origin of spherical symmetry, which is implausible in view of the Copernican principle. Secondly, the inhomogeneity has to be very large—e.g., a void or underdensity of

hundreds of megaparsecs—and there is no reasonable theory of structure formation that would produce such large structures consistently with the observed small temperature fluctuations at last scattering [48].

1.2.3 Backreaction of inhomogeneities

Another potential solution to the dark energy problem is to demand consistency with observations, but to reconsider the role of small scale inhomogeneities on average cosmological dynamics, by revisiting the assumptions of the standard model. (See the reviews [19, 25, 49–52] and references therein.) This is a considerably more conservative approach to address the dark energy problem than many alternative theories that either invoke new fundamental fields that have never been observed, or new physics from modifications to the gravitational action, making radical departures from well-tested theories. The use of the FLRW metric is argued to be an oversimplification, with the appearance of dark energy in the standard model merely a phenomenological artefact necessary to fit observations. The basic question this approach seeks to answer is: "How do inhomogeneities in matter and geometry affect the average cosmological dynamics of the universe?" This idea is known as *cosmological backreaction*.

In contrast to the standard model that takes the FLRW metric as the starting point for the averaged universe, in one widely used backreaction approach one constructs the averaged model using an explicit scalar averaging formalism [53, 54].

The Einstein equations are not assumed to hold on arbitrarily large scales, but only on small scales. From first principles, if the Einstein equations are assumed to be causal evolution equations then there is no *a priori* reason why they should hold when averaged on spatial scales larger than those that light and gravitational waves have had time to propagate on. Furthermore, the rest-energy density of non-relativistic particles dominates over the rest-energy density of radiation at late epochs on the right-hand side of Einstein's equations. There is also no *a priori* reason for the average of the small scale Einstein equation to remain an exact solution of the same equations when averaged over spatial scales on which non-relativistic matter propagates.

Fundamental issues arise as to the scale over which matter and geometry can be considered to be coupled by the Einstein equations when taking averages. Because of the nonlinearity of the Einstein field equations the order we average and evolve the system is important, i.e., they do not commute. By averaging the scalar parts of the field equations an analogue of the Friedmann equations can be derived, with the variables being quantities averaged over a spatial domain. The non-commutativity results in an extra term, the *kinematical backreaction scalar*, which taken at face value, could be seen as a way to potentially mimic the effects that are usually attributed to dark energy.

The extent to which backreaction plays a role in cosmology has been the subject of debate [55–58]. Green and Wald [56–58] have proven a result that, assuming average

evolution is an exact solution of Einstein's equations on any spatial scale, then backreaction effects are negligible, within a particular mathematical framework with additional assumptions. While Buchert et al. [55] disagree about the generality of these mathematical assumptions, both sides of the debate agree that the Green-Wald theorem does not apply to the scalar averaging approach of Buchert, since this does not assume that average evolution is an exact solution of Einstein's equations.[9]

It is nonetheless true that since Buchert's formalism is a statistical one, extra physical ingredients are required to relate local observations to statistical quantities, for example in relation to the time parameter appearing in the averaging formalism as compared to time parameters of individual observers. Since the inference of cosmic acceleration involves two time derivatives this is a crucial point. Ishibashi and Wald [60] raised such concerns already in 2006. Wiltshire's timescape model [61] aims to address such concerns, via an additional principle, the *cosmological equivalence principle* [62], which is applied to relate local observables to the Buchert averages.

1.2.4 The scale of statistical homogeneity

An in depth view of the present universe reveals one that is dominated in volume by voids [29,34,35] and is very much inhomogeneous on the small scales of galaxies and galaxy clusters. Only when averaged over large scales does the universe exhibit some notion of homogeneity. The transition between the "small" and the "large" scales demarcates the scale of statistical homogeneity [63–66], and is important in any phenomenologically successful model of backreaction.

There is no universally agreed definition of a statistical homogeneity scale. Generally one must interpret observations in terms of spatial averages of the density field, related mathematically to an average on a compact domain of a spatial hypersurface, Σ_t, according to

$$\langle \rho(t) \rangle_{\mathcal{D}_R} = \frac{1}{\mathcal{V}(t)} \left(\int_{\mathcal{D}_R} \mathrm{d}^3x \sqrt{\det {}^3g}\, \rho(t, \mathbf{x}) \right), \tag{1.18}$$

where $\mathcal{V}(t) \equiv \alpha R^3(t) = \int_{\mathcal{D}_R} \mathrm{d}^3x \sqrt{\det {}^3g}$ is the volume of the domain $\mathcal{D}_R \subset \Sigma_t$, g_{ij}, $(1 \leq i, j \leq 3)$ is the intrinsic metric on Σ_t and α is a dimensionless constant determined by a choice of geometry; e.g., $\alpha = 4\pi/3$ for Euclidean spheres. If the ergodic theorem is assumed to apply, a definition of homogeneity often presupposes the existence of an average positive density, $\rho_0(t)$, defined by the limit

$$\lim_{R(t)\to\infty} \langle \rho(t) \rangle_{\mathcal{D}_R} = \rho_0(t) > 0. \tag{1.19}$$

[9] Green and Wald responded to Buchert et al. [55] with a note [59] in which they redefined the word "backreaction" to refer to the specific setting they address in their own formalism, labelling other approaches which constitute most of the papers in the literature as "pseudo-backreaction". They further clarified that their formalism was "never intended or claimed to apply" to such approaches, and, in particular, that their results "do not apply to the Buchert formalism".

A homogeneity scale, $\lambda_0(t)$, is then defined [67] by the requirement that every point in Σ_t be contained in a domain $\mathcal{D}_{\lambda_0} \subset \mathcal{D}_R$ such that

$$\left|\left\langle \rho(t)\right\rangle_{\mathcal{D}_R} - \rho_0(t)\right| < \rho_0(t), \qquad \forall\ R > \lambda_0. \tag{1.20}$$

In practice, the density field can only be inferred indirectly from the statistical properties of the distribution of galaxies, with all of the systematic issues related to finite sample volumes and observational biases. Thus, any practical measure of statistical homogeneity is not directly based on a relation such as (1.20), but rather on the scale dependence of galaxy–galaxy 2–point correlation functions.

The precise scale is not well defined as the transition to homogeneity is gradual [65]. However, in observational cosmology it is usually assumed in the standard model that the FLRW metric applies below this scale as well.

In this thesis, it is our aim to study the effect on light propagation of fully nonlinear exact solutions of Einstein's equations for inhomogeneities with characteristic scales smaller than the statistical homogeneity scale. In these cases the FLRW metric will not apply on the small scales. We will adopt the most conservative estimate of a statistical homogeneity scale of order $100h^{-1}$Mpc (or redshift $z \sim 0.03$), based on the 2-point galaxy correlation function.

If one were to adopt a strict definition of homogeneity based on convergence (1.19), (1.20). That would, however, require that all higher order N–point galaxy correlation functions also converge, and this has not been observed. In the largest survey volumes that have been studied, the density contrast δ_ρ has been observed to have a standard deviation of 7–8% on the largest spatial scales [63,64]. In models of backreaction in which the average evolution in non–Friedmann, convergence of (1.19), (1.20) would not occur in the observable universe. The statistical homogeneity scale then demarcates between a large scale on which the standard deviation of δ_ρ remains bounded at the present epoch, while being arbitrarily large on small scales [62].

In this thesis, we will not investigate the effects of backreaction and will simply retain an average FLRW model on large spatial scales, to model the average propagation of light for most of its journey to us from the CMB. We will therefore isolate the effect on light propagation of nonlinear inhomogeneities on relative close ($< 100h^{-1}$Mpc) spatial scales, and investigate the differences from the FLRW model.

1.3 Hubble expansion variation as a cosmological probe

As our understanding of the properties of galaxies, clusters, Cepheids, SNe Ia, gamma ray bursters etc, has grown, so too has the observational cosmologist's ability to exploit them as a sensitive probe of the universe. Developments in photometry and spectroscopy, as well as technical advances, has led to a surge in the number of astronomical surveys,

with numerous space observatories launched capable of observing in optical, infrared wavelength bands etc. As a result, astronomers have been able to map the universe in exquisite detail, and chart our local cosmic neighbourhood.

If the early universe consisted of particles in random motion, with the motion of nearby particles uncorrelated, the late universe is characterised by the gravitational collapse of matter. As discussed in Section 1.1, the conventional picture is based on Newtonian gravitational instability theory, set against the backdrop of a rigid FLRW background. The redshift, z, of distant sources, for the case of an observer and source both at rest with respect to the $t=$const hypersurfaces of (1.1), is given by

$$1+z=\frac{a_0}{a(t)}\,. \tag{1.21}$$

More generally, this relation is modified to become

$$(1+z_{\rm obs})=(1+z_{\rm FLRW})(1+z_{\rm Doppler})\,, \tag{1.22}$$

where $z_{\rm FLRW}$ is given by (1.21) and $z_{\rm Doppler}$ incorporates the local Lorentz boosts of both the observer and the source. Provided we can correct for our own local motion, to transform to the *cosmic rest frame*, namely the $t_0=$const hypersurface of (1.1), then in the limit of small redshifts the deviations of the luminosity distance–redshift relation from the leading order linear term of (1.2)—the Hubble law—are treated as *peculiar velocities*,

$$v_{\rm pec}=cz-H_0\,d_L\,. \tag{1.23}$$

In the framework of linear perturbations of the FLRW model discussed in Section 1.1.4, peculiar velocities are considered as Newtonian in character, being caused by the gravitational pull of matter overdensities[10] which deviate from the background. This furnishes a velocity field $\boldsymbol{v}$, which in turn is related to the density perturbation field. In this framework large-scale motions are then probes of the underlying gravitational potential. The Newtonian perturbative framework laid down by Peebles in the 1980s [70] is sometimes used even on scales $< 100h^{-1}$Mpc in which the density perturbations become nonlinear. However, more sophisticated analyses recognise that N–body Newtonian simulations are required to make inferences about the nonlinear regime [71, 72].

1.3.1 The cosmic rest frame and bulk flows

As mentioned in section 1.1.3, in the standard framework the observed CMB dipole referred to the heliocentric frame[11] is assumed to be caused entirely by the motion of the Sun with respect to the $t_0=$const hypersurface of (1.1). The local Lorentz frame in which

[10] In this Newtonian framework, astronomers include components of the velocity field which "push" away from voids [68, 69], which is conceptually challenging given that there is no known fundamental force with this character, Λ being spatially homogeneous.

[11] As expected, the dipole is modulated at parts in 10^4 by the motion of the Earth around the Sun.

the CMB dipole vanishes is thus assumed to be the cosmic rest frame. After taking into account the known motions of the Sun in its orbit within the Milky Way galaxy, and of the Milky Way itself with respect to the barycentre of the Local Group of galaxies—the largest bound structure of which it is a part—one deduces the Local Group (LG) must have a velocity with respect to the CMB frame [68] of

$$635 \pm 38\,\mathrm{km\,s^{-1}} \quad \text{towards} \quad (l, b) = (276.4^\circ, 29.3^\circ) \pm 3.2^\circ, \tag{1.24}$$

which is in the constellation *Hydra*.

Ever since the first accurate determination of the CMB dipole [24] all observations of redshifts have been routinely transformed to the CMB rest frame before performing cosmological measurements. Such measurements include the determination of the luminosity distance–redshift relation [12, 13], cosmological parameters from CMB anisotropies [5, 6], or indeed any cosmological parameter estimates based on relating the redshift to measurements that determine the expansion history in any form.

In the framework of Newtonian perturbation theory, which we will further discuss in the next Chapter, our observed peculiar velocity field (1.23) in the CMB rest frame is expected to be given by

$$\boldsymbol{v}(t_0, \boldsymbol{r}) = \frac{H_0 \Omega_{M0}^{0.55}}{4\pi} \int \delta_\rho(\boldsymbol{r}') \frac{\boldsymbol{r} - \boldsymbol{r}'}{|\boldsymbol{r} - \boldsymbol{r}'|^3} \mathrm{d}^3\boldsymbol{r}'. \tag{1.25}$$

at the present epoch in the case of a spatially flat FLRW model with nonzero Λ, where $\Omega_{M0} = 8\pi G\rho_{M0}/(3{H_0}^2)$ is the present epoch matter density parameter, i.e., the ratio of the matter density to the critical density. (See §2.1.2 for further discussion.) There are two important expectations of this analysis:

(1) The magnitude and direction of the peculiar velocity (1.24) of the Local Group are numerically consistent with an observed *clustering dipole* of the nearby peculiar field determined by (1.25), or nonlinear extensions thereof, once the effects of all mass perturbations in our vicinity are accounted for.

(2) The spherical *average* of the peculiar velocity field (1.25) should tend to zero at very large distances, consistent with a stochastic field of peculiar velocities whose amplitude is determined from realistic Newtonian N–body simulations.

The study of cosmic flows in this framework has led to sometimes confusing and conflicting claims in its 40 year history, and both of the points above are the subject of ongoing debate. In particular, a significant dipolar moment in the local velocity field, or *bulk flow* velocity, is observed to extend out to $\gtrsim 300\,\mathrm{Mpc}$, beyond the $\sim 100h^{-1}\mathrm{Mpc}$ scale of statistical homogeneity. Such an unexpected large-scale coherent motion of nearby galaxies is not easily explained.

The measurement of the amplitude and direction of the bulk flow has seen a range of results [73–84], using a variety of methods for determining distances. These methods include both: (i) direct estimate of luminosity distances via methods such as the Tully-Fisher, Faber-Jackson and Fundamental Plane relations, SNe Ia etc; and (ii) indirect estimates using the signatures of galaxy clusters on the CMB anisotropies via the kinematic Sunyaev–Zel'dovich (kSZ) effect, a secondary CMB anisotropy. All observations are subject to complex statistical biases, selection effects and systematic uncertainties. These questions, as well as the question of the whether the bulk flow amplitude is consistent with the expectations of the ΛCDM model. Estimates of the bulk flow amplitude via the kSZ effect as high as $600 - 1000\,\mathrm{km\,s^{-1}}$ on large scales [75] are particularly controversial and the subject of much debate [79, 81, 82].

Observations with more traditional distance estimators sometimes also find bulk flows inconsistent with the ΛCDM model [73, 74]. Watkins et al. [73] find an amplitude of $407 \pm 81\,\mathrm{km\,s^{-1}}$ towards $(287^\circ \pm 9^\circ, 8^\circ \pm 6^\circ)$. By comparison the best-fit WMAP5 ΛCDM model predicted a velocity field with a root mean square standard deviation $\sim 110\,\mathrm{km\,s^{-1}}$. By contrast, Davis & Nusser [77] and Ma & Scott [80] find a bulk flow in similar directions as [73, 74] but with amplitudes consistent with the ΛCDM expectation.

Identifying the most significant source of the bulk flow, has been at the centre of cosmic flow studies. Early studies looked for a distant, massive concentration that could "pull" galaxies towards it, such as the Great Attractor and Local Supercluster, at a distance of $\sim 30 - 55h^{-1}$Mpc [85]. More recently studies have focused on the more distant Shapley concentration, at a distance of $\sim 125 - 150h^{-1}$Mpc [85]. However, subsequent studies [86] found no signature of infall of galaxies on the far side, as would be expected in the Newtonian framework.

1.3.2 Minimum spherically averaged Hubble expansion variation

Recently Wiltshire and collaborators [87, 88] have analysed observations of the variation of the local expansion, by considering spherical and angular averages of luminosity distances versus redshifts, generalising techniques first introduced by Li and Schwarz [89] for spherical averages, and by McClure and Dyer [90] for angular averages.

In the case of the spherical averages a best fit linear Hubble law is determined in independent radial shells – even on small scales in which the average expansion is nonlinear – by standard linear regression, minimising the quantity $\chi^2_s = \sum_{i=1}^{N_s} \left[\sigma_i^{-1}((d_L)_i - cz_i/H_s)\right]^2$, where s runs over the independent radial shells and N_s is the number of data points in the sth shell. Different Hubble constants H_s are fit in each independent shell, being given

by

$$H_s = \left(\sum_{i=1}^{N_s} \frac{(cz_i)^2}{\sigma_i^2} \right) \left(\sum_{i=1}^{N_s} \frac{cz_i (d_L)_i}{\sigma_i^2} \right)^{-1} \tag{1.26}$$

where σ_i is the uncertainty in $(d_L)_i$. Wiltshire et al. [87] analysed the COMPOSITE sample[12] of 4534 galaxy and cluster redshifts and distances [73, 74] by this approach and found, with strong Bayesian evidence, that the Hubble expansion is significantly more uniform in the frame of the Local Group (LG) of galaxies than in the standard CMB rest frame. (The rest frame of the Local Sheet in which the LG is embedded shows results similar to the LG frame.)

It was found the Hubble parameter in each shell approaches the asymptotic value, $\bar{H}_0$, faster when measured in the LG frame, rather than the CMB frame. Such a result might appear counter-intuitive at first as far as the standard cosmology is concerned, as it is assumed that the CMB frame coincides with the cosmic rest frame and naïvely the cosmic rest frame is the one in which the Hubble expansion is most uniform in a statistical sense.

Wiltshire et al. [87] also observed that the difference $\Delta H_s = H_{\text{s,CMB}} - H_{\text{s,LG}}$ was roughly inversely proportional to the average value of the squared luminosity distance, $\left\langle (d_L)^2 \right\rangle_s$, in each shell. They deduced that this could be understood by considering redshifts, z_i, observed in a frame of reference in which the variation of the spherically averaged Hubble expansion is minimised. An arbitrary local boost of the central observer then leads to inferred redshifts, z_i', in the new frame given by

$$\begin{aligned} cz_i \to cz_i' &= c(\gamma - 1) + \gamma \left[cz_i + \boldsymbol{v} \cdot \hat{\boldsymbol{n}}_i (1 + z_i) \right] \\ &\simeq cz_i + \boldsymbol{v} \cdot \hat{\boldsymbol{n}}_i (1 + z_i) + \mathcal{O}\left(\beta^2\right) \qquad (1.27) \\ &\simeq cz_i \left[1 + \mathcal{O}(\beta) \right] + \boldsymbol{v} \cdot \hat{\boldsymbol{n}}_i \,. \qquad (1.28) \end{aligned}$$

where $\beta = v/c$ and γ is the Lorentz factor. In the Newtonian velocity addition approximation[13], (1.28) with terms $\mathcal{O}(\beta)$ neglected—which is widely used in the peculiar velocities community—this results in the changes $(cz_i)^2 \to (cz_i')^2 = (cz_i)^2 + 2cz_i\, \boldsymbol{v} \cdot \hat{\boldsymbol{n}}_i + (\boldsymbol{v} \cdot \hat{\boldsymbol{n}}_i)^2$ in the numerator of (1.26), and $cz_i (d_L)_i \to cz_i (d_L)_i + (d_L)_i\, \boldsymbol{v} \cdot \hat{\boldsymbol{n}}_i$ in the denominator. Given data uniformly distributed over the sky then the terms linear in (1.26) are roughly

[12] The COMPOSITE sample is a compilation of several major peculiar velocity surveys and was designed to select the best data available.

[13] The $\mathcal{O}(\beta)$ correction is at most 0.5% for the data sets considered, at least one order of magnitude smaller than typical distance uncertainties.

self-cancelling and one finds to leading order

$$\Delta H_s = H_s' - H_s \sim \left(\sum_{i=1}^{N_s} \frac{(\boldsymbol{v}\cdot\hat{\boldsymbol{n}}_i)^2}{\sigma_i^2}\right)\left(\sum_{i=1}^{N_s} \frac{cz_i(d_L)_i}{\sigma_i^2}\right)^{-1}$$
$$\approx \frac{v^2}{3\bar{H}_0\left\langle (d_L)_i^2\right\rangle_s} \tag{1.29}$$

McKay and Wiltshire [88] systematically investigated the characterisation of the frame of minimum spherically averaged Hubble expansion variation via (1.29), upon performing arbitrary boosts of the central observer. They investigated both the COMPOSITE sample and the *Cosmicflows-II* sample [91] of 8162 redshifts and distances, finding consistent results, although the latter sample has an unsubtracted distribution Malmquist bias which limited its usefulness. They confirmed that the CMB frame is significantly different from the frame in which the spherically averaged Hubble expansion converges most quickly to an asymptotic linear Hubble law. The difference of the CMB and LG frames coincides with the expectation (1.29) apart from a small range of distances $40 \lesssim d_L \lesssim 60h^{-1}$Mpc, in which the CMB frame gives a better fit. By contrast, the LG frame is a member of a degenerate set of local Lorentz frames that cannot be distinguished from each other as candidate *minimum Hubble expansion variation* frames, on the basis of existing data[14].

This result was unexpected in the standard framework, as no one had anticipated a relation such as (1.29) which could make sense of the "nonlinear regime" well below the statistical homogeneity scale. Indeed, in SNe Ia analyses data is often simply cut off below a redshift $z < 0.023$ [92]. However, very recently Kraljic & Sarkar [93] further investigated spherical averages using N-body simulations. They concluded that not only can one find candidate LG locations which give results numerically consistent with Eq. (1.29) when comparing the simulated difference between the simulated LG and CMB frames, but the departure from the relation (1.29) seen in the COMPOSITE and *Cosmicflows–II* in the distance range in which structures are most nonlinear can also be fit numerically if a bulk flow is included in the LG frame. The likelihood of such bulk flows is yet to be determined in the ΛCDM framework, and cannot be separated from the question of selection effects and statistical biases as different bulk flow magnitudes were found in comparing the fits of the COMPOSITE and *Cosmicflows–II* samples [93]. Consequently, the results of [88] do not directly contradict the ΛCDM paradigm. The statistical likelihood of the bulk flow amplitude and its match to observations are separate questions which are still to be resolved in the ΛCDM framework.

[14]There is no data in the plane of our Milky Way galaxy, as it obscures more distant galaxies. This does not pose a problem in terms of sky coverage for the statistical tests, as the missing region—the so-called 'Zone of Avoidance'—is symmetrical on the sky. However, it turns out that one can perform boosts of order $100 - 200\,\mathrm{km\,s^{-1}}$ in the plane of the Milky Way without changing the statistical likelihood of the fit to (1.29) [88].

1.3.3 Tests of differential cosmic expansion

In addition to the result concerning the uniformity of the spherically averaged Hubble expansion, Wiltshire et al. [87] also studied angular averages. They found that there is a range of distances $40 \lesssim d_L \lesssim 60h^{-1}$Mpc for which there is a deviation from the spherical average relation (1.29) of difference of the Hubble parameter in the CMB and LG frames, which also correlates with a significant difference in the fit of a dipole Hubble expansion law in independent spherical shells. Evidently nonlinear structures in this range (which encompasses the Great Attractor) are responsible for both effects.

The boost to the CMB frame improves the fit of the spherical averaged expansion in the distance range $40 \lesssim d_L \lesssim 60h^{-1}$Mpc relative to the LG frame, and also greatly reduces the dipole. As the distance is further increased, however, Wiltshire et al. [87] find that the dipole in the CMB frame increases while the that in the LG frame reduces becoming statistically consistent with zero[15]. This suggests a possibility that the large bulk flow seen in the CMB frame may be a systematic error resulting from a wrong choice of rest frame if the geometry below the statistical homogeneity scale is not the standard FLRW geometry. In particular, exact solutions of Einstein's equations for general dust inhomogeneities—such as the LTB [42–44] and Szekeres [94] models—generally exhibit deviations from uniform Hubble expansion that cannot be interpreted as local boosts relative to a spatially flat background. Rather generic inhomogeneities should be understood to give rise to *relativistic differential expansion* [1], corresponding to gradients in the local expansion of underdense regions and neighbouring overdense regions.

Recently, in order to characterise the effects of relativistic differential cosmic expansion, Bolejko, Nazer & Wiltshire [1] have begun investigating ray tracing of null geodesics in exact solutions of Einstein's equations which asymptote to a standard FLRW cosmology on large spatial scales $\gtrsim 100h^{-1}$Mpc, while containing inhomogeneities on smaller scales which are not small perturbations of the FLRW geometry. The models are constrained by using the COMPOSITE sample in the LG frame to constrain the dipole of the local Hubble expansion field—assuming the LG frame to be the frame which is the expansion is closest to uniform—while also demanding that the amplitude and direction of the CMB dipole in the LG frame are consistent.

In these models, light propagation no longer leads to the simple redshift relation (1.22). The term $z_{\rm FLRW}$ is replaced by a redshift term with an intrinsic anisotropy in addition to the anisotropies arising from the multipoles of the Doppler term in (1.22). The redshift anisotropy can therefore be considered to be *non-kinematic*. If a significant fraction of the CMB dipole is non-kinematic, this raises the possibility [87] that various large angle anomalies in the CMB anisotropy spectrum might be related to unexpected systematic errors arising from removal of the CMB dipole, which is performed at the

[15]For very large distances, $d_L \gtrsim 100h^{-1}$Mpc the data becomes too sparse to draw firm statistical conclusions.

same time as removal of microwaves emissions due to the Milky Way galaxy and point sources.

Since the first WMAP data was released potential anomalies have been detected in the primordial CMB anisotropy spectrum, with varying degrees of statistical significance. These include

(1) a power asymmetry between the northern and southern galactic hemispheres [95–98];

(2) very low power in the CMB quadrupole power [95, 99];

(3) the alignment of the quadrupole and octupole [99–101]; and

(4) a "parity asymmetry" between even and odd multipoles [104].

Although there is much debate about the use of *a posteriori* statistics, and the significance of the anomalies given realisations of the CMB anisotropy spectrum from primordial inflation within the ΛCDM model, the significance of some of these problems has increased with the release of Planck satellite data [105, 106]. Some of the anomalies may be related: a study of systematic effects by Freeman et al. [107] revealed that a 1-2% error in the CMB dipole subtraction could potentially cure the power asymmetry anomaly, which in turn may affect the parity anomaly and possibly the quadrupole/octupole alignment.

1.3.4 Characterising a non-kinematic CMB dipole

The programme instigated by Bolejko, Nazer & Wiltshire [1] of using exact solutions of Einstein's equations as small scale nonlinear foreground inhomogeneities requires a huge amount of development still, in order to characterise the differences that might be expected from the standard model in terms of the large angle multipoles. Possible implications such as the question of large angle anomalies cannot be investigated until such work is carried out. As a step towards this Bolejko et al. [1] suggested defining *non-kinematic relativistic differential expansion* to occur when the difference

$$\Delta T_{\rm nk-hel} = \frac{T_{\rm AIE}}{\gamma_{\rm AIE}(1-\boldsymbol{\beta}_{\rm AIE}\cdot\hat{\boldsymbol{n}}^{\rm hel})} - \frac{T_0}{\gamma_{\rm CMB}(1-\boldsymbol{\beta}_{\rm CMB}\cdot\hat{\boldsymbol{n}}^{\rm hel})}, \tag{1.30}$$

has a measurably nonzero dipole[16] when expanded in spherical harmonics, where $\boldsymbol{\beta}_{\rm AIE} = \boldsymbol{v}_{\rm AIE}/c$ is the boost of a particular "Average Isotopic Expansion (AIE) frame" to the heliocentric frame, $\gamma_{\rm AIE} = (1-\beta^2_{\rm AIE})^{-1/2}$,

$$T_{\rm AIE}(\hat{\boldsymbol{n}}^{\rm AIE}) = \frac{T_{\rm CMB}}{1+z_{\rm AIE}(\hat{\boldsymbol{n}}^{\rm AIE})}\,. \tag{1.31}$$

[16] In practice this means a contribution to (1.30) of at the least the same level, $10^{-5}T_0$, as the primordial spectrum; i.e., one order of magnitude larger than the conventional boost dipole.

is the anisotropic CMB temperature as measured in the AIE frame, and

$$T_{\rm CMB} = (1 + z_{\rm dec})T_0 \tag{1.32}$$

is the mean intrinsic temperature of the primordial plasma at decoupling, $z_{\rm dec}$ being the constant isotropic redshift of decoupling in the FLRW model. The AIE frame is defined as the local Lorentz frame at our location in which the spherically averaged luminosity distance–redshift relation in independent radial shells has *minimal* variations relative to a linear Hubble law [87, 88]. In this thesis will take the AIE frame to be the Local Group frame. The definition (1.30), (1.31) still leaves various ambiguities. It is the aim of this thesis to clarify such ambiguities in an effort to more concretely characterise non-kinematic anisotropies in CMB analysis.

There are several ways that a local Lorentz boost manifests on the blackbody spectrum beyond inducing a large dipole. A boost also induces quadrupole and octupole moments on the orders 10^{-6} K and 10^{-9} K respectively. In practice these contributions are too small to be measured as they are swamped by the 10^{-5} K primordial fluctuations that serves to noisy the signal.

The size of these effects become more apparent with larger boosts. However, as the dipole is $\sim 1\,$mK the boost required is only weakly relativistic with a magnitude of $\beta \sim 10^{-3}$ (or $\sim 300\,{\rm km\,s^{-1}}$) and so the effects on the CMB are subtle. Nevertheless they have been measured.

In 2013 the *Planck* collaboration measured the direction and magnitude of the boost using the aberration and modulation effects [108]. The aberration and modulation effects manifest in the statistics of the CMB. In particular, they induce couplings between multipole moments [109, 110] and it is precisely these couplings that have been measured by *Planck*. However, their claim that the kinematic nature of the transformation from the heliocentric to CMB frames has been verified by these effects actually depends on angular scale. The boost direction coincides with the expected direction $(\ell, b) = (264^\circ, 48^\circ)$ only for small angle multipoles $l_{\rm min} = 500 < l < l_{\rm max} = 2000$. For large angle multipoles $l < l_{\rm max} = 100$ the inferred boost direction moves across the sky to coincide with the modulation dipole anomaly direction [98], $(\ell, b) = (224^\circ, -22^\circ) \pm 24^\circ$, associated with the CMB anomalies. Since the non-kinematic terms in (1.30) only affect large angle power, the angular scale dependence of the results of [108] and their association with the anomaly direction provides some tentative evidence for the hypothesis of Wiltshire and collaborators [1, 87].

It has been known for some time now that off-centre observers in the spherically symmetric LTB void models can also observe a large dipole [45, 46, 111, 112]. The idea that such a dipole may contribute to a significant fraction of the CMB dipole has not been seriously considered, however, until the work of Bolejko et al. [1]. One reason for this is

that attention has often been focused on the non-Copernican models with unrealistically large voids discussed in §1.2.2.

Another reason is that simple analytic estimates of higher order multipoles have been made based on the case of both source and observer being *outside* the void – this making it possible to do estimates without the complex ray tracing methods studied by Bolejko et al. [1]. Based on such estimates, generally a "Rees–Sciama quadrupole" of the same magnitude as the "Rees–Sciama dipole" was anticipated, and so an "alternative origin of the CMB dipole" was dismissed [113]. The results of Bolejko et al. show, however, that such naïve estimates do not apply to the case observers deep inside nonlinear structures. One must account for the actual local environment, which in our case includes structures such as the Local Void and Great Attractor – semi-realistic profiles for which have emerged from the ray tracing constraints in the Bolejko et al. analysis [1].

To make further progress it is therefore necessary that we also consider the higher order effects induced on light propagation by nonlinear structures, such as the aberration and modulation signatures. Even in the well-studied case of spherical voids little attention has been paid to the question of whether one might find signatures nominally identified as the aberration and modulation effects. (See, however, [114, 115].) As one aim of this thesis, in Chapter 4 we will systematically investigate this question, including the manner in which Lorentz boost like signatures can be found in the limiting linear regime.

1.4 Summary of research

In this thesis we investigate the possibility of the existence of a non-kinematic dipole component by modelling nonlinear voids using exact solutions of the Einstein field equations. We

- use the LTB and Szekeres solutions to explore the dependence of observer's position (i.e. the 'peculiar potential') on the CMB dipole and quadrupole;
- compare the predictions of linear theory with the exact models;
- derive formulae to estimate the monopole and dipole of the CMB measured in the heliocentric frame based on the LTB model;
- investigate the extent to which such structures can induce a CMB dipole degenerate with the standard kinematic interpretation. In particular, we look for physical mechanisms that might induce couplings of the type seen by *Planck*, but caused by the influence of inhomogeneous structures on the CMB.

Chapter 2 will begin with a review of perturbation theory in the standard FLRW cosmology, and how it sources anisotropies. Chapter 3 will review the exact inhomogeneous

dust solutions of Einstein's equations that are important for our investigations, namely LTB and Szekeres model. Chapter 4 presents new original results. Chapter 5 concludes with brief discussion of the impact of our results for future research.

Notation and units: Unless otherwise stated, we use geometrised units in which $G = 1 = c$, where G is the gravitational constant and c the speed of light. We use the Einstein summation convention with Greek indices $\mu, \nu, \lambda, \ldots$ running over spacetime coordinates labelled $0, 1, 2, 3$, and Latin indices $i, j, k, \ldots$ running over spatial coordinates labelled $1, 2, 3$. We use the metric sign convention, $(-, +, +, +)$. Spatial 3-vectors are denoted in boldface. Euclidean space unit 3-vectors ("directed line segments") will be denoted with hats, e.g., $\hat{\boldsymbol{n}}$. We use comma notation to denote partial derivatives and semicolons to denote covariant derivatives, e.g., $\Phi_{,r} \equiv \partial\Phi/\partial r$ and $T^{\mu\nu}{}_{;\nu} \equiv \nabla_\nu T^{\mu\nu}$.

Chapter 2

Cosmological Perturbation Theory and the Effects of Cosmic Structure

In this thesis we are primarily interested in evaluating the effects of light propagation in exact solutions of the Einstein field equations, which are fully nonlinear and beyond the realm of perturbation theory. By contrast, the standard ΛCDM cosmology is based on perturbation theory about a global FLRW background in the early universe, while the growth of structure in the late epoch universe is subsequently modelled by Newtonian gravity [26] when perturbation theory breaks down.

In order to compare and contrast our nonlinear approach (see chapter 3), we first review the treatment of perturbations in the standard FLRW cosmology, particularly in relation to the generation of the secondary CMB anisotropies, which are the focus of our investigation.

2.1 Cosmological perturbation theory

In the standard framework, initially on all scales and at present large ($\gg 100h^{-1}$ Mpc) scales, large-scale structure is represented by first-order perturbations on the FLRW background geometry. The first-order perturbed metric has the form

$$g_{\mu\nu} = \overline{g}_{\mu\nu} + \delta g_{\mu\nu}, \tag{2.1}$$

where $\overline{g}_{\mu\nu} = g^{\mathrm{FLRW}}_{\mu\nu}$ is the unperturbed background metric and $\delta g_{\mu\nu}$ the first-order perturbation. The perturbed equations are found by inserting these quantities into the field equations keeping only terms up to first-order.

In general, the perturbed line element in comoving coordinates takes the form

$$\mathrm{d}s^2 = g_{\mu\nu}\,\mathrm{d}x^\mu\,\mathrm{d}x^\nu = -(1+2A)\,\mathrm{d}t^2 + 2B_i\,\mathrm{d}x^i\,\mathrm{d}t + a^2(t)(\overline{g}_{ij} + h_{ij})\,\mathrm{d}x^i\,\mathrm{d}x^j, \tag{2.2}$$

where A, B_i and h_{ij} are all functions of t and x^i and between them possess ten degrees of freedom. Four of these are coordinate degrees of freedom and can be fixed by a choice of gauge. For instance, in the synchronous gauge $A = 0$ and $B_i = 0$ so that the metric

is in diagonal form with $g_{tt} = -1$ and $g_{ti} = 0 = g_{it}$ and coordinate time coincides with proper time. The perturbation h_{ij} can be decomposed into scalar, vector and tensor parts and it turns out that for a FLRW background these decouple, i.e., each sector evolves independently of the others.[1] In this chapter we will focus on scalar perturbations, ignoring vector and tensor perturbations as their contribution to the CMB anisotropy is negligible.

In the epoch of early structure formation when the ISW effect first becomes apparent, it is most intuitive to study evolution of perturbations in the Newtonian gauge. We consider the case in which the background metric $\overline{g}_{\mu\nu} = g^{\mathrm{FLRW}}_{\mu\nu}$ is given by the spatially flat FLRW metric:

$$\mathrm{d}\bar{s}^2 = g^{\mathrm{FLRW}}_{\mu\nu}\,\mathrm{d}x^\mu\,\mathrm{d}x^\nu = -\,\mathrm{d}t^2 + a^2\,\delta_{ij}\,\mathrm{d}x^i\,\mathrm{d}x^j, \tag{2.3}$$

where $a = a(t)$ is the scale factor of the spatially flat FLRW background. The perturbed metric (2.1) in Newtonian gauge then reads

$$\mathrm{d}s^2 = g_{\mu\nu}\,\mathrm{d}x^\mu\,\mathrm{d}x^\nu = -(1+2\Phi)\,\mathrm{d}t^2 + a^2(1-2\Psi)\,\delta_{ij}\,\mathrm{d}x^i\,\mathrm{d}x^j, \tag{2.4}$$

where $\Phi = \Phi(t, \boldsymbol{x})$, $\Psi = \Psi(t, \boldsymbol{x})$ are known as the Newtonian and curvature potentials respectively.

2.1.1 Evolution of structure

Before we can evaluate (2.59) we first need to determine the explicit time dependence of Φ and Ψ by solving the field equations for the metric (2.4) and a linearly perturbed perfect fluid energy-momentum tensor. Since the spatially flat background rigidly evolves, one can solve the Einstein equations order by order. The zeroth order (or unperturbed) equations are just the Friedmann equations

$$H^2 = \left(\frac{\dot{a}}{a}\right)^2 = \frac{8\pi\rho}{3} + \frac{1}{3}\Lambda \qquad \text{and} \qquad \frac{\ddot{a}}{a} = -\frac{4\pi}{3}\,(\rho + 3p) + \frac{1}{3}\Lambda. \tag{2.5}$$

For the following discussion we consider only a subset of the Einstein equations of the metric (2.4) and a perturbed perfect fluid energy-momentum tensor.[2] These are

$$\nabla^2\Psi - 3\mathcal{H}(\Psi' + \mathcal{H}\Psi) = 4\pi a^2\delta\rho, \tag{2.6a}$$

$$\Psi'' + 3\mathcal{H}\Psi' + (2\mathcal{H}' + \mathcal{H}^2)\Psi = 4\pi a^2\delta p, \tag{2.6b}$$

$$\nabla^2\Psi = 4\pi a^2\delta\rho, \tag{2.6c}$$

where the equality sign should be understood to mean equality up to first order only. The equations are written in terms of conformal time with $\mathcal{H} = a'/a$ the conformal Hubble

[1] The decoupling of sectors is a special property not shared by other perturbed models, such as perturbed LTB models [116, 117].

[2] The complete set of perturbed Einstein equations may be found in, e.g., §2.3 of [118].

parameter, $\delta\rho = \delta\rho(\eta, \boldsymbol{x})$ and $\delta p = \delta p(\eta, \boldsymbol{x})$ the first order perturbations in density and pressure respectively. Note the gradient operator is taken w.r.t. the comoving coordinates $\boldsymbol{x}$. Further we assume the anisotropic stress in the perturbed energy-momentum tensor vanishes so that we have $\Phi = \Psi$.[3] Using (2.6a) and (2.6b) along with the Friedmann equations (2.5), and assuming that perturbations are adiabatic so that $\delta p = w\,\delta\rho$ (with w the equation of state parameter of $p = w\rho$), we can derive the evolution equation

$$\Psi'' + 3\mathcal{H}(1+w)\Psi' - w\nabla^2\Psi = 0. \tag{2.7}$$

At this point it is standard in cosmological perturbation theory to write this equation in Fourier space where each Fourier mode can be solved through the second-order ODE

$$\Psi_k'' + 3\mathcal{H}(1+w)\Psi_k' + wk^2\Psi_k = 0. \tag{2.8}$$

The kth mode, $\Psi_k \equiv \Psi(\eta, \boldsymbol{k})$, is the Fourier transform of $\Psi = \Psi(\eta, \boldsymbol{x})$:

$$\Psi(\eta, \boldsymbol{k}) = \int \mathrm{d}^3\boldsymbol{x}\, \Psi(\eta, \boldsymbol{x})\, \mathrm{e}^{i\boldsymbol{k}\cdot\boldsymbol{x}}. \tag{2.9}$$

We consider three cases of a universe dominated by (i) matter, (ii) radiation, and (iii) dark energy.

Matter domination Consider an Einstein-de Sitter background Friedmann model, i.e., one that is spatially flat and dust dominated $\rho = \rho_m \propto a^{-3}$. Since dust has zero pressure $w = 0$ and $a \propto \eta^{2/(1+3w)} = \eta^2$ (which implies $\mathcal{H} = 6/\eta$), (2.8) becomes

$$\Psi_k'' + \frac{6}{\eta}\Psi_k' = 0. \tag{2.10}$$

The general solution is $\Psi_k = A_k + B_k\eta^{-5}$, where A_k and B_k are constants. Because perturbations are small in the early universe (i.e. when η is small), we have $B_k = 0$ so that

$$\Psi_k = \text{const}, \tag{2.11}$$

or, in real space, the potential Ψ is time-independent.

At last scattering $\Omega_m \simeq 0.76$ and $\Omega_r \simeq 0.24$, but Ω_r drops below 1% by a redshift $z = 33$, so that the universe then becomes matter dominated.

Radiation domination In the case of a spatially flat universe which is radiation dominated, the ISW effect comes into play. Now $w = 1/3$ and $a \propto \eta$ which implies $\mathcal{H} = 1/\eta$ so the evolution equation is

$$\Psi_k'' + \frac{4}{\eta}\Psi_k' + \frac{k^2}{3}\Psi_k = 0. \tag{2.12}$$

[3]Strictly this is only true if we assume the potentials decay at infinity.

The solutions are more complicated being given in terms of spherical Bessel functions of the first and second kind. Qualitatively, modes with wavelength $\lambda(\propto k^{-1})$ larger than the Hubble horizon $\mathcal{H}^{-1}$ (i.e. *superhorizon* modes) decay much slower than modes smaller than the horizon that decay as $a^{-2} \propto \eta^{-2}$. Realistically, a more complicated solution before dark energy dominates applies, namely

$$a = a_{\rm eq}\left[\left(\frac{\eta}{\eta_*}\right)^2 + 2\left(\frac{\eta}{\eta_*}\right)\right], \tag{2.13}$$

where $\eta_* = 2\,\Omega_r^{1/2}/(H_0\,\Omega_m)$ and $a_{\rm eq} = \Omega_r/\Omega_m$ [23]. Then $a \propto \eta^2$ when radiation dominates, and $a \propto \eta$ when matter dominates. Modes that were subhorizon during the epoch of radiation domination will then be significantly damped at the time of matter-radiation equality compared with modes that were superhorizon.

Dark energy domination Once the radiation density becomes negligible, the spatially flat FLRW model with matter and a cosmological constant is given by the background solution

$$a = \left(\frac{\Omega_m}{\Omega_\Lambda}\right)^{1/3} \sinh^{2/3}\left(\frac{3}{2}\sqrt{\Omega_\Lambda}H_0 t\right), \tag{2.14}$$

where $\Omega_\Lambda = \Lambda/(3H_0^2)$. Consider the limiting case (in the future) in which the cosmological constant dominates the energy density, $\rho \simeq \rho_\Lambda = $ const. The cosmological constant has an equation of state $p_\Lambda = -\rho_\Lambda = $ const and we assume its density and pressure remains unperturbed $\delta\rho_\Lambda = \delta p_\Lambda = 0$. Thus the r.h.s. of (2.6b) vanishes and we have the following closed equation in real space

$$\Psi'' + 3\mathcal{H}\Psi' + (2\mathcal{H}' + \mathcal{H}^2)\Psi = 0, \tag{2.15}$$

where $\mathcal{H} \equiv a'/a$ is the comoving Hubble parameter. Using the Friedmann equations (2.5) it is straightforward to show that $2\mathcal{H}' + \mathcal{H}^2 = a^2\Lambda$. When expressed in cosmic time (2.15) is

$$\ddot{\Psi} + 4H\dot{\Psi} + \Lambda\Psi = 0. \tag{2.16}$$

We remark this equation as well as (2.10), which may be expressed as $\ddot{\Psi} + 4H\dot{\Psi} = 0$, does not have any scale dependence (i.e.,k does not appear) so that all modes evolve uniformly.[4]

When dark energy dominates we have $H^2 \simeq \Lambda/3$ and the equation becomes

$$\ddot{\Psi} + 4\sqrt{\frac{\Lambda}{3}}\dot{\Psi} + \Lambda\Psi = 0, \tag{2.17}$$

[4]This is important in the early initial period of inflationary expansion, which closely resembles a de Sitter universe. This means that the primordial initial conditions which seeded structure were scale-invariant. In Fourier space, one speaks of the fluctuations having a scale-invariant matter power spectrum. In fact in the standard model a close to scale-invariant matter power spectrum is observed, with departures from the exact scale-invariance depending on both the potentials of the inflationary model and the manner in which the period of inflation ends.

which has the general solution

$$\Psi(t,\boldsymbol{x}) = c_1(\boldsymbol{x})\mathrm{e}^{-3Ht} + c_2(\boldsymbol{x})\mathrm{e}^{-Ht}, \tag{2.18}$$

where $H = \sqrt{\Lambda/3} = \text{const}$ and as we can see both solutions are decaying.

The continuity and Euler equations

With the metric (2.4) the conservation equation $\nabla_\mu T^{\mu\nu} = 0$ splits into a continuity equation

$$\frac{\partial\delta}{\partial t} + \frac{1}{a}\nabla\cdot\big[(1+\delta)\,\boldsymbol{v}\big] = 0, \tag{2.19}$$

and the Euler equation of motion

$$\frac{\partial\boldsymbol{v}}{\partial t} + H\boldsymbol{v} + \frac{1}{a}(\boldsymbol{v}\cdot\nabla)\,\boldsymbol{v} = -\frac{1}{a}\nabla\Psi. \tag{2.20}$$

These equations to first order are

$$\frac{\partial\delta}{\partial t} + \frac{1}{a}\nabla\cdot\boldsymbol{v} = 0, \tag{2.21}$$

and

$$\frac{\partial\boldsymbol{v}}{\partial t} + H\boldsymbol{v} = -\frac{1}{a}\nabla\Psi. \tag{2.22}$$

2.1.2 The assumption of uniform growth of scales

Within the above framework of cosmological perturbation theory often an additional assumption is made, which is that all scales grow uniformly:

$$\delta(t,\boldsymbol{r}) = D(t)\,\delta(t_0,\boldsymbol{r}) \iff \delta(t,\boldsymbol{k}) = D(t)\,\delta(t_0,\boldsymbol{k}), \qquad D(t_0) = 1, \tag{2.23}$$

where $\delta(t,\boldsymbol{r}) = \delta\rho(t,\boldsymbol{r})/\overline{\rho}(t)$ is the density contrast, $D(t)$ is determined from the field equations, and $\delta(t_0,\boldsymbol{r})$ can be freely chosen (provided it does not violate $|\delta(t_0,\boldsymbol{r})| \ll 1$).

Under such an assumption the time dependence is separated out from $\delta(t,\boldsymbol{r})$ thereby allowing one to solve Poisson's equation (2.6c) analytically. Using Friedmann's equation we can rewrite Poisson's equation in a more useful form as

$$\nabla^2\Phi = \frac{3}{2}\Omega_m\,H_0^2\,a^{-1}(t)\,\delta(t,\boldsymbol{r}). \tag{2.24}$$

In linear theory this becomes

$$\nabla^2\Phi = \frac{3}{2}\Omega_m H_0^2\,g(t)\,\delta(t_0,\boldsymbol{r}), \tag{2.25}$$

where $g(t) \equiv D/a$ is known as the *linear growth factor*. For brevity, we define the shorthand $\delta(\boldsymbol{r}) \equiv \delta(t_0,\boldsymbol{r})$ to mean the density contrast at the present time so that δ on its own is understood to mean $\delta(\boldsymbol{r})$.

For the rest of this section we assume an isolated and spherically symmetric matter distribution, so that in a coordinate system centred at the origin we have $\delta(\boldsymbol{r}) = \delta(r)$ and $\Phi(t, \boldsymbol{r}) = \Phi(t, r)$.

Solving Poisson's equation using the method of Green's functions with the boundary condition $\Phi \to 0$ as $r \to \infty$ we obtain

$$\Phi(t, r) = -\frac{3}{2}\Omega_m H_0^2 \, g(t) \, F(r), \tag{2.26}$$

with

$$F(r) \equiv \int_0^r \frac{r'^2}{r}\delta(r') \, \mathrm{d}r' + \int_r^\infty r'\delta(r') \, \mathrm{d}r', \tag{2.27}$$

satisfying $\nabla^2 F = -\delta$. The linear growth factor $g(t)$, or equivalently $D(t)$, is determined by substituting $\delta(t, r) = D(t) \, \delta(t_0, r)$ into (3.25) to obtain the following ODE:

$$\ddot{D} + 2\frac{\dot{a}}{a}\dot{D} - 4\pi G\bar{\rho}D = 0. \tag{2.28}$$

Note that $D(t) < 1$ for $t < t_0$ and the general solution to this equation has a growing and decaying solution. For the case of a spatially flat background, $\Omega_k = 0$, one can verify the growing solution [119] is

$$D(t) \propto H(t) \int_0^t \frac{\mathrm{d}t'}{a^2(t')H^2(t')}, \tag{2.29}$$

with the constant of proportionality set by the initial conditions. A more convenient description of D was found [120] by working in conformal time and introducing a function $P = P(\eta)$ related to D by

$$g \equiv \frac{D}{a} = A\left(1 - \frac{a'}{a}P'\right), \tag{2.30}$$

where $A = 1/(1 - \frac{a'}{a}P')|_{a=1}$ since $D(t_0)/a(t_0) = 1$. Substituting this into (2.28) and using the Friedmann equations (2.5), we have after a straightforward, if tedious, calculation the simpler equation

$$P'' + 2\frac{a'}{a}P' - 1 = 0. \tag{2.31}$$

Thus, we have swapped an equation of D for an equation of P, which is readily solved to obtain

$$P(\eta) = \int_0^\eta \mathrm{d}\eta' \left\{ a^{-2}(\eta') \left[\int_0^{\eta'} \mathrm{d}\eta'' a^2(\eta'') \right] \right\}. \tag{2.32}$$

With our expression (2.26) for Φ in hand, we are ready to solve (2.22) for the first-order velocity $\boldsymbol{v}$:

$$\frac{\partial \boldsymbol{v}}{\partial t} + H\boldsymbol{v} = \frac{3}{2}\Omega_m \, H_0^2 \, a^{-1}(t) \, g(t) \nabla F(r). \tag{2.33}$$

Observing that the right-hand side is the product of functions of t and r, we assume the solution to be of the form $\boldsymbol{v} \propto G(t)\nabla F(r)$, with the proportionality constant judiciously

chosen to simplify the resulting equation of G. Substituting this ansatz into (2.33) we find the constraint on G:

$$G' + \frac{a'}{a}\left(G + P'\right) - 1 = 0. \tag{2.34}$$

Comparing with (2.31) we see that this is satisfied if $G = P'$. Thus

$$\boldsymbol{v}(t,r) = \frac{3}{2}A\Omega_m H_0^2 P'(\eta)\nabla F = -\frac{3}{2}A\Omega_m H_0^2 P'(\eta)\left(r^{-2}\int_0^r \delta(r')r'^2\,\mathrm{d}r'\right)\hat{\boldsymbol{r}}. \tag{2.35}$$

By differentiating (2.30) by η and using (2.31) as well as the Friedmann equations it can be shown that $D' = \frac{3}{2}A\Omega_m H_0^2 P'$. Using this relation and $\partial/\partial\eta = a\,\partial/\partial t$ we have the radial component v in a more standard form as

$$v(t,r) = -a(t)\,\dot{D}(t)\,r^{-2}\int_0^r \delta(r')r'^2\,\mathrm{d}r' = -a(t)H(t)f(t)\,r^{-2}\int_0^r \delta(r')r'^2\,\mathrm{d}r', \tag{2.36}$$

where

$$f(t) \equiv \frac{1}{H}\frac{\dot{D}}{D} = \frac{\mathrm{d}\ln D}{\mathrm{d}\ln a} \tag{2.37}$$

is called the *linear growth rate*. A widely used approximation by Peebles [70] when $\Omega_k = 0$ and $\Omega_\Lambda = 0$ is the simple relation $f \approx \Omega_m^{0.6}$, where now $\Omega_m = \Omega_{m0}/a^3$ is the matter density parameter not necessarily at the present time. If $\Omega_\Lambda \neq 0$ then $f \approx \Omega_m^{0.55}$ [121]. Besides a, H and f, which all depend on the background FLRW model only (i.e., they are independent of the details of the density perturbations), the velocity of an observer located at radius r is determined entirely by the density within a ball of radius r.

Note for a general matter distribution $\delta(\boldsymbol{r})$ we have upon rearranging (2.21) the equation

$$\nabla\cdot\boldsymbol{v} = -a\,\dot{\delta}(t,\boldsymbol{r}) = -aHf\delta(\boldsymbol{r}), \tag{2.38}$$

which may be solved using Green's functions to give

$$\boldsymbol{v}(t,\boldsymbol{r}) = \frac{1}{4\pi}aHf\int \delta(\boldsymbol{r}')\frac{\boldsymbol{r}-\boldsymbol{r}'}{|\boldsymbol{r}-\boldsymbol{r}'|^3}\mathrm{d}^3\boldsymbol{r}'. \tag{2.39}$$

We remark that this is the key equation used in the peculiar velocity formalism to investigate bulk flows (see §1.3.1).

2.2 CMB anisotropy from perturbation theory

The CMB temperature anisotropy was first put on a theoretical footing by Sachs and Wolfe in their pioneering 1967 work [122], which saw the first detailed study of the effects of a perturbed FLRW cosmology on the CMB. Indeed the study of light propagation in the universe underpins the theory of the CMB.

In this section we derive the CMB temperature anisotropy, $\Delta T/T$, in the framework of linear perturbation theory. These standard results can be found in, e.g., [118]. The statistical analysis of the CMB is deferred to §2.3.

In general relativity,[5] light is assumed to follow null geodesics given by

$$k^\nu \nabla_\nu k^\mu = 0, \qquad k^\mu \equiv \frac{\mathrm{d}x^\mu}{\mathrm{d}\lambda}\,, \tag{2.40}$$

i.e., the null geodesic equations. With an affine parameter λ the equations become

$$\frac{\mathrm{d}k^\mu}{\mathrm{d}\lambda} + \Gamma^\mu{}_{\alpha\beta} k^\alpha k^\beta = 0, \tag{2.41}$$

where $\Gamma^\mu{}_{\alpha\beta}$ is the Christoffel symbol.

Using the fact that null geodesics of conformally related geometries are identical[6] we can instead consider null geodesics of the conformally related metric given by

$$\gamma_{\mu\nu} \equiv a^{-2} g_{\mu\nu} = \eta_{\mu\nu} + h_{\mu\nu} \tag{2.42}$$

where $\eta_{\mu\nu} = \mathrm{diag}(-1,1,1,1)$ is the Minkowski metric, $h_{\mu\nu}$ the first-order perturbation, and $g_{\mu\nu}$ the metric (2.4). The conformally related line element is

$$a^{-2}\,\mathrm{d}s^2 = \gamma_{\mu\nu}\,\mathrm{d}x^\mu\,\mathrm{d}x^\nu = -(1+2\Phi)\,\mathrm{d}\eta^2 + (1-2\Psi)\,\delta_{ij}\,\mathrm{d}x^i\,\mathrm{d}x^j, \tag{2.43}$$

where η is conformal time and related to cosmic time by $\mathrm{d}\eta = \mathrm{d}t/a$.

We denote by $\Gamma^\mu{}_{\alpha\beta}$ and $\delta\Gamma^\mu{}_{\alpha\beta}$ the Christoffel symbols of $\gamma_{\mu\nu}$ and $h_{\mu\nu}$ respectively, and since the connection vanishes in Minkowski space $\Gamma^\mu{}_{\alpha\beta} = \delta\Gamma^\mu{}_{\alpha\beta}$. Further we denote by k^μ the null tangent vector of the conformally related metric (2.43). Note the only Christoffel symbols required in the following linear calculation is

$$\begin{aligned}\Gamma^0{}_{\alpha\beta} &= \frac{1}{2}\eta^{0\rho}\left(\partial_\beta h_{\alpha\rho} + \partial_\alpha h_{\rho\beta} - \partial_\rho h_{\alpha\beta}\right)\\ &= -\frac{1}{2}\left(\partial_\beta h_{\alpha 0} + \partial_\alpha h_{0\beta} - \partial_0 h_{\alpha\beta}\right)\end{aligned} \tag{2.44}$$

Henceforth barred quantities will denote unperturbed quantities of the conformally related background $\eta_{\mu\nu}$. Thus $\bar{k}^\mu$ is the null tangent vector such that $\eta_{\mu\nu}\bar{k}^\mu\bar{k}^\nu = 0$.

We assume the null geodesics of (2.43) are parametrised by an affine parameter λ and that

$$k^\mu \equiv \frac{\mathrm{d}x^\mu}{\mathrm{d}\lambda} = \bar{k}^\mu + \delta k^\mu. \tag{2.45}$$

where δk^μ is the perturbation. The null geodesic equations (2.41) to first order are

$$\begin{aligned}0 &= \frac{\mathrm{d}}{\mathrm{d}\lambda}\,k^\mu + \Gamma^\mu{}_{\alpha\beta}k^\alpha k^\beta\\ &\simeq \frac{\mathrm{d}}{\mathrm{d}\lambda}\,\delta k^\mu + \delta\Gamma^\mu{}_{\alpha\beta}\bar{k}^\alpha\bar{k}^\beta\end{aligned} \tag{2.46}$$

[5] Just as in special relativity, light propagates according to the wave equation $\nabla^\mu\nabla_\mu\varphi = 0$, the difference now being that spacetime is curved and solutions have the form $\varphi(x) = A(x)e^{i\psi(x)} + \cdots$. Light propagation is based on the *eikonal* or *geometric optics approximation*, which assumes that the phase ψ is changing much faster than the amplitude A so that the tangent vector, $k_\mu \equiv \partial_\mu\psi$, of light rays are null, i.e, $k^\mu k_\mu = 0$. The fact that k_μ is the gradient of a scalar means that light rays are irrotational, $\nabla_{[\mu}k_{\nu]} = 0$ and from these two items it follows that $0 = \nabla_\mu(k^\nu k_\nu) = 2k^\nu\nabla_\mu k_\nu = 2k^\nu\nabla_\nu k_\mu$, i.e., $k^\nu\nabla_\nu k^\mu = 0$.

[6] If $g_{\mu\nu}$ and $\gamma_{\mu\nu}$ are conformally related and have common coordinates x^μ then a null geodesic $\gamma^\mu = \gamma^\mu(\lambda)$ of $g_{\mu\nu}$ is also a null geodesic of $\gamma_{\mu\nu}$. However, the affine parameters will be different.

since $\frac{\mathrm{d}}{\mathrm{d}\lambda}\bar{k}^\mu = 0$. Here and in the following we denote by $\simeq$ equality to first order only. The equation for the conformal time component '0' is explicitly

$$\begin{aligned}\frac{\mathrm{d}}{\mathrm{d}\lambda}\,\delta k^0 &= -\delta\Gamma^0{}_{\alpha\beta}\bar{k}^\alpha\bar{k}^\beta \\ &= \bar{k}^\alpha\bar{k}^\beta\partial_\beta h_{\alpha 0} - \frac{1}{2}\bar{k}^\alpha\bar{k}^\beta\partial_0 h_{\alpha\beta} \\ &= \bar{k}^\beta\partial_\beta(h_{\alpha 0}\bar{k}^\alpha) - \frac{1}{2}\bar{k}^\alpha\bar{k}^\beta\partial_0 h_{\alpha\beta}\end{aligned} \tag{2.47}$$

Integrating between decoupling, λ_*, and the time of reception, λ_0, we find

$$\left[\delta k^0\right]_{\lambda_*}^{\lambda_0} = \left[h_{00} + h_{0j}\bar{k}^j\right]_{\lambda_*}^{\lambda_0} - \frac{1}{2}\int_{\lambda_*}^{\lambda_0}\frac{\partial}{\partial\eta}\,h_{\alpha\beta}\bar{k}^\alpha\bar{k}^\beta\;\mathrm{d}\lambda. \tag{2.48}$$

where we have used

$$(\bar{k}^0)^2 = \delta_{ij}\bar{k}^i\bar{k}^j = 1, \tag{2.49}$$

on the first term. By (2.49) and noting

$$h_{\mu\nu}\,\mathrm{d}x^\mu\,\mathrm{d}x^\nu = -2\Phi\,\mathrm{d}\eta^2 - 2\Psi\,\delta_{ij}\,\mathrm{d}x^i\,\mathrm{d}x^j, \tag{2.50}$$

equation (2.48) becomes

$$\begin{aligned}\left[\delta k^0\right]_{\lambda_*}^{\lambda_0} &= \left[-2\Phi + 0\right]_{\lambda_*}^{\lambda_0} - \frac{1}{2}\int_{\lambda_*}^{\lambda_0}\left[\bar{k}^0\bar{k}^0\,\frac{\partial}{\partial\eta}\,(-2\Phi) + \delta_{ij}\bar{k}^i\bar{k}^j\,\frac{\partial}{\partial\eta}\,(-2\Psi)\right]\,\mathrm{d}\lambda \\ &\simeq -2\Phi\big|_{\lambda_*}^{\lambda_0} + \int_{\lambda_*}^{\lambda_0}\frac{\partial}{\partial\eta}\,(\Phi+\Psi)\;\mathrm{d}\lambda\end{aligned} \tag{2.51}$$

An observer in the conformally related geometry $\gamma_{\mu\nu}$ has a 4-velocity of the form

$$u^\mu = \bar{u}^\mu + \delta u^\mu = (1 + \delta u^0, \delta u^i). \tag{2.52}$$

Imposing the timelike condition $u^\mu u_\mu = -1$ we obtain the relation

$$\begin{aligned}-1 &= \gamma_{00}(u^0)^2 + \gamma_{ij}u^i u^j \\ &= -(1+2\Phi)(1+\delta u^0)^2 + (1+2\Psi)\,\delta_{ij}\delta u^i\delta u^j \\ &\simeq -1 - 2(\delta u^0 + \Phi)\end{aligned} \tag{2.53}$$

i.e., $\delta u^0 = -\Phi$. Defining $v^i \equiv \delta u^i$, the 4-velocity has the form $u^\mu = (1-\Phi, v^i)$. We decompose the unperturbed null vector as $\bar{k}^\mu = \bar{u}^\mu + e^\mu$ where e^μ is a unit spacelike vector in the Minkowski background, i.e., $\eta_{\mu\nu}e^\mu e^\nu = 1$. Then

$$k^\mu = \bar{k}^\mu + \delta k^\mu = (1 + \delta k^0, e^i + \delta k^i). \tag{2.54}$$

Given the affine parameter λ of the metric $\gamma_{\mu\nu}$, a short calculation shows that $\lambda' = a^2\lambda$ is an affine parameter of the original metric $g_{\mu\nu}$. Letting $\tilde{k}^\mu$ be the null tangent vector

of $g_{\mu\nu}$, we have the relation $\tilde{k}^\mu = a^{-2}k^\mu$. The energy measured by an observer with 4-velocity $\tilde{u}^\mu$ is then

$$E = -g_{\mu\nu}\tilde{u}^\mu\tilde{k}^\nu = -a^{-1}\gamma_{\mu\nu}u^\mu k^\nu \tag{2.55}$$

since $\tilde{u}^\mu = \frac{\mathrm{d}x^\mu}{\mathrm{d}t} = \frac{\mathrm{d}\eta}{\mathrm{d}t}\frac{\mathrm{d}x^\mu}{\mathrm{d}\eta} = a^{-1}u^\mu$. Evaluating

$$\begin{aligned}\gamma_{\mu\nu}u^\mu k^\nu &= \gamma_{00}u^0k^0 + \gamma_{ij}u^ik^j \\ &= -(1+2\Phi)(1-\Phi)(1+\delta k^0) + (1-2\Psi)\delta_{ij}v^i(e^j+\delta k^j) \\ &\simeq -1-\Phi-\delta k^0 + \delta_{ij}v^ie^j\end{aligned}$$

and using (2.51) and (2.55), the ratio of the observed and emitted photon energy, E_0 and E_* respectively, is

$$\begin{aligned}\frac{E_0}{E_*} &= \frac{(g_{\mu\nu}\tilde{u}^\mu\tilde{k}^\nu)|_0}{(g_{\mu\nu}\tilde{u}^\mu\tilde{k}^\nu)|_*} \\ &\simeq \frac{a_*}{a_0}\frac{\left(1-\boldsymbol{v}\cdot\hat{\boldsymbol{e}}+\Phi+\delta k^0\right)\big|_0}{\left(1-\boldsymbol{v}\cdot\hat{\boldsymbol{e}}+\Phi+\delta k^0\right)\big|_*} \simeq \frac{a_*}{a_0}\left\{1-\left[\boldsymbol{v}\cdot\hat{\boldsymbol{e}}-\Phi\right]_*^0+\left[\delta k^0\right]_*^0\right\} \\ &= \frac{a_*}{a_0}\left\{1-\left[\boldsymbol{v}\cdot\hat{\boldsymbol{e}}+\Phi\right]_{\lambda_*}^{\lambda_0}+\int_{\lambda_*}^{\lambda_0}\left(\Phi'+\Psi'\right)\mathrm{d}\lambda\right\}.\end{aligned} \tag{2.56}$$

Here $\boldsymbol{v}\cdot\hat{\boldsymbol{e}} \equiv \delta_{ij}\,v^i\,e^j$, the prime $'$ denotes a partial derivative w.r.t. conformal time, and the potentials are integrated along geodesics, that is, $\Phi' = \Phi'(\eta(\lambda), \mathbf{x}(\lambda))$ is understood.

Now recall that the CMB temperature falls as $T_0 = T_*/(1+z)$ and let $T_0(\hat{\boldsymbol{n}}) = \overline{T}_0 + \Delta T_0(\hat{\boldsymbol{n}})$ and $T_*(\hat{\boldsymbol{n}}) = \overline{T}_* + \Delta T_*(\hat{\boldsymbol{n}})$, where $\overline{T}(\propto a^{-1})$ is the unperturbed temperature of the FLRW background and $\hat{\boldsymbol{n}}$ is the direction of observation. Assuming the temperature fluctuations are small[7] we have

$$\frac{1}{1+z} = \frac{\overline{T}_0+\Delta T_0}{\overline{T}_*+\Delta T_*} \approx \frac{a_*}{a_0}\left(1+\frac{\Delta T_0}{\overline{T}_0}-\frac{\Delta T_*}{\overline{T}_*}\right), \tag{2.57}$$

and since $E_0/E_* = 1/(1+z)$, upon inserting into (2.56) and rearranging we finally have

$$\frac{\Delta T_0}{\overline{T}_0}(\hat{\boldsymbol{n}}) = \frac{\Delta T_*}{\overline{T}_*} - \left[\boldsymbol{v}\cdot(-\hat{\boldsymbol{n}})+\Phi\right]_{\lambda_*}^{\lambda_0} + \int_{\lambda_*}^{\lambda_0}\left(\Phi'+\Psi'\right)\mathrm{d}\lambda. \tag{2.58}$$

This is the first order temperature anisotropy observed in the direction $\hat{\boldsymbol{n}} = -\hat{\boldsymbol{e}}$ and at time t_0. The integral represents the ISW effect and generically means the frequency change arising from time-varying potentials, we emphasise that in the standard model it has often come to refer to the effect when only first order perturbation are considered. Note for Einstein-de Sitter models the ISW term vanishes (c.f. (2.11)).

The above derivation computed the ISW effect to linear order assuming that $|h_{\mu\nu}| \ll 1$ or, equivalently, that $|\Phi|$ and $|\Psi|$ are much less than unity. Clearly, nonlinear collapsed

[7] Indeed, the largest contribution is from the dipole, which is at the level of $10^{-3}\,\mathrm{K}$.

structures such as galaxies and clusters can also generate anisotropies in the CMB. The effect these structures have on the CMB is a nonlinear version of the ISW effect called the Rees-Sciama (RS) effect [123]. Whereas the ISW effect arises from first order density fluctuations the RS effect arises from the nonlinear density fluctuations characteristic of late epoch structure formation.[8]

Evaluating the ISW integral requires solutions to the null geodesic equations, which in turn requires determining the potentials Φ and Ψ explicitly from the lumpy distribution of matter. To linear order, often in the standard framework one simply evaluates the ray along the unperturbed trajectory $\boldsymbol{x}(\lambda) = \boldsymbol{x}_* + (\lambda - \lambda_*)\,\hat{\boldsymbol{e}}$, i.e., in Minkowski space. This is known as the *Born approximation* and simplifies numerical calculations as one simply ray traces along the line-of-sight, ignoring the null geodesic equations of the perturbed metric. As a result deflections in the trajectory are not considered, but will however affect the CMB.[9] These effects are treated separately from the ISW effect under the subject of weak lensing of the CMB [125].

By the Born approximation $k^\mu \simeq \bar{k}^\mu = \bar{u}^\mu + e^\mu$, from which we find that $k^\eta \simeq \bar{k}^\eta = \bar{u}^\eta = \delta^\eta{}_\eta = 1$, i.e., $\mathrm{d}\eta/\,\mathrm{d}\lambda \simeq 1$. Thus $\mathrm{d}\lambda \simeq \mathrm{d}\eta$ allowing us to rewrite the ISW term as

$$\left(\frac{\Delta T_0}{\overline{T}_0}\right)_{\mathrm{ISW}} \simeq \int_{\eta_*}^{\eta_0} (\Phi' + \Psi')\,\mathrm{d}\eta, \tag{2.59}$$

with $\Phi' = \Phi'(\eta, \boldsymbol{x}(\eta))$ and $\Psi' = \Psi'(\eta, \boldsymbol{x}(\eta))$.

The other terms in (2.58) are interpreted as follows

- $\boldsymbol{v} \cdot \hat{\boldsymbol{n}}$ is the kinematic dipole caused by the peculiar motion of the observer relative to the CMB rest frame.

- $\Phi(t(\lambda_*), \boldsymbol{x}(\lambda_*))$ is known as the ordinary Sachs-Wolfe effect. It reflects the fact that photons may be emitted inside potentials in which case they lose or gain energy leaving it.

- $\Phi(t(\lambda_0), \boldsymbol{x}(\lambda_0))$ is the monopole contribution due to the present day gravitational potential. Regardless of which direction the CMB is observed in, the temperature shift is the same.

[8] At late times of structure formation, the dark energy driven expansion causes a flattening of the potential but is somewhat cancelled out by matter collapsing under gravity. Treated as the source of the RS effect, this has the tendency of causing the potential Φ to grow and become steeper opposing the effects of expansion. Overall, the ISW effect dominates the RS effect at late times but going to larger redshift the roles reverse as the effects of dark energy become less prominent and matter comes to dominate.

[9] In the standard framework, the deflection angle depends on a term proportional to the transverse gradient of the potential Ψ, basically, the 'force' acts orthogonally to the ray so that it does not induce a change in frequency.

- $\Delta T_*/T_*$ is related to the intrinsic fluctuation in the radiation energy density (δ_γ). Using the Stefan-Boltzmann law $\rho_\gamma \propto \overline{T}^4$ we see that

$$\frac{\Delta T_*}{\overline{T}_*} = \frac{1}{4}\frac{\delta\rho_\gamma}{\rho_\gamma}\bigg|_* \equiv \frac{1}{4}\delta_\gamma\big|_*. \tag{2.60}$$

We remark that the standard interpretations immediately assume an operational interpretation which is open to debate, even in the standard model. In particular, linear perturbation theory is not valid on small scales, and consequently neither the monopole contribution $\Phi(t(\lambda_0), x(\lambda_0))$ to the CMB spectrum, nor the kinematic dipole $\boldsymbol{v}\cdot\hat{\boldsymbol{n}}$ relevant to our own observations can be estimated simply from perturbation theory. If one assumes that the FLRW geometry plus Newtonian N-body simulations are valid approximations for the actual universe, then one can estimate such quantities on the basis of many simulations. However, even state of the art simulations are still based on coarse graining dust as dark matter particles. The relationship between the *calibration* of effective potentials experienced by ordinary baryonic matter and dark matter is not known. Dark matter particles are simply assumed as a proxy for actual observers. Consequently, even in the standard framework there are aspects of the more general fitting problem [126,127] which are not widely addressed. However, some related observational issues have been recently discussed within the standard framework [72,128].

2.3 Statistics of the CMB

In order to quantify the observed temperature anisotropy, it is standard to expand $\Delta T/T$ in spherical harmonic functions $Y_{\ell m}(\hat{\boldsymbol{n}})$:

$$\Theta(\hat{\boldsymbol{n}}) \equiv \frac{\Delta T}{T}(\hat{\boldsymbol{n}}) = \sum_{\ell=0}^{\infty}\sum_{m=-\ell}^{\ell} a_{\ell m}\, Y_{\ell m}(\hat{\boldsymbol{n}}), \tag{2.61}$$

where ℓ is the multipole moment (or for short, the multipole), and again $\hat{\boldsymbol{n}}$ is a unit 3-vector in the direction of observation. The decomposition into spherical harmonics of any function on the sphere is unique. The set of spherical harmonics are orthonormal, in the sense that

$$\int Y_{\ell m}(\hat{\boldsymbol{n}})\, Y^*_{\ell' m'}(\hat{\boldsymbol{n}})\, \mathrm{d}\hat{\boldsymbol{n}} = \delta_{\ell\ell'}\delta_{mm'}, \tag{2.62}$$

and form a basis of functions on the unit sphere. Here the integral is over is over the sky and $\delta_{\ell\ell'}$ is the Kronecker delta symbol defined as $\delta_{\ell\ell'} = 1$ if $\ell = \ell'$ and zero otherwise. By (2.62) we then have

$$a_{\ell m} = \int \Theta(\hat{\boldsymbol{n}}) Y^*_{\ell m}(\hat{\boldsymbol{n}})\, \mathrm{d}\hat{\boldsymbol{n}}. \tag{2.63}$$

Spherical harmonic functions also satisfies the addition theorem,

$$\sum_m Y_{\ell m}(\hat{\boldsymbol{n}}) Y^*_{\ell m}(\hat{\boldsymbol{n}}') = \frac{2\ell+1}{4\pi} P_\ell(\hat{\boldsymbol{n}}\cdot\hat{\boldsymbol{n}}'), \tag{2.64}$$

where P_ℓ is the Legendre polynomial of order ℓ.

Note ℓ is inversely proportional to the angular scale so that small ℓ describes large angular scales etc. The coefficients $a_{\ell m}$ are complex numbers but $\Theta(\hat{\boldsymbol{n}})$ being real imposes $a^*_{\ell m} = (-1)^m a_{\ell -m}$ (following the Condon-Shortley convention [129]), with * denoting the complex conjugate. All cosmological information about the anisotropy field is encoded in these complex quantities.

In principle, we can conceive of an *ensemble* of universes, each a distinct realisation of the physical processes that governs a given cosmological model. It is the average over the ensemble, which we denote $\langle \mathcal{A} \rangle$ for some observable $\mathcal{A}$, that should be compared against the model. Given that we are only able to perform measurements in the universe in which we find ourselves, these averages cannot be performed. However, if one invokes the ergodic theorem[10] as is often done in the standard framework, the ensemble average can be traded for an average over positions in a single realisation. Thus, ensemble averages can, in principle, be done by measuring the CMB at different observational points. Showing that an underlying model has certain properties required for ergodicity is not straightforward requiring additional assumptions of the statistics of random fields. In the case of Gaussian random fields, ergodicity can be demonstrated (e.g., inflationary models predict Gaussian density perturbations).

Assuming $\Theta(\hat{\boldsymbol{n}})$ is statistically isotropic means the *2-point correlation function*

$$C(\hat{\boldsymbol{n}}, \hat{\boldsymbol{n}}') = \langle \Theta(\hat{\boldsymbol{n}}) \Theta(\hat{\boldsymbol{n}}') \rangle, \tag{2.65}$$

depends only on the angle θ between $\hat{\boldsymbol{n}}$ and $\hat{\boldsymbol{n}}'$, that is

$$C(\hat{\boldsymbol{n}}, \hat{\boldsymbol{n}}') = C(\hat{\boldsymbol{n}} \cdot \hat{\boldsymbol{n}}') = C(\theta), \tag{2.66}$$

and as such the correlation function is invariant under rotations $\hat{\boldsymbol{n}} \to R\hat{\boldsymbol{n}}$ and $\hat{\boldsymbol{n}}' \to R\hat{\boldsymbol{n}}'$. We emphasise that this does *not* imply $\Theta(R\hat{\boldsymbol{n}}) = \Theta(\hat{\boldsymbol{n}})$ but only that the *statistics* are preserved between points of a fixed angular separation.

Since $\hat{\boldsymbol{n}} \cdot \hat{\boldsymbol{n}}' = \cos\theta \in [-1, 1]$ let us expand the correlation function in terms of Legendre polynomials $P_\ell(\cos\theta)$:

$$C(\theta) = \langle \Theta(\hat{\boldsymbol{n}}) \Theta(\hat{\boldsymbol{n}}') \rangle \tag{2.67a}$$

$$= \sum_\ell \frac{2\ell + 1}{4\pi} C_\ell P_\ell(\cos\theta). \tag{2.67b}$$

Note the factor $(2\ell + 1)/4\pi$ has been extracted from the basis coefficients C_ℓ as this will simplify the following calculations. Using (2.61) on the right-hand side of (2.67a) and

[10] While the assumption of ergodicity is clearly relevant in isolated systems in statistical physics, this assumption might be questioned for the whole universe, which is not close to any equilibrium state over long periods of time. The application of this assumption to primordial fluctuations is an additional physical ingredient for models of the very early universe, such as inflation.

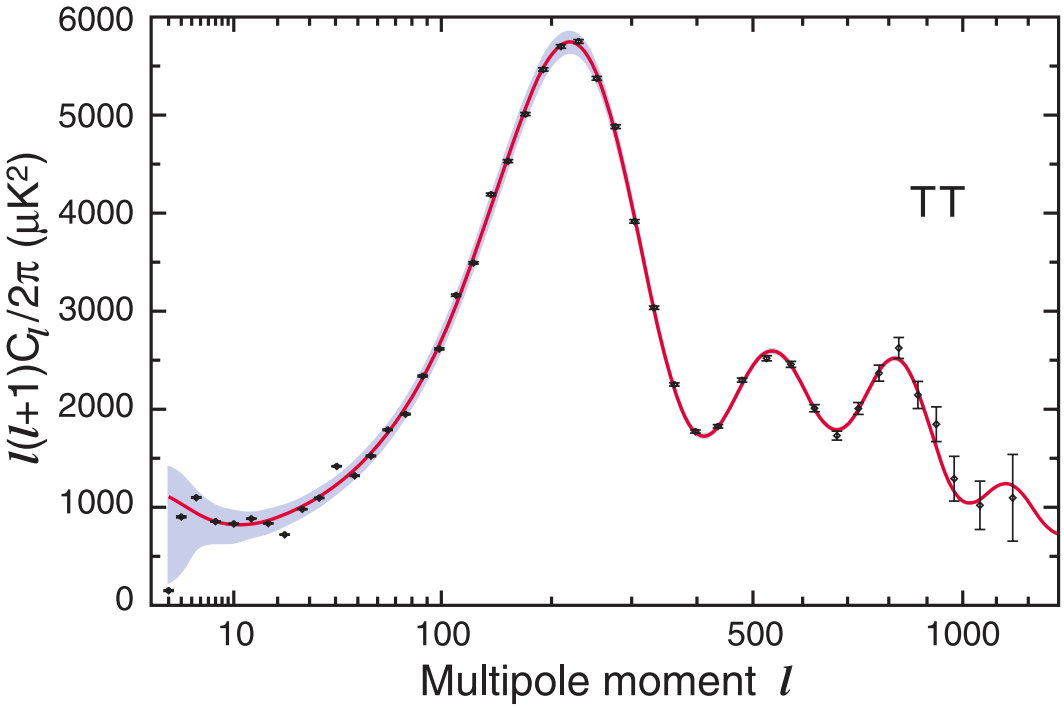

Figure 2.1: The CMB angular power spectrum for $\ell \geq 2$ of 9-year *WMAP* measurements. The red curve is the theoretical curve of the best-fit ΛCDM model while the blue band shows the cosmic variance. The region $\ell \sim 10$ is known as the Sachs-Wolfe plateau due to the power $\ell(\ell+1)C_\ell$ being roughly flat, though it is less apparent here with the logarithmic scale more compressed towards lower ℓ. (Credit: *WMAP* collaboration)

the addition theorem (2.64) on (2.67b) we obtain the relation

$$\sum_{\ell m \ell' m'} \langle a_{\ell m} a^*_{\ell' m'} \rangle Y_{\ell m}(\hat{\boldsymbol{n}}) Y^*_{\ell' m'}(\hat{\boldsymbol{n}}') = \sum_{\ell m} C_\ell Y_{\ell m}(\hat{\boldsymbol{n}}) Y^*_{\ell m}(\hat{\boldsymbol{n}}'). \tag{2.68}$$

Multiplying both sides by $Y^*_{\ell_1 m_1}(\hat{\boldsymbol{n}}) Y_{\ell_2 m_2}(\hat{\boldsymbol{n}}')$, then integrating over $\hat{\boldsymbol{n}}$ and $\hat{\boldsymbol{n}}'$, and using the orthogonality relation (2.62), we find

$$\langle a_{\ell m} a^*_{\ell' m'} \rangle = C_\ell \, \delta_{\ell \ell'} \, \delta_{m m'}. \tag{2.69}$$

Thus, for a statistically isotropic field $\Theta(\hat{\boldsymbol{n}})$ the *angular power spectrum* $C_\ell = \langle |a_{\ell m}|^2 \rangle$ encodes the same information as $C(\theta)$. We can then equivalently think of the statistics in real space, associated with the correlation function, or harmonic space, associated with the power spectrum. Though from a practical standpoint there are significant computational advantages using the latter. Another reason is the power spectrum can be directly compared among different experiments (e.g. *Planck* and *WMAP*), whereas the correlation function will depend on the angular resolution of the experiment.

We observe $C_\ell = \langle |a_{\ell m}|^2 \rangle$ depends only on ℓ and not on the rotational degrees of freedom m; this is as we would expect since we have assumed statistical isotropy. Thus, for a given ℓ we have at most a sample of $2\ell + 1$ measurements of C_ℓ, one for each m.[11]

[11]Often the power spectrum C_ℓ of temperature fluctuations is denoted C_ℓ^{TT} to distinguish between

With the further assumption that $\Theta(\hat{\boldsymbol{n}})$ is Gaussian random field we have $\langle\Theta(\hat{\boldsymbol{n}})\rangle = 0$ or equivalently $\langle a_{\ell m}\rangle = 0$. Each $a_{\ell m}$ is then a Gaussian random variable with mean zero and variance $C_\ell = \langle|a_{\ell m}|^2\rangle$. All n-point correlation functions (n products of $\Theta(\hat{\boldsymbol{n}})$) reduce down to the sum of the products of 2-point correlation functions (2.67a), a result that tells us that the statistics of $\Theta(\hat{\boldsymbol{n}})$ is described entirely by the angular power spectrum.

2.3.1 Cosmic variance

In the previous section we discussed the angular power spectrum in terms of abstract ensemble averages, that is, averages over many realisations of the same underlying universe. In the real world cosmological data comes to us from all but one realisation, meaning that at best all we can do is estimate the true power spectrum.

Assuming statistical isotropy, the simplest estimator of the power spectrum uses the fact that C_ℓ is independent of m so one has $2\ell+1$ different measurements, one for each m. Thus for a given ℓ one just takes the arithmetic average

$$\tilde{C}_\ell \equiv \frac{1}{2\ell+1}\sum_{m=-\ell}^{\ell}|a_{\ell m}|^2, \tag{2.70}$$

with $|a_{\ell m}|^2 = a_{\ell m}a^*_{\ell m}$. This is known as the *pseudo-C_ℓ* (PCL) *estimator* [171] and is unbiased, that is, $\langle\tilde{C}_\ell\rangle = C_\ell$. It is to be compared with the true C_ℓ.[12] Assuming that $\Theta(\hat{\boldsymbol{n}})$ obeys Gaussian statistics (as is done in the standard model), and applying Wick's theorem we find[13] that

$$\mathrm{Var}[\tilde{C}_\ell] \equiv \left\langle (C_\ell - \tilde{C}_\ell)^2 \right\rangle = \frac{2}{2\ell+1}C_\ell^2. \tag{2.71}$$

This is known as *cosmic variance* and represents an intrinsic uncertainty due to the fact that we observe a single realisation. Even with perfect instruments and full-sky coverage one can do no better than this uncertainty. Cosmic variance affects all angular scales but is particularly significant on large angular scales, corresponding to large scale structure (see fig. 2.1).

The power at low multipoles are thought to come mainly from the primordial epoch when the power spectrum would have been close to scale-invariant, i.e., one would measure at this epoch $\ell(\ell+1)C_\ell \simeq$ const. The power spectrum measured today has largely been processed by a range of effects, (e.g., Baryon Acoustic Oscillations, Silk damping, etc) to

other power spectra. So far we have focused on scalar fluctuations in the CMB temperature field, but the CMB is also polarised. There are two types, so-called E-modes and B-modes, and one often constructs the *cross*-power spectra, e.g., C_ℓ^{TE}, C_ℓ^{TB}, C_ℓ^{EB} etc. Henceforth, since we do not investigate polarisation we will simply denote C_ℓ^{TT} as C_ℓ.

[12] This estimator (2.70) assumes an ideal full-sky coverage of the CMB so that each $a_{\ell m}$ can be measured, however, in practice the sky is obscured by foregrounds such as galactic dust and galactic synchrotron emission, and will suffer from instrument noise. Estimators may also be constructed taking partial sky coverage into consideration (see e.g. [132]).

[13] Again, see §2.6 of [133] for details.

arrive at fig. 2.1. At low ℓ the spectrum remains relatively flat, suggesting the power at these scales is mostly of a primordial origin. This region is commonly referred to as the Sachs-Wolfe plateau (c.f. (2.58)).

2.4 Detecting the ISW effect

As we saw above the linear ISW effect in a perturbed Friedmann cosmology arises from the time-evolution of the Newtonian and curvature potentials. In the standard model, the stretching and flattening of the potentials is caused by the expansion of the universe; at late times the apparent acceleration is brought on by dark energy producing a significant ISW signature in the CMB anisotropy. By this token, the ISW effect can be used to constrain the cosmological constant in the standard ΛCDM model. Curvature can also affect the ISW signature but in ΛCDM this is of course negligible so that dark energy can be directly probed.

However, given that the contribution from ISW to the temperature shift $\Delta T/T$ is small—about an order of magnitude smaller than the primary anisotropies— detecting it directly from the CMB proves difficult. Low multipoles, corresponding to large scale structures, in the angular power spectrum have low power (or amplitude) compared with intrinsic fluctuations and also suffer from cosmic variance[14], which is particularly acute on large scales.

Cross-correlations with tracers. An alternative method was proposed by Crittenden and Turok [134]. The idea is that the ISW signature should in principle be correlated with local matter tracers since we see that the potential Φ is related to the density contrast δ through the Poisson equation (2.6c). In turn, the density contrast can be expected to be related to the density of galaxies and quasars. The relation between the matter distribution δ and the galaxy distribution δ_g will generally be biased [135], usually linearly as $\delta_g = b\delta$ where the constant b is the bias parameter.

This is the basis of many efforts today to detect the ISW signal and, indirectly, dark energy from cross-correlation of the temperature map with matter tracers (or the absence thereof).

With the arrival of *WMAP* and more recently *Planck* CMB data, many detections of the ISW signal have been reported using the above method (see Table 1 of [132] and [136] for a summary of recent results). Tracer objects are found through observations of electromagnetic waves in optical wavelengths (Sloan Digital Sky Survey (SDSS) Luminous Red Galaxies and Quasars), radio wavelengths (NVRAO VLA Sky Survey (NVSS)) among others. Many signals tend to be weak (2–3 σ significant) although, notably, Giannantonio

[14]Cosmic variance can be thought of as the inherent limit on the amount of information that can be measured on large scales. Unlike the usual concept variance, cosmic variance cannot be avoided.

et al. [137] find a $4.5\,\sigma$ signal. Their method combines tracer data from six different surveys, however, such a large signal should be interpreted cautiously because of problems in estimating errors associated with correlated data sets.

Stacking superstructures. In theory, overdense and underdense superstructures should be correlated with hot and cold regions respectively in the CMB temperature map, that is, large scale structures are expected to be 'imprinted' on the CMB. However, in practice the ISW signal coming from individual superstructures is too weak to be detected due to the significant amount of noise from primary anisotropies. By averaging or 'stacking' N superstructures, such as supervoids or superclusters, the signal-to-noise can be improved as the noise from uncorrelated primary anisotropies falls as $\propto 1/\sqrt{N}$. This method was used by Granett et al. [138] to detect an ISW signal with a temperature shift of $\sim -11\,\mu\mathrm{K}$ at $3.7\,\sigma$ significance for supervoids, $\sim 8\,\mu\mathrm{K}$ at $2.6\,\sigma$ for superclusters, and an absolute temperature shift averaged over both supervoids and superclusters of $9.6\,\mu\mathrm{K}$ at $>4\,\sigma$ significance. The stacking method involves superposing cutouts of the CMB temperature map at the locations of supervoids and superclusters as determined by luminous red galaxies (LRG) in the SDSS catalogue. In the sample the superstructures used are at a redshift of ~ 0.5 and size $\sim 100\,h^{-1}\,\mathrm{Mpc}$. Interpreted in the standard model, the hot and cold spots are seen as evidence for a late time ISW effect caused by the onset of dark energy domination.

The high amplitude and statistical significance reported by Granett et al. is the focus of much debate. The typical amplitude $|\Delta T|$ detected by tracers is much smaller than when using stacked supervoids/clusters and falls in line with the ΛCDM expectation. Interestingly, the *Planck* team [139] find a signal for both supervoids and superclusters consistent with the temperature shift ΔT found by Granett et al. when using the same sample of superstructures but supplemented with CMB polarisation data. (As it turns out, they do not find any correlation of polarisation with the signal). However, using CMB-tracer cross-correlations the *Planck* team results are otherwise consistent with ΛCDM levels.

Compared with the value predicted by the standard model, the observed temperature deviation $\sim 9\,\mu\mathrm{K}$ is far larger. Nadathur et al. [140] estimate the expected value $\langle \Delta T \rangle$ from an ensemble of supervoids[15] of size $\sim 100\,h^{-1}\,\mathrm{Mpc}$ and different (central) density contrasts $\delta_{\min}$ based on the standard ΛCDM model finding a temperature deviation of $\Delta T \lesssim 2\,\mu\mathrm{K}$ in ΛCDM—a value which is discrepant with [138] by $>3\,\sigma$.

The calculation uses the linear growth approximation in which all scales grow at the same rate. Moreover it assumes that: (i) the density contrast when smoothed on some scale is a Gaussian random field so that large scale structures are given by linear fluctuations, $\delta \lesssim 1$ and that, (ii) locally the density field around superstructures are

[15] Supervoids are less prone than superclusters to selection effects in superstructure finding algorithms.

on average spherically symmetric with the density profile given in [141]. The density amplitudes and radii of the profile are chosen from a distribution to produce the largest possible estimate. The potential Φ is found from the Poisson equation (2.6c) and the temperature map $\Delta T/T$ can then be constructed using (2.59) for different lines-of-sight $\vec{n}$. In the context of the standard model we note in passing that the nonlinear contribution to the full nonlinear ISW effect is thought to be small at low redshifts [142].

Flender et al. [143] subsequently used a slightly modified approach to [140] with the aim of achieving the largest ISW effect in ΛCDM, still find that the discrepancy of Granett et al. persists at $>3\,\sigma$. Moreover, this result is robust against varying the cosmological parameters in ΛCDM and also possible selection effects of the sample. They also argued unlikely that unidentified systematics and galactic foregrounds can account for this tension.

Very recently, Nadathur and Crittenden [144] introduced a new matched filtering approach for detection of the ISW effect, which they claim is not subject to an *a posteriori* bias in the way that earlier techniques were. They apply their method to *Planck* CMB data using voids and superclusters identified in the CMASS galaxy data from the Sloan Digital Sky Survey Data Release 12. They detect the ISW effect with at a $3.1\,\sigma$ significance, but contrary to earlier results its amplitude $A_{\rm ISW} = 1.64 \pm 0.53$ relative to the ΛCDM expectation is in agreement with the predictions of the standard cosmology.

The Cold Spot. The recent discovery of a supervoid [145] in the direction of the CMB Cold Spot seemed to suggest that its temperature fluctuation $\sim -150\,\mu$K could be the result of the ISW and RS effects. In fact, one group claimed that this supervoid could entirely account for the Cold Spot [146]. Centred at a redshift $z = 0.155$ with a size of $\sim 200\,h^{-1}\,$Mpc and central density contrast of $\delta_0 = -0.25$, the supervoid was reported to produce a RS effect an order of magnitude larger than the ISW effect contrary to the results of [142] that the RS effect is negligible for $z \lesssim 1$. In a more detailed study by [147] the authors dispute this claim showing that when the void is modelled either perturbatively or exactly using an LTB model it is unable to explain the temperature profile. Following this work, the authors of [146] revise their paper and come to a similar conclusion.

It is shown in [147] that the RS contribution is in fact two orders of magnitude smaller than from the ISW effect, which gives $\sim -20\,\mu$K. This is not surprising as the second order perturbations should provide corrections to the linear order calculation if the linearised theory is to be valid. Moreover, they argue that supervoids such as the one detected are not as uncommon as first thought with ~ 20 voids of a similar nature expected to be found with a redshift less than ~ 0.5.

They conclude that the size and density contrast of a supervoid required to match the observed signal would need be so severe as to be improbable in the standard model.

N-body simulations. A higher than expected temperature decrement can also be seen in N-body simulations. For instance, Granett et al. compared their stacked imprint to the ΛCDM prediction using a $500\,h^{-1}$ Mpc length box simulation finding that the region giving largest ISW signal was still $\sim 2\,\sigma$ different to the stacked result.

N-body simulations have also been used to study the nonlinear regime. In [142] a $1\,h^{-3}\,\mathrm{Gpc}^3$ size simulation showed by ray tracing that the RS effect is subdominant to the ISW effect at late times but dominates in the matter dominated epoch. A much larger simulation ($216h^{-3}\,\mathrm{Gpc}^3$) finds that the ISW signal from structures with redshift less than 1.4 is no more than $\sim 50\,\mu\mathrm{K}$ over the whole sky [148].

The ongoing debate about observations of the amplitude of the ISW effect involves very complex issues of statistics and *a posteriori* selection effects, as well as the statistics of Newtonian N–body numerical simulations. It is important to have other realistic models beyond the standard cosmology which might potentially lead to differences that might be further tested. This motivates the study of exact inhomogeneous solutions of Einstein's equations, to which we now turn.

Chapter 3

Exact Cosmological Models

In the previous chapter we reviewed the standard model approach to modelling inhomogeneities in the Universe, namely using linear cosmological perturbation theory. Given the complexity of the late epoch Universe we saw how perturbation theory fails to describe the small scales (tens of megaparsecs) of realistic structures such as voids and clusters.

While perturbation theory offers semi-analytical predictions there is no substitute to models based on full general relativity. However, constructing a model of the universe based on exact solutions to the Einstein equations, which takes into account the statistical spatial homogeneity on scales $\gtrsim 100h^{-1}$ Mpc and the emergence of the cosmic web of the late epoch universe, is a very difficult task (as we discussed in §1.2.4 and §1.1.4). It took decades to successfully solve even just the 2-body problem numerically in general relativity [149].

In the last year two teams [150, 151] have begun the extremely complex problem of computational cosmology based on general relativity using the Baumgarte-Shapiro-Shibata-Nakamura (BSSN) formalism [152]. These numerical calculations assume an initial global FLRW geometry in the dust dominated epoch, and must make particular choices of slicing by hypersurfaces, gauge choices for coordinates, and assumptions of initial density perturbations of the early universe, (e.g., Bentivegna & Bruni [151] assume a simple periodic initial perturbation, which has an unrealistically high degree of symmetry). Nonetheless, even with as yet crude approximations, some deviations from the expectations of the standard cosmology have been found. In particular, the variation of local expansion is larger than in the standard approach.

In this thesis we approach the fully nonlinear problem by the alternative approach of embedding small scale exact solutions within a standard FLRW model corresponding to the ΛCDM cosmology.

This chapter is dedicated to the subject of modelling inhomogeneous structures using exact solutions of general relativity. Being non-perturbative, these models allow an exact description of cosmological structures on scales $< 100h^{-1}$ Mpc that are largely ignored

in the standard framework (at least in the relativistic context).

3.1 The Lemaître-Tolman-Bondi solution

The Lemaître-Tolman-Bondi (LTB) models [42–44] are a class of spherically symmetric, time-dependent solutions with the right-hand side of the Einstein field equations specified by a pressureless fluid, i.e., dust. (In fact Lemaître originally studied the more general case involving pressure [42].) In this section we derive the solution and discuss the theory, properties, pathologies and basic tools of LTB models.

To obtain the LTB solution we begin by noting that a spherically symmetric metric in coordinates comoving with the dust has the general form

$$\mathrm{d}s^2 = g_{\mu\nu}\,\mathrm{d}x^\mu\,\mathrm{d}x^\nu = -\mathrm{e}^{2\nu(t,r)}\,\mathrm{d}t^2 + \mathrm{e}^{2\lambda(t,r)}\,\mathrm{d}r^2 + R^2(t,r)\,\mathrm{d}\Omega^2. \tag{3.1}$$

The conditions on $\nu(t,r)$, $\lambda(t,r)$ and $R(t,r)$ are found by inserting the ansatz into the Einstein field equations

$$G_{\mu\nu} = \kappa T_{\mu\nu} - \Lambda g_{\mu\nu}, \tag{3.2}$$

where $G_{\mu\nu} = \mathcal{R}_{\mu\nu} - \frac{1}{2}\mathcal{R}g_{\mu\nu}$ is the Einstein tensor, $\mathcal{R}_{\mu\nu}$ is the Ricci tensor, $\mathcal{R} \equiv g^{\mu\nu}\mathcal{R}_{\mu\nu}$, $\kappa \equiv 8\pi G/c^4 = 8\pi$ and

$$T_{\mu\nu} = \rho(t,r)\,u_\mu u_\nu,$$

is the energy-momentum tensor of dust. Here u^μ is the dust 4-velocity field, $\rho(t,r)$ the dust density and $\mathrm{d}\Omega^2 = \mathrm{d}\theta^2 + \sin^2\theta\,\mathrm{d}\phi^2$ is the 2-sphere metric. For a universe containing dust matter only, it follows from $T^{\mu\nu}{}_{;\nu} = 0$ that $u^\nu\nabla_\nu u^\mu = 0$, i.e., the dust flow follows (timelike) geodesics. Because of spherical symmetry the dust flow is purely radial, and as a result rotation free so that we may choose synchronous coordinates [153] in which we can set $\mathrm{e}^{2\nu} = 1$. Thus coordinate time coincides with proper time τ. Dust particles are labelled by the single coordinate r on account of spherical symmetry and parametrised by t so that $u^\mu = \frac{\mathrm{d}x^\mu}{\mathrm{d}\tau} = \delta^\mu{}_t = (1,0,0,0)$. The only field equations we need to consider are

$$G^t{}_r = 2\frac{\dot{R}'}{R} - 2\frac{R'}{R}\dot{\lambda} = 0, \tag{3.3a}$$

$$G^r{}_r = \frac{R'^2}{R^2}\mathrm{e}^{-2\lambda} - 2\frac{\ddot{R}}{R} - \frac{\dot{R}^2}{R^2} - \frac{1}{R^2} = -\Lambda, \tag{3.3b}$$

$$G^t{}_t = \mathrm{e}^{-2\lambda}\left(\frac{R'^2}{R^2} + 2\frac{R''}{R} - 2\frac{R'}{R}\lambda'\right) - \frac{\dot{R}^2}{R^2} - 2\frac{\dot{R}}{R}\dot{\lambda} - \frac{1}{R^2} = -8\pi\rho - \Lambda. \tag{3.3c}$$

Here we use the shorthand that an overdot denotes the partial derivative $\partial/\partial t$, and a prime the partial derivative $\partial/\partial r$, so that $\dot{R}' \equiv R_{,rt}$ etc. All other field equations are either satisfied identically or provide no new independent equations. Equation (3.3a)

admits a first integral $f(r) \equiv 1 + 2E(r) \geq 0$ and so we find

$$\mathrm{e}^{2\lambda(t,r)} = \frac{R'^2}{1+2E}. \tag{3.4}$$

Written in this way $E(r)$ is an arbitrary function, so long as $E(r) \geq -\frac{1}{2}$. Equality, $E = -\frac{1}{2}$, can be achieved provided $R' = 0$. The function $E(r)$ determines the spatial curvature of a hypersurface of constant t but can also be interpreted as the energy per unit mass of the dust. Note the denominator is written in this way for convenience only; it simplifies solving the other equations.

By multiplying (3.3b) by $\dot{R}R^2$, then integrating by t we obtain

$$\dot{R}^2 = \frac{2M}{R} + 2E + \frac{1}{3}\Lambda R^2, \tag{3.5}$$

where $M(r)$ is a first integral. This is the only dynamical equation of the LTB solution. The arbitrary function $M(r)$ represents the effective gravitating mass contained in a shell of radius r.

Notice that this equation only involves a t partial derivative whereas R is a function of t and r meaning that the initial condition is specified by some arbitrary function of r. By simple rearrangement of (3.5) we find

$$t - t_b(r) = \int_0^{R(t,r)} \frac{\mathrm{d}\tilde{R}}{\sqrt{2M/\tilde{R} + 2E + \Lambda\tilde{R}^2/3}}, \tag{3.6}$$

where the arbitrary function $t_b(r)$ is known as the 'bang time', the time at which $R(t_b(r), r) = 0$ meaning that the big bang need not occur everywhere at 'once' but can vary with position. In general, (3.5) is solved numerically since it does not permit a solution in terms of elementary functions, except in the special case $\Lambda = 0$ (see §3.1.1).

Using (3.4) and (3.5) in equation (3.3c) above we obtain

$$8\pi\rho(t,r) = \frac{2M'}{R'R^2}. \tag{3.7}$$

The LTB line element in comoving-synchronous coordinates now reads

$$\mathrm{d}s^2 = -\,\mathrm{d}t^2 + \frac{R'^2}{1+2E}\,\mathrm{d}r^2 + R^2\,\mathrm{d}\Omega^2, \tag{3.8}$$

with $R(t,r)$ given by solving (3.5).

Specifying $E(r)$, $M(r)$ and $t_b(r)$ determines the LTB model completely. Notice that (3.7) and (3.8) are covariant w.r.t. r, i.e., there remains a coordinate freedom $r \to \tilde{r} = f(r)$ and this can be chosen to fix the scale but can also be used to redefine one of the three functions in a more convenient form. Therefore, only two of the above functions are independent with a gauge specified.

We note here the Hubble expansion rate, in general, may be defined as

$$H(t,r) \equiv \frac{1}{3}\Theta = \frac{1}{3}\nabla_\mu u^\mu = \frac{1}{3}\left(\frac{2\dot{R}}{R} + \frac{\dot{R}'}{R'}\right), \tag{3.9}$$

where the kinematic scalar $\Theta \equiv \nabla_\mu u^\mu$ is the fluid expansion [154] and in the FLRW limit $H = \dot{a}/a$

Note $M(r)$ is not the same as the total mass of all particles integrated over the same ball which would instead be

$$\begin{aligned}\mathcal{M}(r) &= \int_V \rho(t,r)\sqrt{{}^3g}\,\mathrm{d}^3x \\ &= 4\pi\int_0^r \rho\frac{R^2R'}{\sqrt{1+2E}}\,\mathrm{d}\tilde{r} = \int_0^r \frac{M'(\tilde{r})}{\sqrt{1+2E(\tilde{r})}}\,\mathrm{d}\tilde{r}\end{aligned} \tag{3.10}$$

and as we can see the total Newtonian mass differs from $M(r)$ by a factor $\sqrt{1+2E(r)}$. The difference is known as the mass defect in bound gravitational systems. Moreover we see $\mathcal{M}'\sqrt{1+2E} = M'$.

3.1.1 Parametric solutions in the case $\Lambda = 0$

As noted above, when $\Lambda \neq 0$, (3.5) cannot be solved by hand but involves elliptical integrals that cannot be expressed in terms of elementary functions (though Valkenburg [155] has reformulated (3.5) in Carlson's symmetric form of elliptic integrals). In the special case $\Lambda = 0$ this equation has the following parametric solutions:

- If $E(r) > 0$ then evolution is *hyperbolic*:

$$R(t,r) = \frac{M}{2E}(\cosh u - 1), \tag{3.11a}$$

$$t - t_b(r) = \frac{M}{(2E)^{3/2}}(\sinh u - u), \qquad 0 \le u < \infty. \tag{3.11b}$$

- If $E(r) = 0$ then evolution is *parabolic*:

$$R(t,r) = \left[\frac{9M}{2}\left(t - t_b(r)\right)^2\right]^{1/3}. \tag{3.12}$$

- IF $E(r) < 0$ then evolution is *elliptic*:

$$R(t,r) = \frac{M}{(-2E)}(1 - \cos u), \tag{3.13a}$$

$$t - t_b(r) = \frac{M}{(-2E)^{3/2}}(u - \sin u), \qquad 0 \le u \le 2\pi. \tag{3.13b}$$

In the last case, each spherical dust shell labelled r is expanding ($\dot{R} > 0$) until it reaches a maximum size at $u = \pi$ corresponding to a critical $\pi M/(-2E)^{3/2}$, at which point it begins to collapse returning to a singular state after a total time

$$t_c - t_b(r) = 2\pi M/(-2E)^{3/2}, \tag{3.14}$$

where t_c is known as the crunch time. (In the FLRW limit, described in the next section, $M/(-2E)^{3/2}(r) = \text{const}$ so the crunch time is simultaneous for all shells.) Such models are suited to describing the evolution of bound overdense spherical structure such as galaxy clusters (see, for example [156]).

On the other hand, provided no shell crossings occur (see below), choosing a function $E(r) < 0$ ensures that shells will continue to expand since if $\Lambda > 0$, as is true for most cosmological models of interest, then by (3.5) we have $\dot{R} > 0$ for all t.

3.1.2 Recovering the FLRW limit

The spatially homogeneous and isotropic Friedmann-Lemaître-Robinson-Walker (FLRW) dust solutions are the class of LTB models in which $t_b = \text{const}$ and $E/M^{2/3} = \text{const}$. (In fact, these are necessary and sufficient conditions.) To recover the standard Friedmann equation one chooses

$$M(r) = M_0 r^3,$$
$$E(r) = -\frac{1}{2}kr^2,$$

for some constant k. The scale function then factorises as $R(t, r) = a(t)r$ where $a(t)$ is the usual scale factor appearing in the Friedmann equation.

We remark that by setting $M(r) = \text{const}$ and $\Lambda = 0$ then it follows (3.7) that $\rho = 0$, i.e., the metric is a vacuum solution. Indeed, since the solution is spherically symmetric, by Birkhoff's theorem, the metric must be given by the exterior Schwarzschild metric and when given in Lemaître-Novikov coordinates the metric will be of the form (3.8). The remaining functions remain arbitrary with E representing the energy of a test particle and $2M$ being the Schwarzschild radius.

3.1.3 Prescribing LTB models

LTB models are often used to study inhomogeneous cosmologies embedded in a Friedmann background in which $E(r)$, $M(r)$ and $t_b(r)$ asymptotically approaches the FLRW values $E(r) = \text{const}$, $M(r) = M_0 r^3$ and $t_b(r) = \text{const}$, as $r \to \infty$. Alternatively, one is often interested in modelling individual inhomogeneities of a finite size within the LTB framework. Here the inhomogeneity has a comoving radius r_b beyond which the model becomes FLRW. This is the case for LTB Swiss cheese in §3.3 below.

The second of these two inhomogeneous models can be defined in the following way. The coordinate r is chosen such that at some initial time $R(t_i, r) = a_i r$ where $a_i = a(t_i)$ is the FLRW scale factor. We also demand that $\dot{R}(t_i, r) = \dot{a}_i r = a_i H_i r$ where H_i is the Hubble parameter of the background FLRW model. Thus the inhomogeneity at this epoch is contained in the density profile, and is related to the background density by $\rho(t_i, r) = \bar{\rho}(t_i)(1+\delta(t_i, r))$. The model is then completely determined by $\{R(t_i, r), \dot{R}(t_i, r), \rho(t_i, r)\}$.

With these functions chosen $M(r)$ is found by integrating (3.7) to get

$$M(r) = 4\pi \int_0^r \rho(t_i, \tilde{r}) R(t_i, \tilde{r})^2 R'(t_i, \tilde{r}) \, \mathrm{d}\tilde{r} = 4\pi a_i^3 \int_0^r \rho(t_i, \tilde{r}) \tilde{r}^2 \, \mathrm{d}\tilde{r}, \tag{3.15}$$

while the function $E(r)$ is obtained from (3.5) by setting $t = t_i$. Finally, the bang time is then found from (3.6) at $t = t_i$. Thus, specifying $\{R(t_i, r), \dot{R}(t_i, r), \rho(t_i, r)\}$ translates into a choice of $\{E(r), M(r), t_b(r)\}$.

Alternative methods

Rather than specifying the arbitrary functions outright, often it is more practical to specify an initial and/or final density profile since these can readily be chosen based on observational data. The following methods for $\Lambda = 0$ models are due to Krasinski and Hellaby [157, 158]. In these models the coordinate r is defined as $r = M$ and the density profile is specified at times t_1 and t_2. With this coordinate choice it follows from (3.7) that R can be directly evaluated from the profile as

$$R^3(t, M) = \int_0^M \frac{3}{4\pi\rho(t, \tilde{M})} \, \mathrm{d}\tilde{M}. \tag{3.16}$$

The remaining functions $E(r)$ and $t_b(r)$ are found directly from the parametric solutions above (§3.1.1).

Not all initial states are compatible with each other, but must satisfy a certain inequality. For example, in the case of $E > 0$, the following must be true:

$$t_2 - t_1 < \frac{\sqrt{2}}{3\sqrt{M}} \left(R^{3/2}(t_2, M) - R^{3/2}(t_1, M) \right). \tag{3.17}$$

The inequalities for other types of LTB models can be found in [157].

In fact, there are myriad other data that can be used to define LTB models. For instance, the velocity profile defined as $b(M) \equiv \dot{R}(t_i, M)/M^{1/3}$ can also define the model. What is more, initial and final data need not be of the same type. For example, one can specify a velocity profile at t_1 and a density profile at t_2 etc. For a list of valid data see §2.1.6 of [156].

3.1.4 Growing and decaying modes

Similarly to perturbed FLRW cosmologies, the evolution of LTB spacetimes can be characterised by growing and decaying modes, i.e., fluctuations that increase or decrease with

time respectively. In [159], the growing and decaying modes were studied for cases $\Lambda > 0$. This is summarised below.

The line element is recast in a way that it resembles the FLRW line element by redefining the quantities as $R(t,r) = a(t,r)r$, $2E(r) = -k(r)r^2$ while the coordinate r is defined so that $M(r) = M_0 r^3$ and t_b is chosen to be constant. The line element (3.8) then becomes

$$\mathrm{d}s^2 = -\,\mathrm{d}t^2 + a^2\left[(1-\Delta)^2\frac{\mathrm{d}r^2}{1-kr^2} + r^2\,\mathrm{d}\Omega^2\right], \tag{3.18}$$

where

$$\Delta(t,r) \equiv 1 - 3\frac{MR'}{M'R} = 1 - r\frac{a'}{a}, \tag{3.19}$$

and $a(t,r)$ is a solution to the equation

$$\dot{a}^2(t,r) = \frac{2M_0}{a(t,r)} - k(r) + \frac{\Lambda a^2(t,r)}{3}. \tag{3.20}$$

This has essentially the same form as the Friedmann equation except now a and k depend on r. For each r the associated dust shell worldline is precisely the same as its corresponding FLRW model in which $k = \text{const} = k(r)$ and $t_b = \text{const} = t_b(r)$. Thus, locally the evolution of dust shells are identical to FLRW dust models.

The quantity $\Delta(t,r)$ has a geometrical nature having the elegant form

$$\Delta^2 = \frac{9}{16}\frac{C_{\mu\sigma\rho\lambda}C^{\mu\sigma\rho\lambda}}{\mathcal{R}_{\mu\nu}\mathcal{R}^{\mu\nu} - \frac{1}{4}\mathcal{R}^2}. \tag{3.21}$$

We see that $\Delta \propto w$ where $w = C_{\mu\sigma\rho\lambda}C^{\mu\sigma\rho\lambda}$ is the Weyl scalar and in fact $\Delta = 0$ is a necessary and sufficient condition to obtain the FLRW limit [159]. Recall $C_{\mu\sigma\rho\lambda} = 0$ for FLRW metrics so we see at once $\Delta = 0$. To show that $\Delta = 0$ implies the FLRW metric we solve $1 - 3MR'/M'R = 0$ to find $R(t,r) = aM^{1/3}$, then substitute into (3.5) from which it follows that

$$\frac{E(r)}{M^{2/3}(r)} = \text{const}, \tag{3.22}$$

precisely the condition (together with $t_b = \text{const}$) needed to recover the FLRW limit.

Evaluating (3.21) using the field equations we find

$$\Delta(t,r) = \frac{\rho - M/(4\pi R^3/3)}{\rho}, \tag{3.23}$$

so that it can be physically interpreted as the density contrast. Using (3.5) and differentiating $\Delta = 1 - ra'/a$ by t it can be shown that Δ satisfies the exact equation

$$\ddot{\Delta} + 2\frac{\dot{a}}{a}\dot{\Delta} - 3\frac{M_0}{a^3}\Delta = 0. \tag{3.24}$$

This equation has a similar form to the equation

$$\ddot{\delta} + 2H\dot{\delta} - 4\pi\bar{\rho}\delta = 0, \tag{3.25}$$

governing the leading order evolution of the density contrast δ from perturbed FLRW cosmologies. (Note H is the Hubble parameter of the FLRW background.) In fact, these equations have the same form since from (3.7) we have $M_0 = 4\pi\bar{\rho}/3$. Notice that the coefficients in (3.24) are functions of r so these equations are not entirely equivalent, however, for a given r the dynamics are identical. Therefore, both equations can be considered second-order linear differential equation having in general two linearly independent solutions corresponding to the growing and decaying mode of cosmological perturbation theory. In the case of (3.24), the coefficients of the growing and decaying modes are, in general, functions of r and as it turns out, these coefficients are fixed by the arbitrary functions $t_b(r)$ and $k(r)$. The growing mode is proportional to the gradient $k'(r)$, or $(E/M^{2/3})'$ for an arbitrary r coordinate, while the decaying mode is proportional to $t_b'(r)$ (See for example [160] for $\Lambda = 0$ models and §3 of [159] for $\Lambda > 0$ models.) The function $t_b(r)$ can then be thought of as the 'inhomogeneity' in the bang time while $k(r)$ can be thought of as the inhomogeneity in the spatial curvature. Both of these functions are of course constant in the FLRW limit so that growing and decaying modes vanish and we have $\Delta = 0$.

For collapsing models $E < 0$ the situation is different. The decaying mode depends on the derivative of the crunch time $t_c'(r)$, the time at which the shell becomes singular again.

Though E, M and t_b are arbitrary giving an infinite number of LTB models, certain types of models can be ruled out as unphysical. For example, models in which $t_b' \neq 0$ contain decaying modes implying that the universe was less homogeneous and isotropic at early times and thus incompatible with observations. Realistic LTB models then dictate $t_b' = 0$, or $t_b = \text{const}$, corresponding to a simultaneous big bang.

Cosmic voids and clusters

The existence of voids was predicted as early as 1934 in Tolman's original study of what are now known as LTB models. Tolman showed that the formation of voids is a consequence of the instability of inhomogeneities on a Friedmann background. For example, consider an idealised LTB model in which there is a small under- or overdensity at the centre isolated to a small region. Using (3.5) and (3.7) with the initial conditions $R(t_i, r) = a_i r$, $\dot{R}(t_i, r) = a_i H_i r$ and $\rho(t_i, r) = \bar{\rho}_i(1 + \delta(t_i, r))$ it can be shown that

$$\frac{\partial^2}{\partial t^2}\left(\ln\rho - \ln\bar{\rho}\right) = 4\pi(\rho - \bar{\rho}). \tag{3.26}$$

This equation shows that small perturbations away from $\bar{\rho}$ grow to be more pronounced over time. Underdense regions will become even emptier leading to the formation of voids. On the other hand, the growth of overdensities will continue unbounded until the breakdown of the model, e.g. when shell crossings occur (see below).

Since the evolution of the LTB model is governed by gravitating mass alone it is well suited to the study of structures on the scale of tens of megaparsecs, e.g., clusters and voids. On smaller scales the situation is complicated by hydrodynamical processes, when pressure and rotation, (which plays a crucial role in galaxy formation), become important. The flexibility in choosing density profiles that are not just limited to the linear regime make LTB models ideal candidates for describing voids within the framework of general relativity.

3.1.5 Shell crossing

It is possible that two nearby dust shells of different comoving radii will cross causing world lines of dust particles to intersect. Thus coordinates (r, θ, ϕ) no longer uniquely label worldlines. This causes the Kretschmann scalar, $R_{\mu\sigma\rho\lambda}R^{\mu\sigma\rho\lambda}$, and the density to diverge, leading to a singularity. Shell crossings signal a breakdown of the assumptions in LTB models, an artefact of an idealised dust model that a realistic model containing pressure can prevent. Shell crossings can be avoided by a judicious choice of the arbitrary functions.

Conditions to avoid shell crossing

Recall shells are uniquely labelled by the comoving coordinate r. As nearby shells collide, the proper distance between adjacent shells must then become zero implying that $R' = 0$ at shell crossings. However, this is not sufficient as the density, ρ, must also diverge. If $R' = 0$ but M'/R' (c.f. (3.7)) is finite, so that ρ is finite, then these surfaces are regular extrema.

If $R' > 0$ for all t, as is the case when $\rho > 0$, then we can be sure no shell crossings occur. Necessary and sufficient conditions for no shell crossings have been given for $\Lambda = 0$ models [161] and sufficient conditions have been given in the $\Lambda > 0$ case in [159]. There are three sets of conditions each for $E > 0$ (hyperbolic), $E < 0$ (elliptic), and $E = 0$ (parabolic). These conditions restrict the properties that $E(r)$, $M(r)$ and $t_B(r)$ can have but at the same time are sufficiently flexible that they can be easily satisfied.

3.2 The Szekeres solution

A broader class of inhomogeneous cosmologies can be found in the family of Szekeres solutions. These solutions are a generalisation of the LTB solutions (and by extension FLRW solutions) in which the requirement of spherical symmetry is relaxed, allowing anisotropic and inhomogeneous models to be studied in a GR setting. Naturally, there is a greater level of freedom that can be brought to bear on astrophysical cosmology but at the cost of added complexity. In this section we present the Szekeres solution and highlight the relevant details that will be needed in Chapter 4.

The energy-momentum tensor is that of dust, $T^{\mu\nu} = \rho\, u^\mu u^\nu$, but one can also include pressure (see the Szekeres-Szafron family of solutions [162]). The density, ρ, is in general a function of all spacetime coordinates.

We follow the original presentation of the solution due to Szekeres [94]. We begin with the general line element of the form

$$\mathrm{d}s^2 = -\,\mathrm{d}t^2 + \mathrm{e}^{2\alpha}\,\mathrm{d}r^2 + \mathrm{e}^{2\beta}(\mathrm{d}x^2 + \mathrm{d}y^2), \tag{3.27}$$

where α and β are functions of the synchronous-comoving coordinates t, r, x and y. We recall these coordinates can always be found for a dust source and worldlines are labelled not only by r, as in LTB solutions, but by x and y as well. While we label one of the spatial coordinates r, we emphasise that Szekeres solutions do not in general have an 'origin' as in the case of LTB solutions, so r should not be thought of as a radial coordinate.

With the metric of the above form and source specified, the field equations give

$$G^r{}_x = \mathrm{e}^{-2\alpha}(\beta_{,r}\alpha_{,x} - \beta_{,rx}) = 0, \tag{3.28a}$$

$$G^r{}_y = \mathrm{e}^{-2\alpha}(\beta_{,r}\alpha_{,y} - \beta_{,ry}) = 0, \tag{3.28b}$$

which implies

$$\beta_{,r} = u(t,r)\mathrm{e}^{\alpha}, \tag{3.29}$$

with $u(t,r)$ a first integral. The Szekeres solutions can be split into two classes according to whether $\beta_{,r} = 0$ or $\beta_{,r} \neq 0$ (or, equivalently $u(t,r) = 0$ or $u(t,r) \neq 0$). The $\beta_{,r} = 0$ case encompasses the homogeneous FLRW and Kantowski-Sachs solutions. Here we shall focus on the $\beta_{,r} \neq 0$ case as this has a far wider application to inhomogeneous cosmology.

We can safely assume $\beta_{,tx} = 0 = \beta_{,ty}$, as only then do solutions exist [94, 163]. Thus, β will be of the form

$$\beta(t,r,x,y) = \ln \Phi(t,r) + \nu(r,x,y), \tag{3.30}$$

or

$$\mathrm{e}^{\beta}(t,r,x,y) = \Phi(t,r)\mathrm{e}^{\nu(r,x,y)}. \tag{3.31}$$

The field equation, $G^t{}_r = 8\pi T^t{}_r$, gives

$$(\mathrm{e}^{\beta-\alpha}\beta_{,r})_{,t} = 0, \tag{3.32}$$

and together with (3.31) implies

$$\mathrm{e}^{\alpha} = \Phi(t,r)\beta_{,r}. \tag{3.33}$$

Using (3.31) and (3.33) the field equation, $G^r{}_r + \Lambda = 8\pi T^r{}_r$, reduces to

$$\mathrm{e}^{-2\nu}(\nu_{,xx} + \nu_{,yy}) + 1 = 2\Phi_{,tt}\Phi + \Phi_{,t}^2 - \Lambda\Phi^2. \tag{3.34}$$

Observing that the left-hand side depends on r, x and y while the right hand side depends only on t and r, by the separation of variables we conclude that both sides are equal to some function of r, i.e.,

$$2\Phi_{,tt}\Phi + \Phi_{,t}^2 - \Lambda\Phi^2 =: 2E(r). \tag{3.35}$$

In the same way as for the field equation (3.3b) of the LTB solution, we multiply the above equation by $\Phi_{,t}$ and integrate by t to obtain

$$\Phi_{,t}^2 = \frac{2M}{\Phi} + 2E + \frac{1}{3}\Lambda\Phi^2, \tag{3.36}$$

where $M(r)$ is another first integral. Notice this equation has exactly the same form as (3.5) for the LTB case. Likewise the initial condition of (3.36) furnishes another arbitrary function, $t_b(r)$, i.e., the bang time.

Returning to the left-hand side of (3.34), we have

$$\mathrm{e}^{-2\nu}(\nu_{,xx} + \nu_{,yy}) + 1 = 2E(r). \tag{3.37}$$

By using complex coordinates, it can be shown[1] that $\mathrm{e}^{-\nu}$ must have the general form

$$\mathrm{e}^{-\nu} = A(r)(x^2 + y^2) + 2B_1(r)x + 2B_2(r)y + C(r), \tag{3.38}$$

where $A(r)$, $B_1(r)$, $B_2(r)$ and $C(r)$ are arbitrary functions subject to the constraint

$$4(AC - B_1^2 - B_2^2) = 1 - 2E. \tag{3.39}$$

The density is obtained from the (tt) field equation:

$$8\pi\rho(t, r, x, y) = \frac{(2M\mathrm{e}^{3\nu})_{,r}}{\mathrm{e}^{2\beta}(\mathrm{e}^{\beta})_{,r}} = \frac{2(M_{,r} + 3M\nu_{,r})}{\Phi^2(\Phi_{,r} + \nu_{,r})}. \tag{3.40}$$

To summarise, the metric components are

$$g_{tt} = -1, \tag{3.41a}$$
$$g_{rr} = \Phi^2(t, r)\beta_{,r}^2, \tag{3.41b}$$
$$g_{xx} = g_{yy} = \Phi^2(t, r)/\mathrm{e}^{-2\nu(r,x,y)} = (\Phi_{,r} + \Phi\nu_{,r})^2, \tag{3.41c}$$

with ν given by (3.38) and Φ determined by the single dynamical equation (3.36). The Szekeres solution is then completely specified by the functions $E(r)$, $M(r)$, $t_b(r)$, $A(r)$, $B_1(r)$, $B_2(r)$, and $C(r)$. All told there are seven functions in the solution, of which six are independent on account of (3.39) but with a suitable coordinate transformation $r = f(r')$, only five need to be specified.

[1] See the appendix of [94] for a proof.

A more convenient formulation for the Szekeres solution was found by Hellaby [164]. The functions are redefined as follows:

$$\Phi = \sqrt{|\ell|}R, \qquad E = |\ell|\tilde{E}, \qquad M = |\ell|^{3/2}\tilde{M}, \qquad \epsilon = \ell/|\ell|, \tag{3.42}$$

$$A = \sqrt{|\ell|}/(2S), \qquad B_1 = -\sqrt{|\ell|}P/(2S), \qquad B_2 = -\sqrt{|\ell|}Q/(2S), \tag{3.43}$$

$$\text{where} \quad \ell(r) := 4(AC - B_1^2 - B_2^2) = 1 - 2E, \tag{3.44}$$

and imposing the constraint (3.39) we find

$$C = \frac{\sqrt{|\ell|}S}{2}\left[\frac{P^2+Q^2}{S^2} + \epsilon\right], \tag{3.45}$$

so that

$$\mathrm{e}^{-\nu} = \sqrt{|\ell|}\mathcal{E}, \tag{3.46}$$

$$\text{where} \qquad \mathcal{E} := \frac{S}{2}\left[\left(\frac{x-P}{S}\right)^2 + \left(\frac{y-Q}{S}\right)^2 + \epsilon\right]. \tag{3.47}$$

As a result, all functions are independent and the constraint (3.39) is identically satisfied. The line element takes the form

$$\mathrm{d}s^2 = -\,\mathrm{d}t^2 + \frac{(R' - R\mathcal{E}'/\mathcal{E})^2}{\epsilon + 2E}\,\mathrm{d}r^2 + \frac{R^2}{\mathcal{E}^2}(\mathrm{d}x^2 + \mathrm{d}y^2), \tag{3.48}$$

while the density becomes

$$8\pi\rho(t,r,x,y) = \frac{2(M' - 3M\mathcal{E}'/\mathcal{E})}{R^2(R' - \mathcal{E}'/\mathcal{E})}. \tag{3.49}$$

Note that the tildes above M and E have been dropped as from this point on we will no longer need to distinguish between the two formulations.

Comparing (3.48) and (3.49) with the LTB line element (3.8) and density (3.7) we immediately see that the term $\mathcal{E}'(r,x,y)/\mathcal{E}(r,x,y)$ represents the departure from spherical symmetry.

There are now six arbitrary functions $P(r)$, $Q(r)$, $S(r)$, $E(r)$, $M(r)$, $t_b(r)$ sharing five physical degrees of freedom with a coordinate freedom in r. Moreover $\epsilon = -1, 0, 1$ corresponding to *quasi-hyperbolic*, *quasi-plane* and *quasi-spherical* type models respectively.

As the names suggests, these models characterise the geometry of $t = \text{const}$ hypersurfaces, although within a given hypersurface the geometries of the $r = \text{const}$ 2-surfaces can change with r. Note the LTB solutions are recovered for the quasi-spherical case when P, Q and S are all constant.

For the remainder of this section we focus solely on the quasi-spherical $\epsilon = 1$ case. It is by far the most researched case [156, 163] and is capable of modelling a wide range of cosmological scenarios.

3.2.1 Mass dipole

In the quasi-spherical case the density distribution on each shell, consists of a monopole and dipole moment, i.e.,

$$\rho(t,r,x,y) = \rho_{\rm mono}(t,r) + \Delta\rho(t,r,x,y). \tag{3.50}$$

Shells labelled by different r will have different dipolar axes, which in general are not aligned with each other. Using (3.49) we decompose (3.49) as

$$8\pi\rho = \frac{2(M' - 3M\mathcal{E}'/\mathcal{E})}{R^2(R' - \mathcal{E}'/\mathcal{E})} + \frac{Z}{R^2} - \frac{Z}{R^2} \tag{3.51}$$

$$= \frac{Z}{R^2} + \frac{(2M' - ZR') - (6M - RZ)\mathcal{E}'/\mathcal{E}}{R^2(R' - R\mathcal{E}'/\mathcal{E})} \tag{3.52}$$

where we have introduced an arbitrary function $Z = Z(t,r)$. Note the first and second terms correspond to $\rho_{\rm mono}(t,r)$ and $\Delta\rho(t,r,x,y)$ respectively. The splitting is not unique as there are many ways in which $Z(t,r)$ can be defined, e.g., by demanding that $\Delta\rho = 0$ at $r = 0$ (see [156] for details).

3.2.2 The Szekeres solution in spherical coordinates

The quasi-spherical Szekeres solutions represent a family of t = const, r = const 2-dimensional spheres, or 'shells', with areal radius R, each with the line element $R^2\,\mathrm{d}\Omega^2$. In general these shells are displaced from each other according to the functions P, Q and S. In the LTB limit these shells are concentric. This can be understood by changing to spherical coordinates via the stereographic projection:

$$(x - P)/S = \cot(\theta/2)\cos\phi, \qquad (y - Q)/S = \cot(\theta/2)\sin\phi. \tag{3.53}$$

This is a mapping of the infinite (x,y) plane onto the 2-sphere described by the finite range of coordinates θ and ϕ. Through these equations the role of P, Q and S becomes clear. The function P and Q represent r-dependent displacements of the 2-spheres, while the function S gives the magnification of the 2-sphere when mapped onto the (x,y) plane. In these coordinates we have

$$\mathcal{E} = S/(1 - \cos\theta). \tag{3.54}$$

The line element is non-diagonal in these coordinates:

$$\begin{aligned}\mathrm{d}s^2 = &-\mathrm{d}t^2 + \frac{1}{1+2E}\left[R' + \frac{R}{S}(S'\cos\theta + N\sin\theta)\right]^2\mathrm{d}r^2 \\ &+ R^2\left[\frac{S'\sin\theta + N(1-\cos\theta)}{S}\right]^2\mathrm{d}r^2 + R^2\left[\frac{N_{,\phi}(1-\cos\theta)}{S}\right]^2\mathrm{d}r^2 \\ &- R^2\frac{2[S'\sin\theta + N(1-\cos\theta)]}{S}\,\mathrm{d}r\,\mathrm{d}\theta + R^2\frac{2N_{,\phi}\sin\theta(1-\cos\theta)}{S}\,\mathrm{d}r\,\mathrm{d}\theta \\ &+ R^2\,\mathrm{d}\Omega^2,\end{aligned} \tag{3.55}$$

where $N(r,\phi) = P'\cos\phi + Q'\sin\phi$ and primes again denote r partial derivatives.

3.3 Other exact models

3.3.1 The Swiss cheese model

Obtaining a solution of the field equations that describes the Universe on more than one scale is a difficult problem. However, a solution of the field equations can be constructed out of other known solutions. Such constructions with different regions described by different metrics are known as Swiss cheese models.

The Einstein-Straus Swiss cheese [165] is one such example obtained by embedding a Schwarzschild solution in a Friedmann background and was originally intended to describe the local effects of stars within a cosmological setting. More sophisticated models have since been studied. For example one can describe a lattice of holes by LTB solutions in which the density profile can be tuned to model different types of cosmological structures (including $\ll 100h^{-1}$ Mpc sized structures). When used as cosmological models, (i.e., with a FLRW background) the boundary of the hole forms a comoving surface, subject to the Darmois-Israel junction conditions [166, 167].[2]

These types of models add another layer of depth to modelling the universe with a FLRW metric in that they are able introduce nonlinear inhomogeneities. However, in these models the holes maintain the same (comoving) distance with the boundary. As a result the evolution of the holes do not influence the evolution of the background in which they are embedded, so that these models are not useful in studying the effects of inhomogeneities on the average evolution of the universe, i.e., backreaction does not arise.

3.4 Light propagation

3.4.1 Radial null geodesics in LTB models

In the case of the LTB model there is an alternative way to determine the geodesics. For the special case that the observer receives the photon along a radial trajectory the problem becomes 1-dimensional and we can evaluate the redshift without having to first solve the null geodesic equations. We summarise below a method due to Bondi [44] for computing the redshift.

We consider an infalling photon which is emitted from a source at $r = r_{\rm em}$ and received by an observer at $r = r_o$. Both source and observer are taken to be comoving. As the geodesic does not cross the centre, we may use the radial coordinate to parametrise the

[2]The technical construction, amounting to matching at the hole boundary the first and second fundamental forms, g_{ij} and K_{ij} respectively, is known as the Darmois-Israel junction conditions. The requirement that the two regions share a symmetry (e.g. spherical symmetry) at the boundary is not essential but does simplify the construction. For example, Szekeres Swiss cheese models are possible and have no symmetry at the boundary.

trajectory $t = t(r)$. Using the null condition $k^\mu k_\mu = 0$ we obtain the equation

$$\frac{\mathrm{d}t}{\mathrm{d}r} = -\frac{R'}{\sqrt{1+2E}}, \tag{3.56}$$

where we take the negative root since the photon is infalling and $R' > 0$ for $\rho > 0$. Assuming that the period τ of the photon remains small over the time of flight, then the evolution of the period τ for two identical photons emitted $\tau(r)$ apart is to first order

$$\begin{aligned}\frac{\mathrm{d}\tau(r)}{\mathrm{d}r} &= \frac{\mathrm{d}\left(t(r)+\tau(r)\right)}{\mathrm{d}r} - \frac{\mathrm{d}t}{\mathrm{d}r} \\ &\approx -\frac{\dot{R}'(t(r),r)}{\sqrt{1+2E}}\tau(r)\end{aligned}$$

where we have used (3.56). Solving the above gives the redshift measured by an observer at $t = t(r_o)$ and emitted at $t = t(r_{\mathrm{em}})$:

$$\begin{aligned}1 + z \equiv \frac{\lambda_o}{\lambda_{\mathrm{em}}} &= \frac{\nu_{\mathrm{em}}}{\nu_o} = \frac{\tau(r_o)}{\tau(r_{\mathrm{em}})} \\ &= \exp\left(\int_{r_{\mathrm{em}}}^{r_o} \frac{\dot{R}'(t(r),r)}{\sqrt{1+2E(r)}}\,\mathrm{d}r\right).\end{aligned}$$

3.4.2 Non-radial null geodesics in LTB model

In this section we consider an off-centre observer located at point p with coordinates (t_p, r_p) and derive the null geodesics $x^\mu(\lambda)$ that pass through this point. The photon trajectory is completely determined by this position and the angle α between the photon direction and the direction away from the centre of the model. Note given any affine parameter λ we can set $k^t|_p = 1$ by making an affine transformation $\lambda \mapsto a\lambda + b$ and choosing an appropriate a. In addition we choose b such that λ is monotonically decreasing to $\lambda = 0$ at the observation point p.

One can then integrate back up the geodesic to the source position with the initial conditions $k^t|_p = 1$, $t = t_p$, and $r = r_p$. By spherical symmetry, one can think of the photon as moving within a plane defined by, say $\theta = \pi/2$, so that $k^\theta = 0$. We note that $k^\mu k_\mu = 0$ gives the constraint

$$(k^t)^2 = \frac{R'^2}{1+2E}(k^r)^2 + R^2(k^\phi)^2. \tag{3.57}$$

The null geodesic equation of ϕ,

$$\frac{\mathrm{d}k^\phi}{\mathrm{d}\lambda} + \frac{2}{R}\frac{\mathrm{d}R}{\mathrm{d}\lambda}\,k^\phi = 0, \tag{3.58}$$

can be integrated by multiplying both sides by R^2 to get

$$k^\phi = \frac{J}{R^2}, \tag{3.59}$$

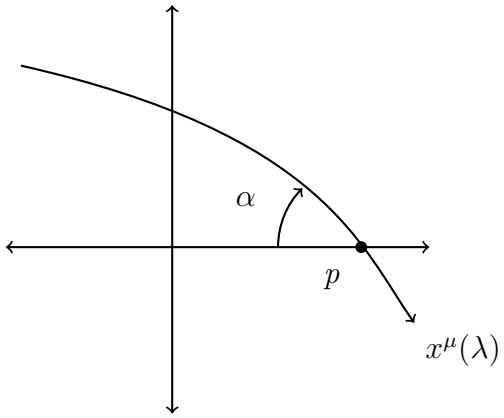

Figure 3.1: Angle α subtended by the direction of observation and the line joining the origin to the observer.

which means that $k_\phi = J$ is constant on geodesics. Here J represents the angular momentum of the particle. Since $k^t|_p = 1$, $k^r|_p = A\cos\alpha$ and $k^\phi|_p = B\sin\alpha$ and the above constraint must hold for all angles, by taking (3.57) at (t_p, r_p) with angles $\alpha = 0$ and $\alpha = \pi/2$ we find

$$A = \frac{(1+2E(r_p))^{1/2}}{R'(t_p,r_p)} \qquad \text{and} \qquad B = R^{-1}(t_p,r_p), \tag{3.60}$$

respectively. We then have $k_\phi = g_{\phi\phi}k^\phi|_p = R(t_p,r_p)\sin\alpha$ is constant. The remaining geodesic equations then reduce to two equations in two unknowns t and r, or, equivalently, as three first order equations in t, r and k^t:

$$\frac{\mathrm{d}t}{\mathrm{d}\lambda} = k^t, \tag{3.61a}$$

$$\frac{\mathrm{d}r}{\mathrm{d}\lambda} = \pm\frac{(1+2E)^{1/2}}{R'}\left[(k^t)^2 - \frac{J^2}{R^2}\right]^{1/2}, \tag{3.61b}$$

$$\frac{\mathrm{d}k^t}{\mathrm{d}\lambda} = \frac{J^2}{R^2}\left(\frac{\dot{R}'}{R'} - \frac{\dot{R}}{R}\right) - \frac{\dot{R}'}{R'}(k^t)^2, \tag{3.61c}$$

where $R_p \equiv R(t_p, r_p)$. The plus (minus) sign is taken for an outgoing (ingoing) photon, i.e., an observer looking inward (outward).

By spherical symmetry one can always treat a photon as propagating on the plane, i.e., as a 2-dimensional problem. However, in Chapter 4 when we ray trace over the whole sky all 4 null geodesic equations need to be solved. The complete equations can be found in Appendix A.

Finally we note that the redshift for a comoving source and observer, with respective 4-velocities $u^\mu_{\mathrm{em}} = \delta^\mu{}_t$ and $u^\mu_0 = \delta^\mu{}_t$, and measured energies $E_{\mathrm{em}} = -u^\mu_{\mathrm{em}}k_\mu$ and $E_0 = -u^\mu_0 k_\mu$, is given by

$$1 + z = \frac{g_{\mu\nu}u^\mu_{\mathrm{em}}k^\nu}{g_{\mu\nu}u^\mu_0 k^\nu|_p} = k^t, \tag{3.62}$$

where $g_{\mu\nu}u^\mu_0 k^\nu|_p = 1$ with the above choice of affine parameter.

Chapter 4

Method and Results

Using the techniques described in chapter 3, we investigate two models, namely the LTB and Szekeres models. These models will be used to describe a nonlinear void, and an additional overdensity in the Szekeres case. We will use them to generate CMB maps by solving the null geodesic equations. Of particular interest is how observers located in and around the void will affect the observed CMB dipole and quadrupole.

In this chapter we also investigate the prospect that the CMB dipole has a non-kinematic origin. It has been known for some time that LTB observers displaced from the centre of spherical symmetry can induce a significant dipole, just like Lorentz boost. While the size of the dipole can be matched by tuning the void, what is not clear is whether the void can also give rise to modulation and aberration-like effects, associated with a Lorentz boost. With the recent detection of such effects by *Planck* [108] it is an important test of the non-kinematic hypothesis.

4.1 Setting up the model

The model can be set up in many ways as we have discussed in previous sections. Here we follow the procedure given by Bolejko [168]. The steps are as follows.

The mass function is of the form

$$M(r) = M_0(r) + \delta M(r), \tag{4.1}$$

where

$$M_0(r) = \frac{4}{3}\pi\overline{\rho}(t_0)r^3 = \frac{1}{2}\Omega_m H_0^2 r^3, \tag{4.2}$$

is the homogeneous FLRW mass profile, while $\delta M(r)$ gives the deviation away from homogeneity. The arbitrary function δM will be chosen so that the mass function asymptotically approaches zero in the limit that r goes to infinity, i.e., $M(r) \to M_0(r)$ as $r \to \infty$. As was discussed in §3.2, a given worldline of a Szekeres spacetime is labelled by its spatial coordinates and can be identified with a congruence of worldlines of some FLRW

model. In this sense, the Szekeres model is said to be asymptotically FLRW. In terms of the background parameters we have

$$M(r) = \frac{1}{2}\Omega_m H_0^2 r^3 \left(1+\delta\right), \tag{4.3}$$

where we have introduced $\delta = \delta(r)$, which fully entails the deviation from homogeneity. As in [1] this function is chosen to be

$$\delta(r) = \frac{1}{2}\delta_0 \left(1 - \tanh\frac{r-r_0}{2\Delta r}\right), \tag{4.4}$$

where $\delta_0 \in [-1,0]$, r_0 and Δr are constants; r_0 gives the characteristic size of the void, while Δr determines the steepness of the profile (see fig. 4.3). We emphasise that δ_0 is *not* the central density contrast and the function $\delta(r)$ is *not* the conventional density contrast. The density contrast is defined as $\Delta \equiv (\rho - \overline{\rho})/\overline{\rho}$, with the density ρ determined from (3.49) and will depend on all coordinates, not just r.

The coordinate gauge is fixed such that the radial coordinate coincides with the areal radius at the present time, i.e., $R(t_0, r) = r$ where t_0 is the age of the universe.

We shall take $R(t,r)$, $P(r)$, $Q(r)$, $S(r)$, t and r to have units Mpc.

Requiring that the universe evolved from a more homogeneous initial state, we take $t_b(r) = \text{const}$. As discussed in §3.1.4, since $t_b' = 0$ the model contains no decaying mode so that the void profile is shallower into the past and deeper into the future with the overdense shell becoming denser still (see fig. 4.3). It remains to find $E(r)$, which with this choice of gauge, is obtained by solving (3.6) at $t = t_0$, i.e., by solving the integral equation

$$t_0 = \int_0^r \left(\frac{2M(r)}{a} + 2E(r) + \frac{1}{3}\Lambda a^2\right)^{-1/2} \mathrm{d}a. \tag{4.5}$$

The curvature function $k(r) \equiv -2E(r)$ is shown in fig. 4.1. Also shown is the Hubble parameter normalised w.r.t. the FLRW background. As can be seen the local Hubble parameter for an observer in the void at the present epoch can be as much as $\approx$20% higher than the background.

The Szekeres model we study will be defined by (4.3) and the following functions:

$$P(r) = 0, \qquad Q(r) = 0, \qquad S(r) = (r/1\,\mathrm{Mpc})^{\alpha}\,\mathrm{Mpc}. \tag{4.6}$$

The anisotropic aspect of this model is then parametrised by α and represents a one-parameter family of Szekeres solutions. When $\alpha \to 0$ we recover the LTB limit in which the density is uniform on each shell. The function S represents a displacement of these shells in the direction $(\theta, \phi) = (\pi, 0)$, with a larger α corresponding to a greater concentration of matter on one end of the shell than on the other, resulting in a density dipole. As was mentioned in §3.2, each shell's matter dipole are generally not aligned, however, the functions P and Q being zero means these shells will share a common dipolar axis, as

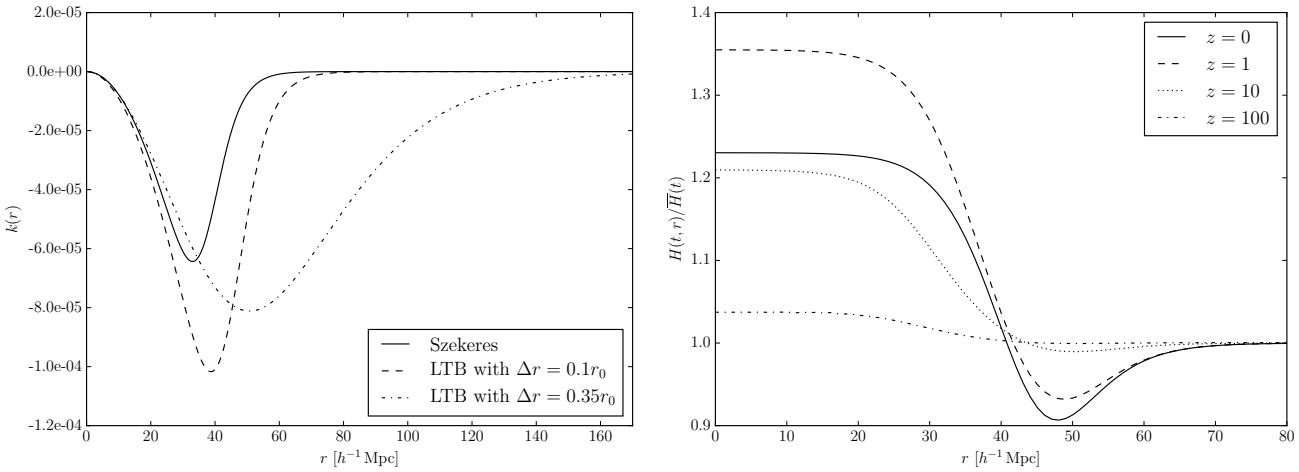

Figure 4.1: *Left:* The function $k(r) = -2E(r)$ in geometric units. *Right:* Evolution of the LTB Hubble expansion profile normalised to the background Hubble parameter $\overline{H}(t)$.

can be seen in fig. 4.2. Thus, while this particular Szekeres model is less symmetric than the LTB model, it is however axially symmetric possessing the Killing vector ∂_ϕ. This is clear since the quantity $\mathcal{E}'/\mathcal{E} = -\sin\theta S'(r)/S(r)$ does not depend on ϕ and therefore $\rho = \rho(t, r, \theta)$, i.e., matter is distributed symmetrically about the axis of the dipole. Although the density contrast Δ depends on R and R', and therefore requires numerical computation, we can, however, write down its form at the present epoch t_0, since with the above gauge choice $R(t_0, r) = r$ and $R'(t_0, r) = 1$. With the choice of functions (4.4) and (4.6) we find

$$\Delta(t_0, r, \theta) = \Delta_{\text{mono}}(t_0, r) - \frac{1}{3}\frac{\alpha \sin\theta}{(1 + \alpha \sin\theta)}\, r\delta'(r), \tag{4.7}$$

where

$$\Delta_{\text{mono}}(t_0, r) = \delta(r) + \frac{1}{3} r\delta'(r), \tag{4.8}$$

is the density contrast monopole. The LTB limit is then recovered by setting $\alpha = 0$, upon which we find $\Delta = \Delta_{\text{mono}}(r)$.

The Szekeres model is chosen to asymptotically approach the spatially flat FLRW model specified by the *Planck* 2013 Legacy archive parameters,

$$\{\Omega_m,\, \Omega_\Lambda, \Omega_k,\ h\} = \{0.315,\, 0.685,\, 0,\, 0.673\}, \tag{4.9}$$

where Ω_m, Ω_Λ and Ω_k are the matter, cosmological constant and spatial curvature density parameters respectively, and h is related to the Hubble parameter by $H_0 = 100\, h\, \mathrm{km\, s^{-1}\, Mpc^{-1}}$. Note since $\Omega_k = 0$, the Friedmann equation (2.5) can be solved analytically giving the formula for the age of the universe

$$t_0 = \frac{1}{3\sqrt{\Omega_\Lambda} H_0} \ln\left(\frac{1 + \sqrt{\Omega_\Lambda}}{1 - \sqrt{\Omega_\Lambda}}\right). \tag{4.10}$$

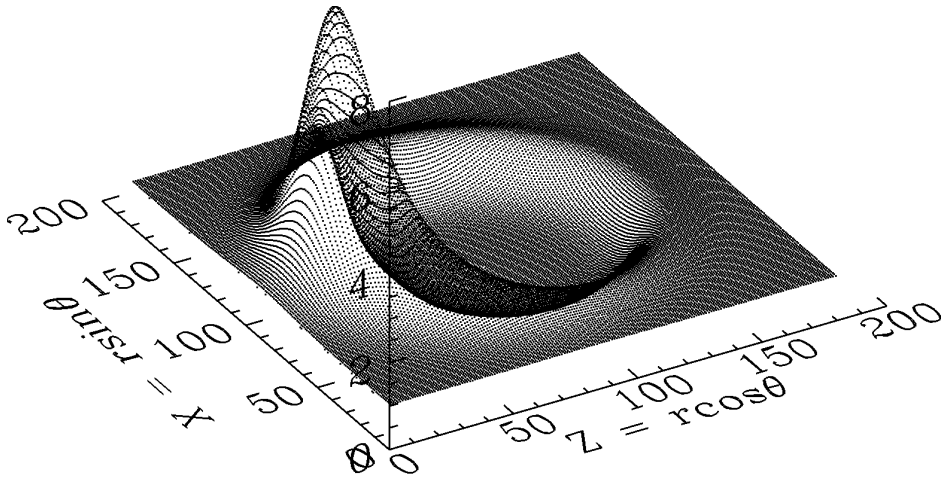

Figure 4.2: The density of the Szekeres model normalised to the background density. Note we define the coordinates $X := R(t_0, r)\cos\theta = r\cos\theta$ and $Z := R(t_0, r)\sin\theta = r\sin\theta$.

Following [1] the Szekeres model is specified by

$$r_0 = 38.5\,h^{-1}\,\mathrm{Mpc}, \qquad \delta_0 = -0.86 \qquad \text{and} \qquad \alpha = 0.86 \tag{4.11}$$

while the LTB model is specified by

$$r_0 = 45.5\,h^{-1}\,\mathrm{Mpc}, \qquad \delta_0 = -0.95 \qquad \text{and} \qquad \alpha = 0. \tag{4.12}$$

In both models we take $\Delta r = 0.1 r_0$. These parameters were found through a 5-dimensional parameter space search with the requirements that the resultant model is consistent with the CMB dipole and quadrupole, as well as the dipole and quadrupole[1] of the Hubble expansion anisotropy [1]. The choice of Δr was made in order to reduce the size of parameter space, and as can be seen in fig. 4.3, it gives a somewhat steep transition to homogeneity. Thus, the situation we are interested in studying is inhomogeneous on scales $\lesssim 100\,h^{-1}\,\mathrm{Mpc}$.

4.2 Methodology

4.2.1 Ray tracing

Now that we have specified the model, we turn to the task of simulating the CMB sky as seen by a hypothetical observer located within the void.

To do this we ray trace through the above models by solving the null geodesic equations in spherical coordinates. The reason is that the observer's angular coordinates (on the sky) are most naturally related to these coordinates. In the LTB model the geodesic equations are given by (3.61a)–(3.61c). The geodesic equations in the Szekeres case are not as simple, due to the more complicated Szekeres metric (even more so in spherical

[1]The magnitude of the dipoles match, but as yet the simulated quadrupoles are smaller.

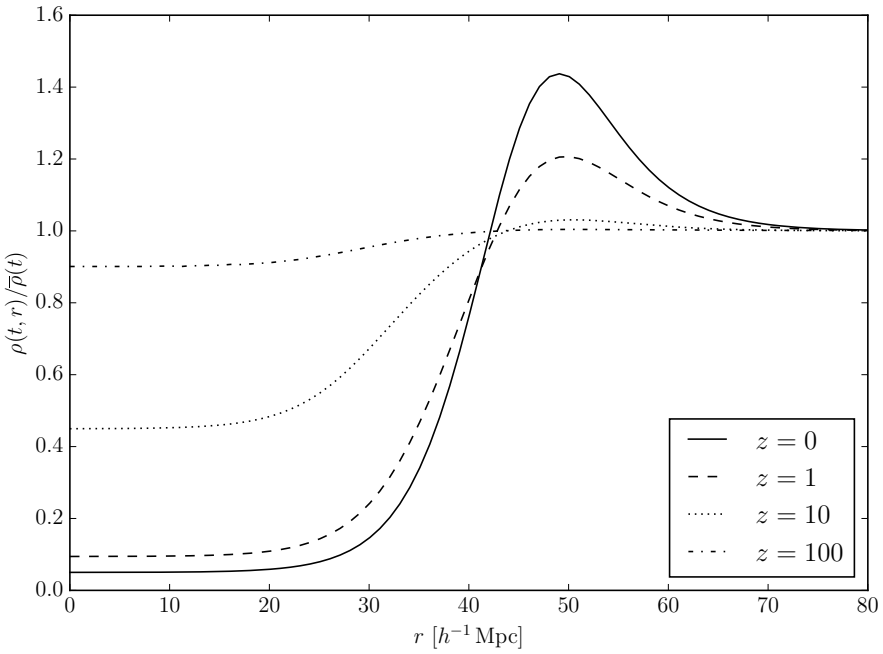

Figure 4.3: The evolution of the density profile of the LTB model normalised to the background FLRW model.

coordinates). These can, however, be found in the appendix of [169] (and we confirm that these are indeed correct using Maple). The redshift z is determined from (3.62). The ray tracing code we use is based on a numerical code by Krzysztof Bolejko, which was used to obtain the results in [1]. We modify and optimise the code to allow for fast computation of redshift and the inversion of the integral equation (4.5). In particular we solve the null geodesic equations using the Dormand-Prince 8th-order Runge-Kutta method.

We use the HEALPix[2] (Hierarchical Equal Area isoLatitude Pixelisation) scheme to partition the sky into equal sized areas or pixels. The ith pixel is assigned a ray with angular coordinates (l_i, b_i), which, together with $t = t_0$ and $r = r_{\rm obs}$, fixes the initial position of the null geodesic equations to be solved.

The number of pixels is determined by $N_{\rm pix} = 12N_{\rm side}^2$, where $N_{\rm side}$ (the number of 'sides') is a convenient way to parameterise the resolution of the map, and corresponds to the number of isolatitude bands that encircle the sphere.

Ray tracing over the whole sky is a computationally intensive task, even if one is just sampling the sky to a resolution of a few degrees. In this work we choose $N_{\rm side} = 16$. This is more than sufficient given that we are primarily interested in the dipole and quadrupole induced by these models. This corresponds to 3072 pixels each covering an area of $\Delta\Omega = 4\pi/N_{\rm pix} \approx 1.6 \times 10^{-5}\,{\rm sr}$ of the sky. Each pixel determines the initial conditions of the null geodesic propagated in the pixel's direction on the sky (see below). As a rule of thumb the power spectrum should only be computed up to $\ell_{\rm max} \leq N_{\rm side}/2$

[2]For more information go to `http://healpix.sourceforge.net`.

in order to avoid sampling below the resolution of the pixel sky.

Initial conditions

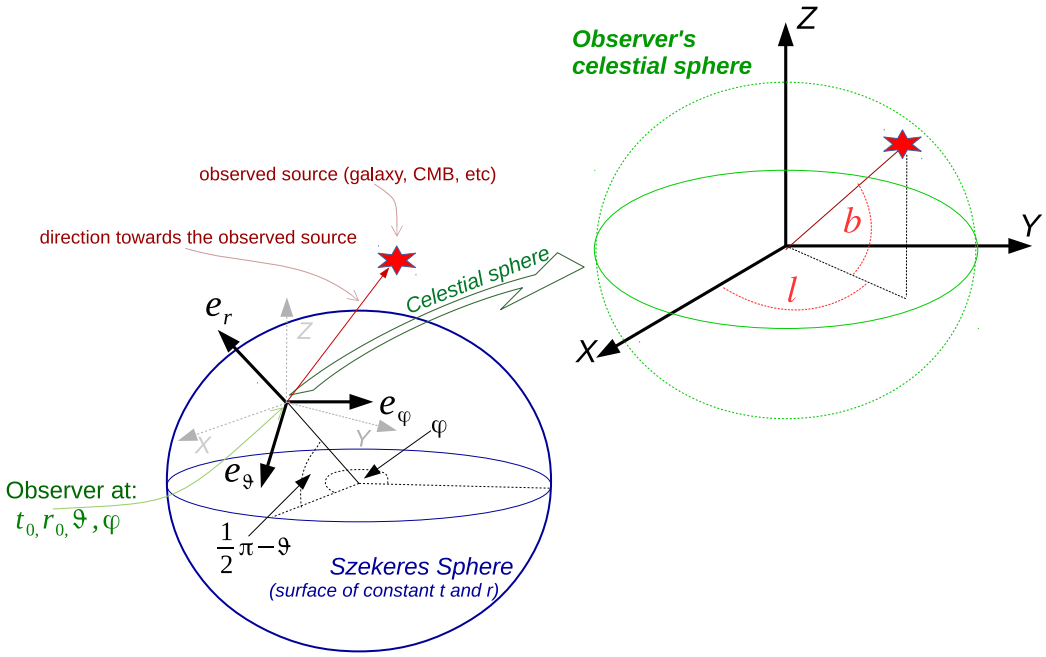

Figure 4.4: Observer's celestial sky in relation to the Szekeres spherical coordinates. (Credit: Bolejko [170])

Here we outline how to obtain the initial conditions for the null geodesics. As we adopt the HEALPix scheme, we describe an algorithm to convert each pixel to its corresponding initial null vector.

Recall the null geodesic equations are a set of 4 second-order ODEs or, equivalently, 8 first-order ODEs. Thus, one needs a total of 8 initial conditions: 4 for the initial position x^μ and 4 for the initial direction of propagation $k^\mu = \frac{\mathrm{d}x^\mu}{\mathrm{d}\lambda}$. Since we solve the geodesic equations backwards in time the initial position is taken to be at the observer's location:

$$(t_i,\, r_i,\, \theta_i,\, \phi_i) = (t_0,\, r_o,\, \vartheta,\, \varphi), \tag{4.13}$$

where, because of axial symmetry of the Szekeres model, φ can be set to any value. (In the LTB model this is true for ϑ as well.) The remaining initial conditions k^μ are required to be consistent with the HEALPix convention, i.e., we want the geodesics to emanate from the observer in a uniform manner. The procedure to obtain them from the pixel coordinates l, b are involved and is the subject of the rest of this section.

First let us decompose the null vector w.r.t. a timelike vector $u^\mu = \delta^\mu{}_t$ and a spacelike vector n^μ:

$$k^\mu = k^t(u^\mu + n^\mu), \qquad n^\mu = (0,\, n^i), \tag{4.14}$$

with $u^\mu u_\mu = -1$, $n^\mu n_\mu = 1$ and $u^\mu n_\mu = 0$. (Recall $g_{\mu\nu}k^\mu u^\nu = k^t$.) At the point of reception we can always set $k^t = 1$ by a suitable choice of affine parameter (see §3.4.2).

This leaves 3 initial conditions to be specified. In fact, only 2 of these are physical since at the point of reception $k^i = n^i$ is just the direction the photon is observed, and this is related to the observer's coordinates l, b (see fig. 4.4). We therefore ray trace only in those directions specified by the HEALPix pixels.

During the course of this investigation it was discovered that the algorithm by Bolejko for the initial conditions in the numerical code contained an error that did not take into account the fact that (3.55), the Szekeres metric in spherical coordinates, is non-diagonal. In the following we outline a corrected algorithm by Bolejko [170]. It takes as input the galactic coordinates l, b and outputs to the initial null vector k^μ.

For each pixel $p \in \{1, 2, \ldots, 12N_{\rm side}^2\}$, corresponding to the direction $\hat{\boldsymbol{n}}$ or angular coordinates (l, b) (this will be the direction the photon is observed)

(i) Compute the vector $\hat{\boldsymbol{n}}$ in Cartesian coordinates of a local spatial frame corresponding to standard galactic latitude and longitude

$$\hat{n}^x = \sin b \cos l, \quad \hat{n}^y = \sin b \sin l, \quad \hat{n}^z = \cos l. \tag{4.15}$$

In the local orthonormal frame the null vector is $k^{\hat{a}} = (-1, \hat{\boldsymbol{n}})$ and we have implicitly chosen the affine parameter so that the rays travels backwards in time.

(ii) Compute the local orthonormal tetrad basis $\{\boldsymbol{e}_{\hat{a}}\}$ (see Appendix B for details).

(iii) Transform back to Szekeres spherical coordinates: $k^\mu = k^{\hat{a}} e_{\hat{a}}{}^\mu$.

4.2.2 The CMB anisotropy from null geodesics

We recall that the temperature, $T_{\rm em}$ of the CMB at emission (which we assume to be at the time of last scattering) is related to the temperature of the observed CMB by $T = T_{\rm em}/(1+z)$ or

$$(1+z) = \frac{T_{\rm em}}{T} \tag{4.16}$$

where $T = T(\hat{\boldsymbol{n}})$ is the observed temperature in the direction $\hat{\boldsymbol{n}}$, and thus z is also directionally dependent. The redshift can be computed directly from the model using (3.62), that is, by solving the null geodesic equations.

To calculate the raw temperature we must input by hand either the temperature at reception or emission. The dimensionless anisotropy, however, can be determined in terms of redshift alone by observing

$$\begin{aligned} \frac{\Delta T}{T} \equiv \frac{T(\hat{\boldsymbol{n}}) - \langle T \rangle_\Omega}{\langle T \rangle_\Omega} &= \frac{T(\hat{\boldsymbol{n}})/T_{\rm em} - \langle T \rangle_\Omega / T_{\rm em}}{\langle T \rangle_\Omega / T_{\rm em}} \\ &= \frac{(1+z)^{-1} - \left\langle (1+z)^{-1} \right\rangle_\Omega}{\left\langle (1+z)^{-1} \right\rangle_\Omega} \end{aligned} \tag{4.17}$$

where angle brackets with subscript Ω denotes the spherical average

$$\langle T\rangle_\Omega = \frac{1}{4\pi}\int T(\hat{\boldsymbol{n}})\ \mathrm{d}\hat{\boldsymbol{n}} = \frac{1}{4\pi}\int_0^{2\pi}\mathrm{d}\phi\int_0^{\pi}\mathrm{d}\theta\ \sin\theta\, T(\theta,\phi). \tag{4.18}$$

Here and in the following θ and ϕ are angular coordinates on the observer's celestial sphere *not* the coordinates of the LTB or Szekeres models. It should however be clear from the context which are being used. We have assumed the photon is emitted at the time of last scattering and also $T_{\rm em} = T_{\rm lss} =$ constant so that $\langle T_{\rm em}\rangle_\Omega = T_{\rm em}$. For an inhomogeneous spacetime the intersection of the observer's past light cone with the last scattering surface cannot be said to form a sphere, so the quantity $\langle T_{\rm em}\rangle_\Omega$ is not well defined. However, since the age of the universe is the same everywhere for the dust cosmologies we consider, we can take the last scattering surface to be a $t =$ constant hypersurface with the temperature of the universe assumed to be very uniform.

In principle, the redshift is computed by integrating the geodesics all the way back to the surface of last scattering. However, in practice the size of our voids are much smaller than the Hubble radius. It therefore suffices to propagate the geodesics to $r \gtrsim 200h^{-1}\,\mathrm{Mpc}$ for observers located within $r = 70h^{-1}\,\mathrm{Mpc}$. Beyond this distance, the local geometry is essentially that of a FLRW cosmology, and the redshift anisotropy that rays pick up is negligible.

All rays are propagated backwards in time, starting from the point of observation (4.13), and ending when the elapsed time reaches $400\,\mathrm{Mpc}/c$. This ensures the rays are well clear of the void and into the homogeneous outer regions.

We decompose $\Delta T/T$ into spherical harmonics:

$$\Theta(\theta,\phi) \equiv \frac{\Delta T(\theta,\phi)}{T} = \sum_{\ell=0}^{\infty}\sum_{m=-\ell}^{\ell} a_{\ell m}\, Y_{\ell m}(\theta,\phi). \tag{4.19}$$

By the properties of spherical harmonic functions the coefficients $a_{\ell m}$ are given by

$$a_{\ell m} = \int_0^{2\pi}\mathrm{d}\phi\int_0^{\pi}\mathrm{d}\theta\,\sin\theta\,\Theta(\theta,\phi)Y^*_{\ell m}(\theta,\phi). \tag{4.20}$$

In practice, numerically the integral becomes a sum, and following the HEALPix scheme, the sum is over $N_{\rm pix}$ points. The coefficients are computed as follows:

$$\begin{aligned} a_{\ell m} &\approx \sum_{i=1}^{N_{\rm pix}} \Theta(\theta_i,\phi_i)\, Y^*_{\ell m}(\theta_i,\phi_i)\ \sin\theta_i\,\Delta\theta_i\,\Delta\phi_i \\ &= \frac{4}{N_{\rm pix}}\sum_{i=1}^{N_{\rm pix}} \Theta(\hat{\boldsymbol{n}}_i)\, Y^*_{\ell m}(\hat{\boldsymbol{n}}_i) \end{aligned} \tag{4.21}$$

where $\hat{\boldsymbol{n}}_i = \hat{\boldsymbol{n}}(\theta_i,\phi_i)$. Note for a given $N_{\rm side}$, $\Delta\theta = \Delta\theta_i$ is constant since the sides are isolatitude by construction. The power of HEALPix is in its ability to identify each

pixel by a single, unique index $i \in \{1, \ldots, 12N_{\rm side}^2\}$, thereby allowing fast and efficient evaluation of the $a_{\ell m}$, from an input map.

As discussed in §2.3 an observer only has access to their sky, and only their sky, so estimates

$$\tilde{C}_\ell = \frac{1}{2\ell+1}\sum_m |a_{\ell m}|^2. \tag{4.22}$$

By convention, what is of actual interest when analysing CMB data is not[3] C_ℓ but instead

$$\mathcal{D}_\ell \equiv \frac{\ell(\ell+1)\tilde{C}_\ell}{2\pi}\,\langle T\rangle_\Omega^2\,, \tag{4.23}$$

where we have multiplied by $\langle T\rangle_\Omega^2$, since the power spectrum is associated with $\Theta \equiv \Delta T/\langle T\rangle_\Omega$ *not* ΔT (for which we would have $\mathcal{D}_\ell = \ell(\ell+1)\tilde{C}_\ell/(2\pi)$ as is often seen in the literature). Note $\mathcal{D}_\ell$ has units of temperature squared.

4.2.3 A framework for the computation of the dipole

The presence of a foreground inhomogeneity on the CMB induces large-angle fluctuations, most notably the dipole, and to a lesser extent, the quadrupole. The effect on $\ell \geq 3$ multipoles is on the order $\Delta T/T \lesssim 10^{-9}$, far below the size of primordial fluctuations ($\Delta T/T \sim 10^{-5}$). In this section we focus on the theory of the dipole, and derive general tools used in the computation of the dipole.

For a function $T(\theta,\phi) = \sum_{\ell m} a_{\ell m} Y_{\ell m}(\theta,\phi)$ the dipole is the part $\sum_{m=-1}^{1} a_{1m} Y_{1m}(\theta,\phi)$. Expanding this out we find

$$\begin{aligned}
\sum_{m=-1}^{1} a_{1m}Y_{1m}(\theta,\phi) &= a_{1-1}\sqrt{\frac{3}{8\pi}}\mathrm{e}^{-i\phi}\sin\theta + a_{10}\sqrt{\frac{3}{8\pi}}\cos\theta - a_{11}\sqrt{\frac{3}{8\pi}}\mathrm{e}^{i\phi}\sin\theta \\
&= \sqrt{\frac{3}{8\pi}}\Big[(a_{1-1}+a_{1-1}^*)\sin\theta\cos\phi - i(a_{11}-a_{11}^*)\sin\theta\sin\phi + \sqrt{2}\,a_{10}\cos\theta\Big] \\
&= \sqrt{\frac{3}{8\pi}}(-2a_{11}^{re}\sin\theta\cos\phi + 2a_{11}^{im}\sin\theta\sin\phi + \sqrt{2}a_{10}\cos\theta) \qquad (4.24a) \\
&\equiv \boldsymbol{d}\cdot\hat{\boldsymbol{n}} \qquad (4.24b)
\end{aligned}$$

where

$$\hat{\boldsymbol{n}} = (\hat{n}_x, \hat{n}_y, \hat{n}_z) = (\sin\theta\cos\phi,\, \sin\theta\sin\phi,\, \cos\theta), \tag{4.25}$$

is a direction on the observers celestial sphere, a_{11}^{re} and a_{11}^{im} denote the real and imaginary parts of a_{11} and we have used $a_{\ell m}^* = (-1)^m a_{\ell -m}$ on the first line and $a_{1-1}^{re} = -a_{11}^{re}$ on the second. The formulae for the spherical harmonics can be found in Appendix D. The

[3]The reason for this is because for a scale-invariant power spectrum characterised by the spectral index $n_s = 1$, the angular power spectrum has the form $C_\ell \sim \frac{2\pi}{\ell(\ell+1)}$. Note observational data from *Planck* and *WMAP* indicate an index close to 1.

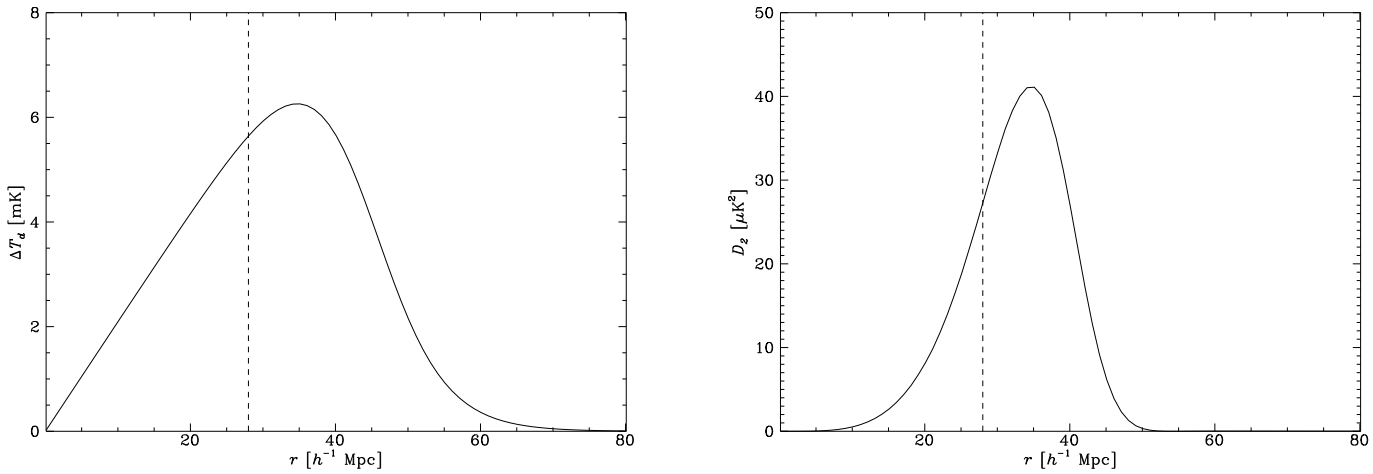

Figure 4.5: Profiles of the dipole and quadrupole of the LTB model. The position of an LTB observer at a coordinate distance of $r_o = 28h^{-1}$ Mpc from the centre, as found in [1], is indicated by the vertical dashed line.

dipole vector $\boldsymbol{d}$ is defined by (4.24a), i.e.,

$$\boldsymbol{d} = (d_x,\, d_y,\, d_z) = \sqrt{\frac{3}{4\pi}}(-\sqrt{2}a_{11}^{re},\, \sqrt{2}a_{11}^{im},\, a_{10}). \tag{4.26}$$

Thus the dipole defines a direction in the sky and determining $\boldsymbol{d}$ is equivalent to computing the coefficients a_{1m}. The temperature difference induced by the dipole is then the amplitude given by

$$\begin{aligned}\Delta T_d = \max\{|\boldsymbol{d}\cdot\hat{\boldsymbol{n}}|\} = |\boldsymbol{d}| &= \sqrt{\frac{3}{4\pi}}\sqrt{a_{10}^2 + 2(a_{11}^{re})^2 + 2(a_{11}^{im})^2} \\ &= \sqrt{\frac{3}{4\pi}}\sqrt{a_{10}^2 + 2|a_{11}|^2}\end{aligned} \tag{4.27}$$

where we have noted that $|a_{11}| = |a_{1-1}|$ to obtain the last equality. This shows that ΔT_d does not depend on the coordinates (θ, ϕ) and we can assume the dipole lies along the z-axis so that $a_{11} = a_{1-1} = 0$ and the above simplifies to

$$\Delta T_d = \frac{1}{2}\sqrt{\frac{3}{\pi}}a_{10}. \tag{4.28}$$

Working in harmonic space is more computationally efficient since we deal purely with large-angle fluctuations, so that the first few $a_{\ell m}$ carries most of the information about underlying sky. However it is more intuitive to see the equivalent expression in real space:

$$\Delta T_d = 3\left\langle T(\hat{\boldsymbol{n}})\,\hat{\boldsymbol{d}}\cdot\hat{\boldsymbol{n}}\right\rangle_\Omega, \tag{4.29}$$

where $\langle\cdot\rangle_\Omega = \frac{1}{4\pi}\int \mathrm{d}\hat{\boldsymbol{n}}(\cdot)$ is the spherical average and $\hat{\boldsymbol{d}}$ the dipole unit vector. This expression can be derived by first multiplying both sides of (4.24b) by $T(\hat{\boldsymbol{n}}) = \sum_{\ell'm'} a^*_{\ell'm'}Y^*_{\ell'm'}$

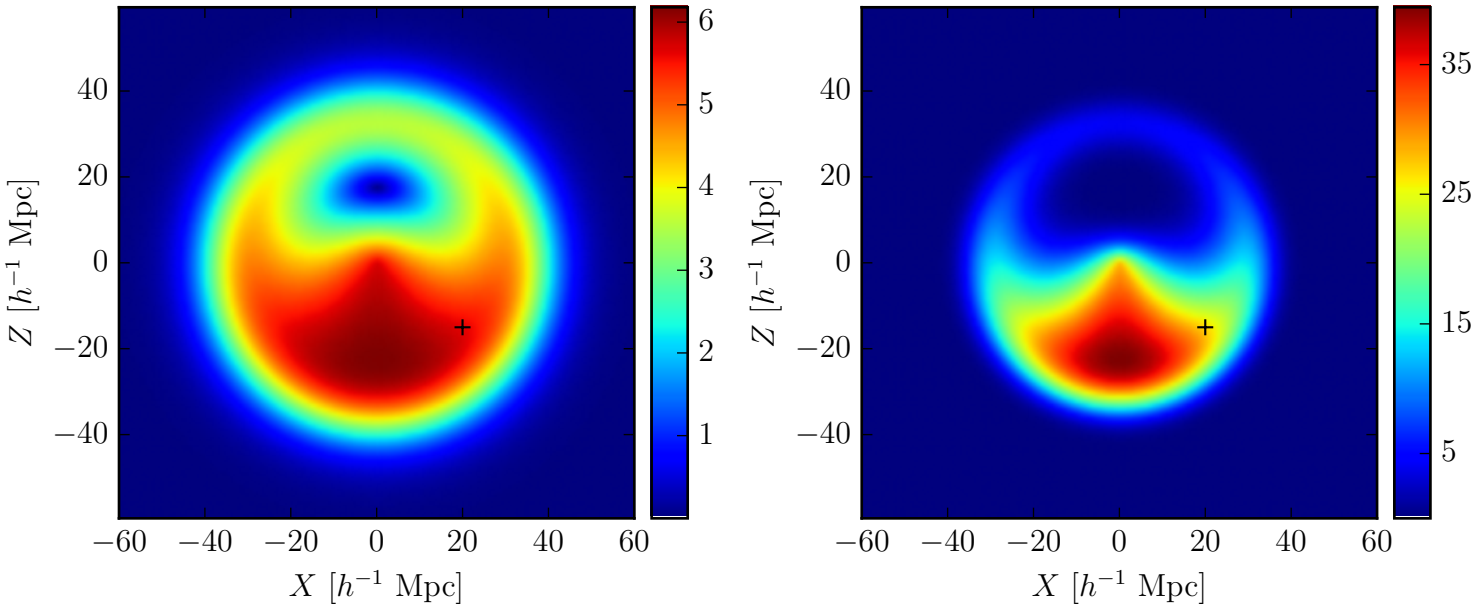

Figure 4.6: Dipole and quadrupole of the Szekeres model shown as a 2-dimensional cross section through the axis of cylindrical symmetry. The plane is divided into pixels of area $(1\,h^{-1}\,\mathrm{Mpc})^2$. *Left:* Dipole ΔT_d in units mK. *Right:* Quadrupole $\mathcal{D}_2 = 6\,C_2/(2\pi)$ in units $\mu\mathrm{K}^2 = 10^{-12}\,\mathrm{K}^2$. Coordinates are defined as $X \equiv R(t_0, r)\sin\theta\cos\phi = r\sin\theta$ and $Z \equiv R(t_0, r)\cos\theta = r\cos\theta$. The position of the Szekeres observer of [1] is indicated by the cross '+'.

then integrating over the sky to get

$$\frac{1}{4\pi}\sum_{m=-1}^{1}\sum_{\ell' m'} a_{1m}a^*_{\ell' m'}\int \mathrm{d}\hat{\boldsymbol{n}}\, Y_{1m}(\hat{\boldsymbol{n}})\, Y^*_{\ell' m'}(\hat{\boldsymbol{n}}) = \left\langle T(\hat{\boldsymbol{n}})\,\boldsymbol{d}\cdot\hat{\boldsymbol{n}}\right\rangle_\Omega . \tag{4.30}$$

Recalling the orthogonality relation (2.62) this simplifies to

$$\frac{1}{4\pi}\sum_{m=-1}^{1}|a_{1m}|^2 = \left\langle T(\hat{\boldsymbol{n}})\,\boldsymbol{d}\cdot\hat{\boldsymbol{n}}\right\rangle_\Omega , \tag{4.31}$$

and (4.29) follows after some algebraic manipulation.

In practice, one never has full coverage of the sky due to, for example, the presence of dust in the galactic plane, astrophysical point-sources, masked regions etc. The integral over the sky then becomes a weighted integral:

$$\int \mathrm{d}\hat{\boldsymbol{n}} \;\to\; \int \mathrm{d}\hat{\boldsymbol{n}}\, W(\hat{\boldsymbol{n}}), \tag{4.32}$$

where $W(\hat{\boldsymbol{n}})$ is some weighting function on the sky, and generically results in unwanted correlations between the C_ℓ. In general, $\boldsymbol{d}$ is found by solving the system of equations

$$\langle \hat{\boldsymbol{n}}\,\hat{\boldsymbol{n}}^T\rangle_\Omega\,\boldsymbol{d} = \langle T(\hat{\boldsymbol{n}})\,\hat{\boldsymbol{n}}\rangle_\Omega, \qquad \hat{\boldsymbol{n}} = (\hat{n}_x,\,\hat{n}_y,\,\hat{n}_z). \tag{4.33}$$

Note the average is taken over each entry, so the spherical average of a vector quantity is a vector of averages, e.g.,

$$\left\langle T(\hat{\boldsymbol{n}})\,\hat{\boldsymbol{n}}\right\rangle_\Omega \equiv \left(\left\langle T(\hat{\boldsymbol{n}})\,\hat{n}_x\right\rangle_\Omega, \left\langle T(\hat{\boldsymbol{n}})\,\hat{n}_y\right\rangle_\Omega, \left\langle T(\hat{\boldsymbol{n}})\,\hat{n}_z\right\rangle_\Omega\right). \tag{4.34}$$

In the case of full-sky coverage, the cross-terms vanish (e.g. $\langle \hat{n}_x \hat{n}_y\rangle_\Omega = 0$) and we find that $\left\langle \hat{\boldsymbol{n}}\hat{\boldsymbol{n}}^T\right\rangle_\Omega = \mathrm{diag}(\frac{1}{3}, \frac{1}{3}, \frac{1}{3})$, or $\langle \hat{n}_x^2\rangle_\Omega = \langle \hat{n}_y^2\rangle_\Omega = \langle \hat{n}_z^2\rangle_\Omega = \frac{1}{3}$. Thus (4.33) reduces to

$$\boldsymbol{d} = 3\left\langle T(\hat{\boldsymbol{n}})\,\hat{\boldsymbol{n}}\right\rangle_\Omega, \tag{4.35}$$

and in pixel space

$$\boldsymbol{d} \approx \frac{3}{N_{\rm pix}} \sum_{\rm ipix=1}^{N_{\rm pix}} T(\hat{\boldsymbol{n}}_{\rm ipix})\,\hat{\boldsymbol{n}}_{\rm ipix}. \tag{4.36}$$

Notice with the estimator (4.22) the temperature of the dipole may be written in a more convenient form as

$$\Delta T_d = \frac{3}{2}\sqrt{\frac{\tilde{C}_1}{\pi}}. \tag{4.37}$$

We remark that all multipoles admit a geometric description in terms of directional vectors [172] with the ℓth multipole associated with a set of ℓ Cartesian vectors. This geometric framework is often used to test alignments between multipoles, (e.g., the quadrupole-octupole alignment). Naturally, various statistics can be constructed by taking appropriate combinations of dot products and cross products etc.

Dipole and quadrupole in the LTB and Szekeres models

The dipole temperature for the LTB model is shown in fig. 4.5 for a set of theoretical observers placed around the void, while the case of the Szekeres model is shown in fig. 4.6. In the LTB model the dipole is evidently largest when the observer is located inside the void. Furthermore, comparing the profiles of the dipole and Hubble expansion (see fig. 4.1) it is clear that the peak dipole at roughly $35h^{-1}$ Mpc, coincides with the distance at which the gradient in the Hubble expansion (or differential Hubble expansion) is steepest. A local void also induces other large angle fluctuations, though the size of these contributions decrease with higher ℓ.

For the Szekeres model we see the size of quadrupole is much more sensitive to the position of the observer, with the maximum quadrupole occuring when the observer is placed near $(X, Z) = (0, 0)$. From fig. 4.2 this can be understood as the point along the axis of the mass dipole where the adjacent overdensity sharply transitions to the central underdensity.

It is interesting to consider the magnitude of the temperature dipole ΔT_d shown in fig. 4.6 for the case of observers just outside the structures, as this represents the much studied Rees–Sciama effect [123] for CMB photons that *cross* a nonlinear structure. For

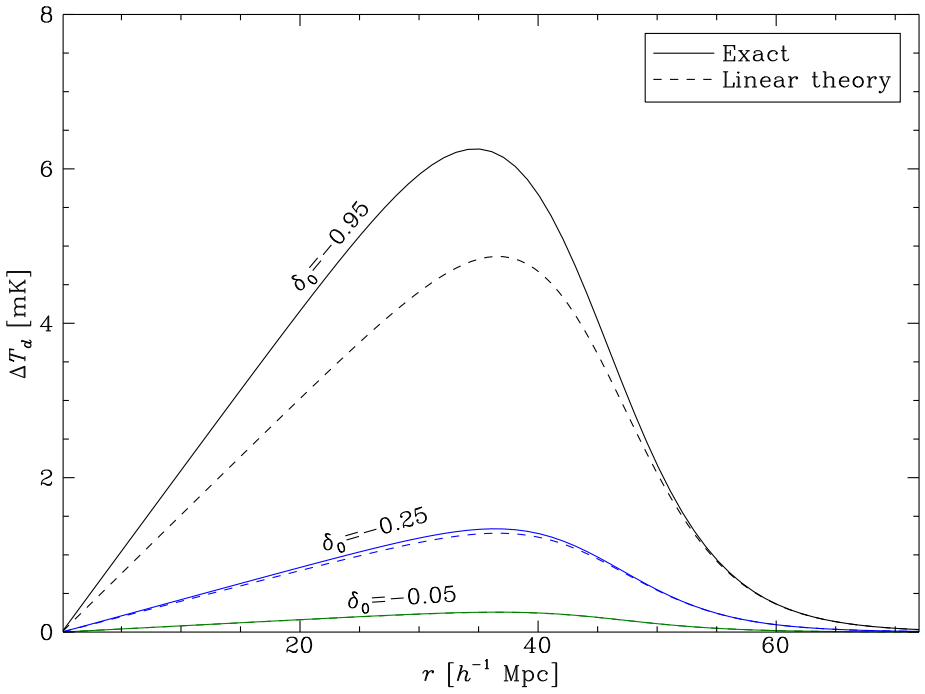

Figure 4.7: Comparison of the temperature dipole between exact LTB models and its linear theory expectation. Note both use the same density contrast profile (4.8).

the numerical example of fig. 4.6 we find $|\Delta T|/T < 3 \times 10^{-7}$, which is consistent with previous estimates which use larger voids and generate a somewhat larger amplitude [102, 103]. Since $|\Delta T|/T \sim 2 \times 10^{-3}$ for observers inside the void, this numerical example clearly demonstrates how the actual observer's position relative to the inhomogeneities is crucial in numerical modelling of realistic structures.

Furthermore, in fig. 4.6 the CMB quadrupole, for the observer whose dipole matches our CMB dipole in the LG frame (as shown by the cross), is $\mathcal{D}_2 = 26.6\mu\text{K}^2$, an order of magnitude smaller than the observed CMB quadrupole. This demonstrates how naïve numerical estimates for the quadrupole based on photons that traverse a void from one side to the other [113] cannot be relied on when realistically considering the origin of the CMB dipole using exact solutions of Einstein's equations. As Bolejko et al. [1] argue, there is considerable scope to include additional structures in the Szekeres model to further improve the fit of the Hubble expansion quadrupole, which is as yet not quite large enough to match that of the actual COMPOSITE sample.

4.3 Comparison with linear perturbation theory

There are two ways to obtain a large dipole. The first is with a very large structure such as a void, often several times the size of the Hubble radius. Take for instance a

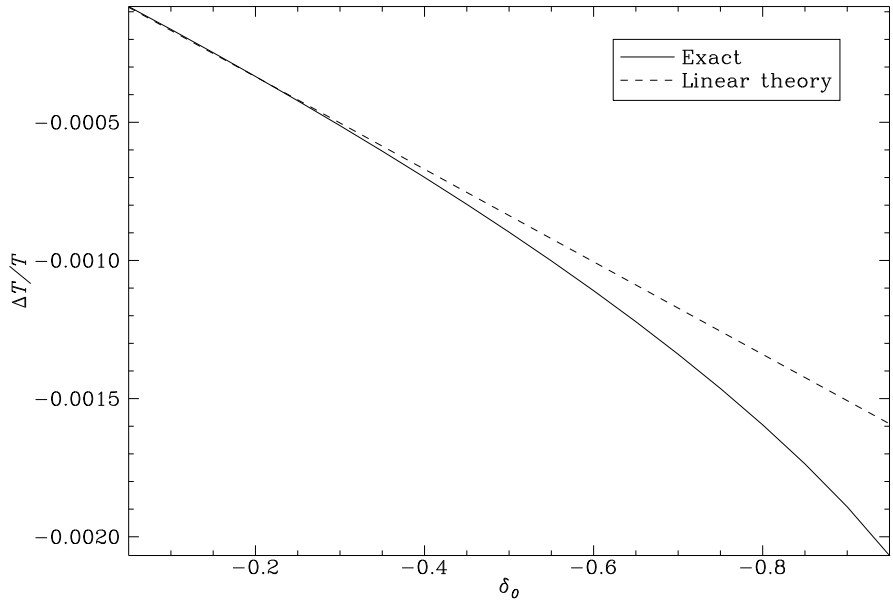

Figure 4.8: CMB fluctuation as seen by an off-centre LTB observer located at $r = 28\,h^{-1}\,\mathrm{Mpc}$.

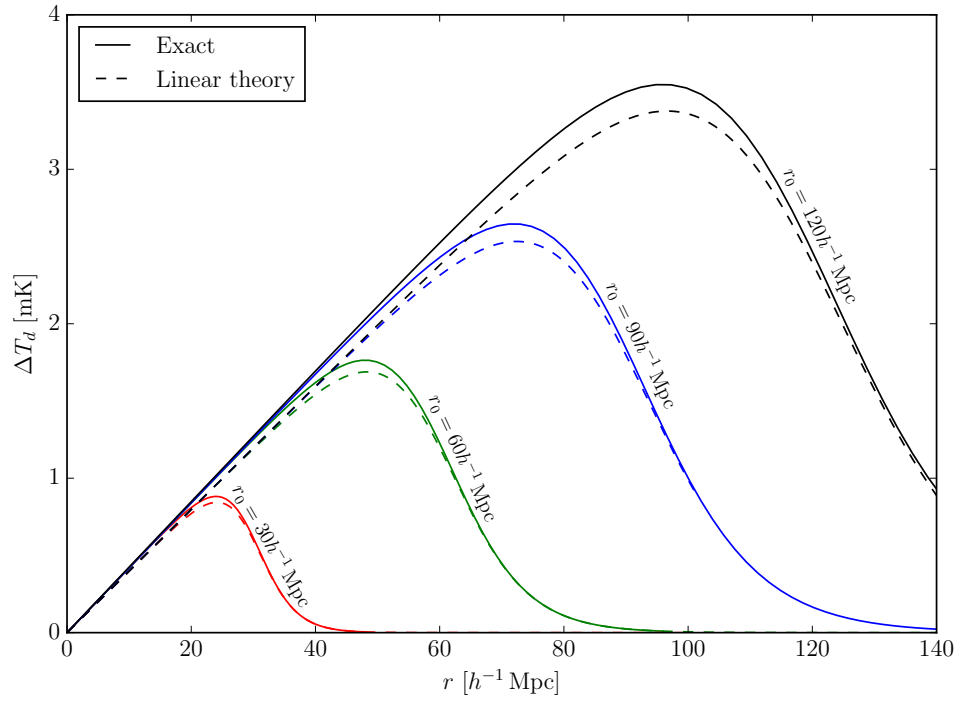

Figure 4.9: Comparison of the size, r_0 of the maximum possible dipole in the LTB model for different sized voids. Here we show for $\delta_0 = -0.25$ but the scaling is typical for all δ_0.

spherical void. The motion induced by local expansion gradients is proportional to the size of the void, so objects further away from the centre measures a larger dipole. This approach can be treated entirely within linear theory but it would appear unlikely, given

Gaussian primordial density fluctuations. The second way is with a very under- or over-dense structure $|\delta| \gg 0$. On one hand, this does not require anomalously large structures unlike the first approach, but on the other it is not amenable to analytic approximations. Such structures are, therefore, studied non-perturbatively using numerical methods.

Nevertheless we can still gain some intuition in the linear regime. Recall the peculiar velocity in linear theory is given by (2.36). For the spherically symmetric case, we substitute the density contrast (4.7) with $\alpha = 0$ into (2.36):

$$\begin{aligned} v(t,r) &= -a(t)\,H(t)\,f(t)\,r^{-2}\int_0^r \Delta(r')\,r'^2\,\mathrm{d}r' \\ &= -\frac{1}{3}a(t)\,H(t)\,f(t)\,r\,\hat{\Delta}(r) \end{aligned} \tag{4.38}$$

where

$$\hat{\Delta}(r) \equiv \frac{3}{4\pi r^3}\int_0^r \mathrm{d}r'\,r'^2\int_0^\pi \mathrm{d}\theta\,\sin\theta\int_0^{2\pi}\mathrm{d}\phi\,\Delta(r'). \tag{4.39}$$

is the average density contrast of a ball of radius r. Evaluating the integral by hand is long and tedious, however, the final result is surprisingly simple:

$$\hat{\Delta}(r) = \frac{\delta_0}{\mathrm{e}^{(r-r_0)/\Delta r}+1}. \tag{4.40}$$

As an aside, a void is said to be compensated if $\hat{\Delta}(r) \to 0$, as $r \to \infty$, i.e., all the matter removed must be replaced elsewhere. Clearly, (4.40) vanishes in the limit $r \to \infty$ so, at least in the linear regime, the LTB void is compensated.

Since the temperature dipole ΔT_d is linearly proportional to $|v(t,r)|$, we can find the dependence of the peculiar velocity on the size of the void r_0 by solving $\frac{\partial}{\partial r}v = 0$ and substituting the solution back into (4.38). Although we cannot find a closed form solution for $r_{\max}$ with this particular density contrast profile, we find that $\Delta T_d \propto |v(t,r)|$ scales linearly with the size of the void, i.e., $\Delta T_d \sim r_0$. This shows that in order to match the observed CMB dipole in linear theory, one must be willing to accept the fact that we happen to reside in a very large void. As shown in fig. 4.7, a more plausible scenario is that of a dipole instead arising from a highly underdense void, with a density contrast of approximately -0.9. Certainly, such a hypothesis is not at odds with observations that indicates a late-universe dominated by nonlinear voids [29, 34, 35].

Solving the perturbation equations of chapter 2 we compute the temperature fluctuation of a photon passing through the centre of the void as measured by an observer in the void. This is shown in fig. 4.8. Since we compare the *total* CMB anisotropy with the LTB model, we compute all terms of (2.58) (excluding the unobservable monopole). In linear theory the off-centre observer's dipole moment is indeed much larger than the ISW effect. Not surprisingly linear theory breaks down well before the density contrast reaches the magnitude of our LTB model, in which $\delta_0 = -0.95$. However visually inspecting fig. 4.8, linear theory does appear to agree well with the exact predictions when

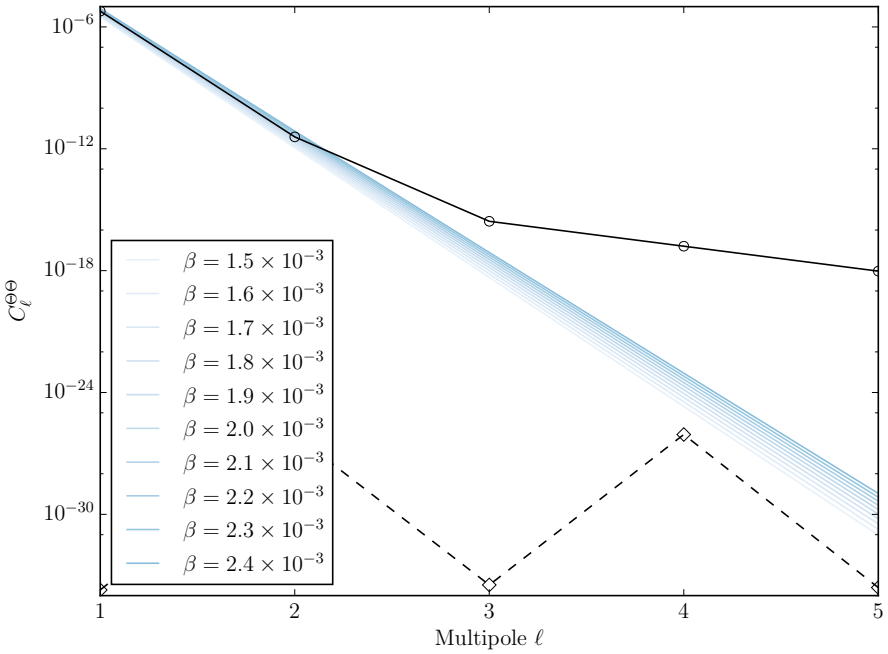

Figure 4.10: Power spectrum of a uniform temperature map that has been boosted (blue lines). The LTB model power spectrum is indicated by the solid black line. For reference the dashed line indicates the numerical noise level determined from a uniform temperature map.

$\delta_0 > -0.2$. Notice that in linear theory a large dipole can be achieved without requiring a highly underdense void provided the void is (unrealistically) large (see fig. 4.9). We remark that while linear theory clearly breaks down for $\delta_0 = -0.95$, as shown in fig. 4.7, the location of the peak of ΔT_d predicted in this regime still corresponds well with the exact prediction.

4.4 Comparison of the kinematic and non-kinematic dipoles in the LG frame

We next compare the coefficients $a_{\ell m}$ of a uniform map of temperature T_0 that has been boosted, with that of an off-centre LTB observer. Due to the azimuthal symmetry we again take $\hat{\boldsymbol{\beta}} = \hat{\boldsymbol{z}}$, so that we only need to consider the zonal modes $a_{\ell 0}$. The coefficients are given by

$$a_{\ell 0} = \int_0^{2\pi} \mathrm{d}\phi \int_0^{\pi} \mathrm{d}\theta \sin\theta \, \frac{T_0}{\gamma(1 - \beta\cos\theta)} \, Y^*_{\ell 0}(\theta, \phi) \tag{4.41}$$

and, as it turns out, for each ℓ this integral can be expressed in terms of elementary functions. The first few $a_{\ell 0}$ are

$$a_{00} = \sqrt{\pi}\frac{T_0}{\beta\gamma}\ln\left(\frac{1+\beta}{1-\beta}\right) = T_0\left(1 - \frac{1}{6}\beta^2 + \mathcal{O}(\beta^4)\right) \tag{4.42a}$$

$$a_{10} = \sqrt{3\pi}\frac{T_0}{\beta^2\gamma}\left[-2\beta + \ln\left(\frac{1+\beta}{1-\beta}\right)\right] = T_0\left(\beta + \frac{1}{10}\beta^3 + \mathcal{O}(\beta^5)\right) \tag{4.42b}$$

$$a_{20} = -\frac{1}{2}\sqrt{5\pi}\frac{T_0}{\beta^3\gamma}\left[(\beta^2-3)\ln\left(\frac{1+\beta}{1-\beta}\right) + 6\beta\right] = T_0\left(\beta^2 + \frac{5}{14}\beta^4 + \mathcal{O}(\beta^6)\right) \tag{4.42c}$$

$$a_{30} = -\frac{1}{6}\sqrt{7\pi}\frac{T_0}{\beta^4\gamma}\left[(9\beta^2-15)\ln\left(\frac{1+\beta}{1-\beta}\right) - 8\beta^3 + 30\beta\right] = T_0\left(\beta^3 + \frac{11}{18}\beta^5 + \mathcal{O}(\beta^7)\right) \tag{4.42d}$$

For small β, the coefficients clearly have the asymptotic behaviour $a_{\ell 0} \sim \beta^\ell$. In particular, for the dipole (see (4.28)) we have the simple scaling $\Delta T_d \propto a_{10} \sim \beta$. Given that ΔT_d is in milliKelvin, it follows that $\beta \sim 10^{-3}$. While a boost contributes to all multipoles, the quadratic and higher-order terms are $\lesssim 10^{-6}$, i.e., one order of magnitude smaller than the primordial fluctuations and beyond the sensitivity of current detectors.

To compare the boosted blackbody $T'(\hat{\boldsymbol{n}}')$ with the temperature map seen by an off-centre void observer in the LTB model we define the anisotropy

$$\Theta(\hat{\boldsymbol{n}}') = \frac{T'(\hat{\boldsymbol{n}}') - \left\langle T'(\hat{\boldsymbol{n}}')\right\rangle_{\Omega'}}{\left\langle T'(\hat{\boldsymbol{n}}')\right\rangle_{\Omega'}}. \tag{4.43}$$

Note this is independent of T_0 and can be compared directly with the LTB model. We emphasise that the dimensionless fluctuation Θ of the LTB model, (or for that matter any cosmological solution of the field equations), can be expressed in terms of redshift only, that is, it is independent of T_0. Therefore, this eliminates any ambiguity related to how the monopole temperature is set since $\left\langle\Theta(\hat{\boldsymbol{n}}')\right\rangle_{\Omega'} = 0$.

The dipole the off-centre observer will measure we take to be 5.64 mK, consistent with the LG frame dipole. We investigate the size of the boost needed to match this dipole.

The power spectrum of the of the ray traced CMB in the LTB model is computed using HEALPix, while we use the analytic formulae (4.42a)–(4.42d) for the boosted spectrum. The results are shown in fig. 4.10. Superscripts of $C_\ell^{\Theta\Theta}$ are used emphasise that it is the power spectrum of Θ. Beyond $C_2^{\Theta\Theta}$ the power spectrums begin to diverge, but as far as current detectors are concerned, both spectrums are observationally degenerate. Furthermore, the multipoles of the LTB model also show a hierarchical scaling $C_1^{\Theta\Theta} > C_2^{\Theta\Theta} > C_3^{\Theta\Theta} > \ldots$ in the same way as a boost. This puts a limit on how much the quadrupole observed by Planck can be produced by a foreground inhomogeneity.

4.5 Boosting the LG frame to the heliocentric frame

Aside from an induced dipole, there are two secondary effects on the CMB associated with a Lorentz boost, namely, the aberration and modulation effects.

From a practical standpoint, the aberration effect presents a problem in that boosting a HEALPix map pixel by pixel does not result in another HEALPix map. Thus each pixel of the boosted map cannot be said to be uniformly spaced as the pixel density is now higher (lower) towards (away from) the boost direction. Simply, the number of pixels in each hemisphere is no longer equal. To get around this, often one transforms the map in pixel space to harmonic space, then applies the boost. This problem can be overcome, owing to the magnitude of the boosts being small ($\beta \sim 10^{-3}$) and the fact that the temperature maps of the LTB and Szekeres models do not induce small-scale fluctuations. For this reason we only need to consider the first few multipoles.

In this section we give formulae relating the boosted monopole and dipole in two frames, one boosted relative to the other. The formulae derived are (4.68) and (4.69) and we use these to investigate the possibility of the existence of a non-kinematic dipole in the heliocentric frame. In the following, we outline the calculation based on the assumption that the boost is small, expanding to second-order in β. The advantage of these formulae is that we are able to avoid having to boost the entire CMB map. If, however, we look at boosting more featureful maps with significant fluctuations beyond $\ell \geq 3$ then the following analysis no longer holds.

Recall the key equations for a local Lorentz boost of the (generally anisotropic) mean temperature of a blackbody distribution are (1.14) and (1.10). We restate them here for convenience to the reader:

$$T'(\hat{\boldsymbol{n}}') = \frac{T(\hat{\boldsymbol{n}})}{\gamma(1-\boldsymbol{\beta}\cdot\hat{\boldsymbol{n}}')} = \gamma(1+\boldsymbol{\beta}\cdot\hat{\boldsymbol{n}})T(\hat{\boldsymbol{n}}), \tag{4.44a}$$

$$\hat{\boldsymbol{n}}' = \frac{\hat{\boldsymbol{n}} + [\gamma\beta + (\gamma-1)\hat{\boldsymbol{\beta}}\cdot\hat{\boldsymbol{n}}]\hat{\boldsymbol{\beta}}}{\gamma(1+\boldsymbol{\beta}\cdot\hat{\boldsymbol{n}})}, \tag{4.44b}$$

where the primes denote the quantities in the boosted frame. Without loss of generality we assume the boost is in the z-direction[4] so $\hat{\boldsymbol{\beta}} = \hat{\boldsymbol{z}}$, from which it follows $\hat{\boldsymbol{z}} = \hat{\boldsymbol{z}}'$. We project $\hat{\boldsymbol{n}}'$ onto the z-axis to find

$$\cos\theta' = \frac{\cos\theta + \gamma\beta + (\gamma-1)\cos\theta}{\gamma(1+\beta\cos\theta)} = \frac{\cos\theta+\beta}{1+\beta\cos\theta}, \tag{4.45}$$

and taking the differential we obtain

$$\sin\theta'\,\mathrm{d}\theta' = \frac{\sin\theta\,\mathrm{d}\theta}{\gamma^2(1+\beta\cos\theta)^2}. \tag{4.46}$$

[4]We can always rotate the coordinate system before boosting so that the boost is in the z-direction from which the angle θ is measured. As we are attempting to obtain formulae for the CMB monopole and dipole, we should find that these observables are independent of the observer's angular coordinates.

Since $\phi = \phi'$ for a boost along the z-direction, the differential solid angle $\mathrm{d}\Omega = \sin\theta\,\mathrm{d}\theta\,\mathrm{d}\phi$ in the boosted frame transforms as

$$\mathrm{d}\Omega' = \frac{\mathrm{d}\Omega}{\gamma^2(1+\beta\cos\theta)^2} \simeq \left[1 - 2\boldsymbol{\beta}\cdot\hat{\boldsymbol{n}} + 3(\boldsymbol{\beta}\cdot\hat{\boldsymbol{n}})^2 - \beta^2\right]\mathrm{d}\Omega, \tag{4.47}$$

where $\simeq$ will denote equality to second order in β.

Since we need to distinguish what frame the spherical average is taken in, we will use $\langle\cdot\rangle_{\Omega'}$ to denote the spherical average in the boosted frame.

4.5.1 The monopole

We now compute the monopole temperature in the boosted frame by expanding (4.44a) in powers of β:

$$\begin{aligned}\left\langle T'(\hat{\boldsymbol{n}}')\right\rangle_{\Omega'} &= \left\langle T(\hat{\boldsymbol{n}})\gamma(1+\boldsymbol{\beta}\cdot\hat{\boldsymbol{n}})\right\rangle_{\Omega'} \\ &= \left\langle T(\hat{\boldsymbol{n}})[1+\boldsymbol{\beta}\cdot\hat{\boldsymbol{n}} + \frac{1}{2}\beta^2 + \mathcal{O}(\beta^3)]\right\rangle_{\Omega'} \\ &\simeq \left\langle T(\hat{\boldsymbol{n}})\right\rangle_{\Omega'} + \left\langle T(\hat{\boldsymbol{n}})\boldsymbol{\beta}\cdot\hat{\boldsymbol{n}}\right\rangle_{\Omega'} + \frac{1}{2}\beta^2\left\langle T(\hat{\boldsymbol{n}})\right\rangle_{\Omega'}\end{aligned} \tag{4.48}$$

In the following, we will rewrite each term on the last line above in terms of quantities in the unboosted frame, i.e., in terms of unprimed quantities.

Using (4.47), we first note the spherical average of any observable $A(\hat{\boldsymbol{n}})$ as measured in the boosted frame is related to the unboosted frame by

$$\left\langle A(\hat{\boldsymbol{n}})\right\rangle_{\Omega'} \simeq \left\langle A(\hat{\boldsymbol{n}})\right\rangle_{\Omega}(1-\beta^2) - 2\left\langle A(\hat{\boldsymbol{n}})\boldsymbol{\beta}\cdot\hat{\boldsymbol{n}}\right\rangle_{\Omega} + 3\left\langle(\boldsymbol{\beta}\cdot\hat{\boldsymbol{n}})^2 A(\hat{\boldsymbol{n}})\right\rangle_{\Omega}. \tag{4.49}$$

Applying this to the observed temperature in (4.48) the respective terms may be rewritten as follows

$$\left\langle T(\hat{\boldsymbol{n}})\right\rangle_{\Omega'} \simeq \left\langle T(\hat{\boldsymbol{n}})\right\rangle_{\Omega}(1-\beta^2) - 2\left\langle T(\hat{\boldsymbol{n}})\boldsymbol{\beta}\cdot\hat{\boldsymbol{n}}\right\rangle_{\Omega} + 3\left\langle(\boldsymbol{\beta}\cdot\hat{\boldsymbol{n}})^2 T(\hat{\boldsymbol{n}})\right\rangle_{\Omega}, \tag{4.50a}$$

$$\left\langle T(\hat{\boldsymbol{n}})\boldsymbol{\beta}\cdot\hat{\boldsymbol{n}}\right\rangle_{\Omega'} \simeq \left\langle T(\hat{\boldsymbol{n}})\boldsymbol{\beta}\cdot\hat{\boldsymbol{n}}\right\rangle_{\Omega} - 2\left\langle(\boldsymbol{\beta}\cdot\hat{\boldsymbol{n}})^2 T(\hat{\boldsymbol{n}})\right\rangle_{\Omega}, \tag{4.50b}$$

$$\frac{1}{2}\beta^2\left\langle T(\hat{\boldsymbol{n}})\right\rangle_{\Omega'} \simeq \frac{1}{2}\beta^2\left\langle T(\hat{\boldsymbol{n}})\right\rangle_{\Omega}, \tag{4.50c}$$

where we neglect terms $\mathcal{O}(\beta^3)$. Hence (4.48) becomes

$$\left\langle T'(\hat{\boldsymbol{n}}')\right\rangle_{\Omega'} \simeq \left\langle T(\hat{\boldsymbol{n}})\right\rangle_{\Omega}(1-\frac{1}{2}\beta^2) - \left\langle T(\hat{\boldsymbol{n}})\,\boldsymbol{\beta}\cdot\hat{\boldsymbol{n}}\right\rangle_{\Omega} + \left\langle(\boldsymbol{\beta}\cdot\hat{\boldsymbol{n}})^2\,T(\hat{\boldsymbol{n}})\right\rangle_{\Omega}. \tag{4.51}$$

Let us check that this reduces to the familiar case when $T(\hat{\boldsymbol{n}}) = T = \text{const}$. Indeed

$$\left\langle T'(\hat{\boldsymbol{n}}')\right\rangle_{\Omega'} \simeq T(1-\frac{1}{2}\beta^2) - T\left\langle\boldsymbol{\beta}\cdot\hat{\boldsymbol{n}}\right\rangle_{\Omega} + T\left\langle(\boldsymbol{\beta}\cdot\hat{\boldsymbol{n}})^2\right\rangle_{\Omega} \tag{4.52a}$$

$$= T(1-\frac{1}{6}\beta^2) \tag{4.52b}$$

where we have used

$$\langle \boldsymbol{u} \cdot \hat{\boldsymbol{n}} \rangle_\Omega = 0 \qquad \text{and} \qquad \left\langle (\boldsymbol{u} \cdot \hat{\boldsymbol{n}})^2 \right\rangle_\Omega = \frac{1}{3}|\boldsymbol{u}|^2, \tag{4.53}$$

for any vector $\boldsymbol{u}$.

The temperature $T(\hat{\boldsymbol{n}})$ can be written in real space, rather than harmonic space, as

$$T(\hat{\boldsymbol{n}}) = \left\langle T(\hat{\boldsymbol{n}}) \right\rangle_\Omega + \boldsymbol{d} \cdot \hat{\boldsymbol{n}} + \ldots, \tag{4.54}$$

where $\boldsymbol{d} \cdot \hat{\boldsymbol{n}} = \sum_m a_{1m} Y_{1m}(\hat{\boldsymbol{n}})$ and the ellipsis denotes the remaining multipoles, i.e., quadrupole, octupole etc. Substituting this into $\left\langle T(\hat{\boldsymbol{n}})\, \hat{\boldsymbol{n}} \right\rangle_\Omega$ we find

$$\left\langle T(\hat{\boldsymbol{n}})\, \hat{\boldsymbol{n}} \right\rangle_\Omega = \langle \hat{\boldsymbol{n}} \rangle_\Omega \left\langle T(\hat{\boldsymbol{n}}) \right\rangle_\Omega + \left\langle (\boldsymbol{d} \cdot \hat{\boldsymbol{n}})\, \hat{\boldsymbol{n}} \right\rangle_\Omega + \ldots = \left\langle (\boldsymbol{d} \cdot \hat{\boldsymbol{n}})\, \hat{\boldsymbol{n}} \right\rangle_\Omega + \ldots, \tag{4.55}$$

since $\langle \hat{\boldsymbol{n}} \rangle_\Omega = 0$. It therefore follows that the second term on the right-hand side of (4.51) is

$$\left\langle T(\hat{\boldsymbol{n}})\, \boldsymbol{\beta} \cdot \hat{\boldsymbol{n}} \right\rangle_\Omega = \boldsymbol{\beta} \cdot \left\langle T(\hat{\boldsymbol{n}})\, \hat{\boldsymbol{n}} \right\rangle_\Omega = \boldsymbol{\beta} \cdot \left\langle (\boldsymbol{d} \cdot \hat{\boldsymbol{n}})\, \hat{\boldsymbol{n}} \right\rangle_\Omega + \ldots = \frac{1}{3} \boldsymbol{\beta} \cdot \boldsymbol{d} + \ldots, \tag{4.56}$$

while the last term of (4.51) becomes

$$\begin{aligned} \left\langle (\boldsymbol{\beta} \cdot \hat{\boldsymbol{n}})^2\, T(\hat{\boldsymbol{n}}) \right\rangle_\Omega &= \left\langle (\boldsymbol{\beta} \cdot \hat{\boldsymbol{n}})^2 \right\rangle_\Omega \left\langle T(\hat{\boldsymbol{n}}) \right\rangle_\Omega + \left\langle (\boldsymbol{\beta} \cdot \hat{\boldsymbol{n}})^2\, \boldsymbol{d} \cdot \hat{\boldsymbol{n}} \right\rangle_\Omega + \ldots \\ &= \frac{1}{3} \beta^2 \left\langle T(\hat{\boldsymbol{n}}) \right\rangle_\Omega + \ldots \end{aligned} \tag{4.57}$$

In arriving at (4.56) and (4.57) we used the fact that for any vectors $\boldsymbol{u}$ and $\boldsymbol{v}$ we have the general results

$$\left\langle (\boldsymbol{u} \cdot \hat{\boldsymbol{n}})\, \hat{\boldsymbol{n}} \right\rangle_\Omega = \frac{1}{3} \boldsymbol{u} \qquad \text{and} \qquad \left\langle (\boldsymbol{u} \cdot \hat{\boldsymbol{n}})(\boldsymbol{v} \cdot \hat{\boldsymbol{n}})\, \hat{\boldsymbol{n}} \right\rangle_\Omega = 0. \tag{4.58}$$

This can be verified by simply evaluating the spherical averages.

In the case of our models, the next highest contribution after the dipole is the quadrupole, which is order $10^{-6}\,\mathrm{K}$. It turns out the quadrupole can be neglected, as we show in appendix C. We thus have

$$T(\hat{\boldsymbol{n}}) \approx \left\langle T(\hat{\boldsymbol{n}}) \right\rangle_\Omega + \boldsymbol{d} \cdot \hat{\boldsymbol{n}}, \tag{4.59}$$

i.e., at the level of precision we are interested in, we can simply approximate the temperature as the sum of a monopole and dipole. Since the boosts we are considering are small (e.g. $\beta \sim 10^{-3}$) we can write

$$\left\langle T(\hat{\boldsymbol{n}})\, \boldsymbol{\beta} \cdot \hat{\boldsymbol{n}} \right\rangle_\Omega \approx \frac{1}{3} \boldsymbol{\beta} \cdot \boldsymbol{d}, \tag{4.60}$$

with corrections on the order of $10^{-9}\,\mathrm{K}$. Hence for our models we have the simple formula

$$\left\langle T'(\hat{\boldsymbol{n}}') \right\rangle_{\Omega'} \approx \left\langle T(\hat{\boldsymbol{n}}) \right\rangle_\Omega (1 - \frac{1}{6}\beta^2) - \frac{1}{3} \boldsymbol{\beta} \cdot \boldsymbol{d}. \tag{4.61}$$

The last term gives the correction when $T(\hat{\boldsymbol{n}})$ is not constant, as will be the case in the frame of the Local Group.

4.5.2 The dipole

We now turn to obtaining an expression for the dipole in the boosted frame in terms of the quantities in the unboosted frame. Using (4.29), the dipole in the boosted frame is

$$\Delta T'_d = 3\left\langle T'(\hat{\boldsymbol{n}}')\,\hat{\boldsymbol{d}}'\cdot\hat{\boldsymbol{n}}'\right\rangle_{\Omega'} \tag{4.62a}$$

$$= 3\left\langle T(\hat{\boldsymbol{n}})\gamma(1+\boldsymbol{\beta}\cdot\hat{\boldsymbol{n}})\,\hat{\boldsymbol{d}}'\cdot\hat{\boldsymbol{n}}'\right\rangle_{\Omega'} \tag{4.62b}$$

where $\hat{\boldsymbol{d}}'$ is the direction of the dipole in the boosted frame and we have used (4.44a) in the second line. We define

$$\boldsymbol{q} := \hat{\boldsymbol{d}}' - \hat{\boldsymbol{d}}, \tag{4.63}$$

with $\boldsymbol{q} = \boldsymbol{q}(\beta)$ and $\boldsymbol{q}(0) = 0$ so that $\hat{\boldsymbol{d}}' = \hat{\boldsymbol{d}}$ when $\beta = 0$. Expanding (4.62b) we then have

$$\begin{aligned}\gamma(1+\boldsymbol{\beta}\cdot\hat{\boldsymbol{n}})\,\hat{\boldsymbol{d}}'\cdot\hat{\boldsymbol{n}}' &= \hat{\boldsymbol{d}}'\cdot\hat{\boldsymbol{n}} + \left[\gamma\beta + (\gamma-1)\hat{\boldsymbol{\beta}}\cdot\hat{\boldsymbol{n}}\right]\hat{\boldsymbol{d}}'\cdot\hat{\boldsymbol{\beta}} \\ &= \hat{\boldsymbol{d}}\cdot\hat{\boldsymbol{n}} + \boldsymbol{q}\cdot\hat{\boldsymbol{n}} + \boldsymbol{\beta}\cdot\hat{\boldsymbol{d}}' + \mathcal{O}(\beta^2)\end{aligned} \tag{4.64}$$

where we have used (4.44b) in the first line and expanded the square brackets to second order in β. Hence

$$\begin{aligned}\Delta T'_d &= 3\left\langle T(\hat{\boldsymbol{n}})\,\hat{\boldsymbol{d}}\cdot\hat{\boldsymbol{n}}\right\rangle_{\Omega'} + 3\left\langle T(\hat{\boldsymbol{n}})\,\boldsymbol{q}\cdot\hat{\boldsymbol{n}}\right\rangle_{\Omega'} + 3\,\boldsymbol{\beta}\cdot\hat{\boldsymbol{d}}'\left\langle T(\hat{\boldsymbol{n}})\right\rangle_{\Omega'} + \mathcal{O}(\beta^2) \\ &= 3\left\langle T(\hat{\boldsymbol{n}})\,\hat{\boldsymbol{d}}\cdot\hat{\boldsymbol{n}}\right\rangle_{\Omega} + 3\left\langle T(\hat{\boldsymbol{n}})\,\boldsymbol{q}\cdot\hat{\boldsymbol{n}}\right\rangle_{\Omega} + 3\,\boldsymbol{\beta}\cdot\hat{\boldsymbol{d}}'\left\langle T(\hat{\boldsymbol{n}})\right\rangle_{\Omega} \\ &\quad - 6\left\langle T(\hat{\boldsymbol{n}})(\hat{\boldsymbol{d}}'\cdot\hat{\boldsymbol{n}})(\boldsymbol{\beta}\cdot n)\right\rangle_{\Omega} + \mathcal{O}(\beta^2)\end{aligned} \tag{4.65}$$

where we have made use of (4.49) in the second line.

For our models we insert (4.59) into the above to find

$$\begin{aligned}\Delta T'_d \simeq \Delta T_d &+ 3\,\boldsymbol{q}\cdot\left\langle(\boldsymbol{d}\cdot\hat{\boldsymbol{n}})\,\hat{\boldsymbol{n}}\right\rangle_{\Omega} + 3\,\boldsymbol{\beta}\cdot\hat{\boldsymbol{d}}'\left\langle T(\hat{\boldsymbol{n}})\right\rangle_{\Omega} \\ &- 6\,\boldsymbol{\beta}\cdot\left\langle(\hat{\boldsymbol{d}}'\cdot\hat{\boldsymbol{n}})\,\hat{\boldsymbol{n}}\right\rangle_{\Omega}\left\langle T(\hat{\boldsymbol{n}})\right\rangle_{\Omega} - 6\,\boldsymbol{\beta}\cdot\left\langle(\hat{\boldsymbol{d}}'\cdot\hat{\boldsymbol{n}})(\boldsymbol{d}\cdot\hat{\boldsymbol{n}})\,\hat{\boldsymbol{n}}\right\rangle_{\Omega},\end{aligned} \tag{4.66}$$

where we have used (4.53) and $\Delta T_d = 3\left\langle T(\hat{\boldsymbol{n}})\,\hat{\boldsymbol{d}}\cdot\hat{\boldsymbol{n}}\right\rangle_{\Omega}$. Finally by recalling (4.58), we obtain

$$\begin{aligned}\Delta T'_d &\simeq \Delta T_d(1+\boldsymbol{q}\cdot\hat{\boldsymbol{d}}) + \boldsymbol{\beta}\cdot\hat{\boldsymbol{d}}'\left\langle T(\hat{\boldsymbol{n}})\right\rangle_{\Omega} \\ &= (\hat{\boldsymbol{d}}\cdot\hat{\boldsymbol{d}}')\Delta T_d + \boldsymbol{\beta}\cdot\hat{\boldsymbol{d}}'\left\langle T(\hat{\boldsymbol{n}})\right\rangle_{\Omega}\end{aligned} \tag{4.67}$$

This equation as well as (4.61) are the key equations.

These equations can be rewritten in a more convenient form as

$$\overline{T}' \simeq \overline{T}\left(1 - \frac{1}{6}\beta^2 - \frac{1}{3}\Theta_d\,\beta\cos\alpha_1\right) \tag{4.68}$$

$$\Delta T'_d \simeq \overline{T}\left(\Theta_d\,\cos\alpha_3 + \beta\cos\alpha_2\right) \tag{4.69}$$

where we have introduced the separation angles α_1, α_2 and α_3 defined by $\hat{\boldsymbol{\beta}} \cdot \hat{\boldsymbol{d}} = \cos\alpha_1$, $\hat{\boldsymbol{\beta}} \cdot \hat{\boldsymbol{d}}' = \cos\alpha_2$ and $\hat{\boldsymbol{d}} \cdot \hat{\boldsymbol{d}}' = \cos\alpha_3$. We also defined the shorthands $\overline{T} \equiv \langle T(\hat{\boldsymbol{n}}) \rangle_{\Omega}$, $\overline{T}' \equiv \langle T'(\hat{\boldsymbol{n}}') \rangle_{\Omega'}$ and the unitless dipole $\Theta_d \equiv \Delta T_d / \overline{T}$, which we note can be computed directly from the model without having to input temperature, that is, it can be expressed in terms of redshift only.

4.5.3 Estimating the non-kinematic dipole in the heliocentric frame

Using the formulae derived above we wish to compute the dipole of the residual temperature (1.30), which we rewrite here in a slightly different form as

$$\Delta T_{\rm nk} \equiv T_1(\hat{\boldsymbol{n}}^{\rm hel}) - T_2(\hat{\boldsymbol{n}}^{\rm hel}), \tag{4.70}$$

where

$$T_1(\hat{\boldsymbol{n}}^{\rm hel}) \equiv \frac{T(\hat{\boldsymbol{n}}^{\rm LG})}{\gamma_{\rm hel-LG}(1 - \boldsymbol{\beta}_{\rm hel-LG} \cdot \hat{\boldsymbol{n}}^{\rm hel})}, \tag{4.71}$$

and

$$T_2(\hat{\boldsymbol{n}}^{\rm hel}) \equiv \frac{\overline{T}^{\rm CMB}}{\gamma_{\rm hel-CMB}(1 - \boldsymbol{\beta}_{\rm hel-CMB} \cdot \hat{\boldsymbol{n}}^{\rm hel})}. \tag{4.72}$$

Here $\boldsymbol{\beta}_{\rm hel-CMB}$ is the boost from the CMB frame to heliocentric frame with $\gamma_{\rm hel-CMB}$ its respective Lorentz factor, $\boldsymbol{\beta}_{\rm hel-LG}$ is the boost from the LG frame to heliocentric frame with $\gamma_{\rm hel-LG}$ its respective Lorentz factor, $T(\hat{\boldsymbol{n}}^{\rm LG})$ is the temperature seen by an observer in a frame comoving with the dust which we take to be the frame of an observer in the LTB model located at $r = 28h^{-1}$ Mpc. If $T(\hat{\boldsymbol{n}}^{\rm LG})$ is the temperature of the CMB resulting from a boost, as it is assumed in the standard model, then $\Delta T_{\rm nk} = 0$. This is because the assumption that the CMB dipole in the LG frame is due to a boost implies

$$T(\hat{\boldsymbol{n}}^{\rm LG}) = \frac{\overline{T}^{\rm CMB}}{\gamma_{\rm LG-CMB}(1 - \boldsymbol{\beta}_{\rm LG-CMB} \cdot \hat{\boldsymbol{n}}^{\rm LG})}, \tag{4.73}$$

with $\boldsymbol{\beta}_{\rm LG-CMB}$ the boost from the CMB frame to LG Frame, so that boosting from the LG frame to the heliocentric frame is then equivalent to deboosting from the LG frame followed immediately by boosting to the heliocentric frame. Thus a non-zero dipole of $\Delta T_{\rm nk}$ entails a *non-kinematic dipole*, as discussed in §1.3.4. The non-kinematic dipole can then be estimated by computing the difference of the dipoles of $T_1(\hat{\boldsymbol{n}})$ and $T_2(\hat{\boldsymbol{n}})$.

Ultimately we want the non-kinematic monopole to vanish in the heliocentric frame at the µK level and the dipole to vanish at one order of magnitude below the boost dipole, i.e., $\sim 0.1\,$mK. Solving the first equation (4.68) determines what the monopole temperature $\overline{T} = \overline{T}^{\rm LG}$ in the Local Group frame should be to achieve this based on our knowledge in the heliocentric frame. Thus, in the equations above the primed frame is the heliocentric frame and the unprimed the Local Group frame, i.e., we have

$$\left\{\overline{T}',\, \Delta T_d',\, \Theta_d,\, \beta\right\} = \left\{\overline{T}^{\rm hel},\, \Delta T_d^{\rm hel},\, \Theta_d^{\rm LG},\, \beta_{\rm hel-LG}\right\}. \tag{4.74}$$

$\overline{T}^{\mathrm{CMB}}$	$2.7255 \pm 0.0006\,\mathrm{K}$	Fixsen (2009) [22]
$\hat{\boldsymbol{d}}_{\mathrm{LG}}$	$(276.4°, 29.3°) \pm 3.2°$	Tully et al. (2008) [68]
$\hat{\boldsymbol{\beta}}_{\mathrm{hel-LG}}$	$(106°, -6°) \pm 4°$	Tully et al. (2008) [68]
$\hat{\boldsymbol{\beta}}_{\mathrm{hel-CMB}} = \hat{\boldsymbol{d}}_{\mathrm{hel}}$	$(264.14°, 48.26°) \pm 0.15°$	Fixsen et al. (1996) [24]
$c\beta_{\mathrm{hel-LG}}$	$318.6 \pm 20.0\,\mathrm{km\,s^{-1}}$	Tully et al. (2008) [68]
$c\beta_{\mathrm{hel-CMB}}$	$371 \pm 1\,\mathrm{km\,s^{-1}}$	Fixsen et al. (1996) [24]

The three angles can be determined from the literature whereas the unitless dipole Θ_d^{LG} is computed directly from the LTB or Szekeres model. Moreover $\hat{\boldsymbol{d}} \equiv \hat{\boldsymbol{d}}_{\mathrm{LG}}$, $\hat{\boldsymbol{d}}' \equiv \hat{\boldsymbol{d}}_{\mathrm{hel}}$ and $\hat{\boldsymbol{\beta}} \equiv \hat{\boldsymbol{\beta}}_{\mathrm{hel-LG}}$.

To simplify notation let $D \equiv \Delta T_d^{\mathrm{hel}}$ be the dipole in the heliocentric frame; subscripts '1' and '2' shall label each respective term above.

We now compute the non-kinematic dipole in the case of the LTB model. The monopole and dipole of (4.71) and (4.72) above are

$$\overline{T}_1^{\mathrm{hel}} = \overline{T}^{\mathrm{LG}} \left(1 - \frac{1}{6}\beta_{\mathrm{hel-LG}}^2 - \frac{1}{3}\Theta_d^{\mathrm{LG}}\beta_{\mathrm{hel-LG}}\cos\alpha_1\right) \tag{4.75a}$$

$$\overline{T}_2^{\mathrm{hel}} = \overline{T}^{\mathrm{CMB}}(1 - \frac{1}{6}\beta_{\mathrm{hel-CMB}}^2) \tag{4.75b}$$

$$D_1 = \overline{T}^{\mathrm{LG}} \left(\Theta_d^{\mathrm{LG}}\cos\alpha_3 + \beta_{\mathrm{hel-LG}}\cos\alpha_2\right) \tag{4.75c}$$

$$D_2 = \overline{T}^{\mathrm{CMB}}\beta_{\mathrm{hel-CMB}} \tag{4.75d}$$

As we want the monopoles to cancel at the µK level we solve $\overline{T}_1^{\mathrm{hel}} = \overline{T}_2^{\mathrm{hel}}$ for $\overline{T}^{\mathrm{LG}}$. We assume $\hat{\boldsymbol{d}}_{\mathrm{hel}} = \hat{\boldsymbol{\beta}}_{\mathrm{hel-CMB}}$, i.e., the measured dipole direction is the same as the direction given for the boost. The values we use are given in the table while we find from our model $\Theta_d^{\mathrm{LG}} = 2.070\,54 \times 10^{-3}$. (Note this gives a dipole temperature of $\approx 5.64\,\mathrm{mK}$.)

With these values we have

$$\begin{aligned}
\cos\alpha_1 &= \hat{\boldsymbol{\beta}}_{\mathrm{hel-LG}} \cdot \hat{\boldsymbol{d}}_{\mathrm{LG}} = -0.91 \pm 0.04 \\
\cos\alpha_2 &= \hat{\boldsymbol{\beta}}_{\mathrm{hel-LG}} \cdot \hat{\boldsymbol{d}}_{\mathrm{hel}} = -0.69 \pm 0.05 \\
\cos\alpha_3 &= \hat{\boldsymbol{d}}_{\mathrm{hel}} \cdot \hat{\boldsymbol{d}}_{\mathrm{LG}} = 0.933 \pm 0.020
\end{aligned}$$

In the heliocentric frame we find

$$\begin{aligned}
\overline{T}_1^{\mathrm{hel}} &= \overline{T}_2^{\mathrm{hel}} = 2.7255 \pm 0.0006\,\mathrm{K} \\
\overline{T}^{\mathrm{LG}} &= 2.7255 \pm 0.0006\,\mathrm{K} \\
D_1 &= 3.26 \pm 0.22\,\mathrm{mK} \\
D_2 &= 3.373 \pm 0.009\,\mathrm{mK}
\end{aligned}$$

With these values we find a non-kinematic dipole

$$\Delta D_{\mathrm{nk}} \equiv D_1 - D_2 = -0.12 \pm 0.22\,\mathrm{mK}. \tag{4.76}$$

As a check we use HEALPix-boost [173], a modified version of HEALPix that allows inclusion of modulation and aberration effects on CMB maps, to calculate $\Delta D_{\rm nk}$. Indeed, by this consistency check we find $\Delta D_{\rm nk} \equiv D_1 - D_2 = -0.11\,\mathrm{mK}$. The uncertainty on this value we can take to be the one quoted, which was computed by propagating the errors according to the dipole formula (4.69).

In the Szekeres model, for an observer located at $r_o = 25h^{-1}$ Mpc, we have $\Theta_d^{\rm LG} = 2.052\,96 \times 10^{-3}$. While we have only computed $\Delta D_{\rm nk}$ for the LTB model, we expect that the estimate from the Szekeres model would be very similar. This is because, in this analysis, we only require the magnitude of the dipole of the LTB or Szekeres models and *not* the quadrupole (as we argue in appendix C). In the case of the Szekeres model, the lack of axial symmetry of the observer's celestial sphere means the spherical harmonic decomposition of the sky will include contributions beyond just the zonal harmonics $Y_{\ell 0}$, unlike the spherically symmetric LTB models. However, the CMB seen by generic observers in both LTB and Szekeres models are dominated by a dipole, with the next largest fluctuation being the quadrupole, which is 3 orders of magnitude smaller than the dipole. Thus, in the above analysis a non-kinematic dipole cannot sufficiently distinguish between our LTB and Szekeres models, at least not at the level of precision required to cancel the monopole.

4.6 Aberration in the LTB model

As mentioned above the aberration effect causes a shift of the observed direction towards the direction of the boost $\boldsymbol{\beta}$, so a photon originally observed from $\hat{\boldsymbol{n}}$ now appears coming from $\hat{\boldsymbol{n}}' = \hat{\boldsymbol{n}}'(\hat{\boldsymbol{n}})$. The effect breaks the statistical isotropy of the unboosted sky, and implies that the 2-point correlation function $C(\hat{\boldsymbol{n}}_1, \hat{\boldsymbol{n}}_2)$ will no longer depend on just the relative separation of $\hat{\boldsymbol{n}}_1$ and $\hat{\boldsymbol{n}}_2$.

Let us begin by reviewing the aberration effect of a boost. The temperature $T'(\hat{\boldsymbol{n}}')$ measured in a boosted frame is related to the temperature $T(\hat{\boldsymbol{n}})$ in the unboosted frame by

$$T'(\hat{\boldsymbol{n}}') = \frac{T(\hat{\boldsymbol{n}})}{\gamma(1 - \boldsymbol{\beta}\cdot\hat{\boldsymbol{n}}')}. \tag{4.77}$$

We wish to rewrite $T(\hat{\boldsymbol{n}})$ as a function of $\hat{\boldsymbol{n}}'$ by expanding $\hat{\boldsymbol{n}} = \hat{\boldsymbol{n}}(\hat{\boldsymbol{n}}')$ in powers of β. Assuming the boost is small we have

$$\begin{aligned}\hat{\boldsymbol{n}} &= \frac{\hat{\boldsymbol{n}}' - [\gamma\beta + (\gamma-1)\hat{\boldsymbol{\beta}}\cdot\hat{\boldsymbol{n}}']\hat{\boldsymbol{\beta}}}{\gamma(1 - \boldsymbol{\beta}\cdot\hat{\boldsymbol{n}}')} \\ &\simeq \hat{\boldsymbol{n}}' - \boldsymbol{\beta} + \left(\hat{\boldsymbol{n}}'\cdot\boldsymbol{\beta}\right)\hat{\boldsymbol{n}}' = \hat{\boldsymbol{n}}' - \boldsymbol{\alpha}\end{aligned} \tag{4.78}$$

where

$$\boldsymbol{\alpha} := \boldsymbol{\beta} - (\hat{\boldsymbol{n}}'\cdot\boldsymbol{\beta})\hat{\boldsymbol{n}}' \simeq \hat{\boldsymbol{n}}' - \hat{\boldsymbol{n}}, \tag{4.79}$$

is responsible for the aberration effect. Note that $\boldsymbol{\alpha}$ is tangent to the sphere since $\hat{\boldsymbol{n}}' \cdot \boldsymbol{\alpha} = 0$. We can therefore think of $\boldsymbol{\alpha}$ as a vector field on the sphere that remaps observations on the sky. In the following we show how the aberration is degenerate with a curl-free deflection field from gravitational lensing.

It is a basic fact that any vector field $\boldsymbol{v}$ on the sphere can be decomposed as the sum of a curl-free vector field and a divergence-free vector field:

$$\boldsymbol{v} = \nabla\psi + \hat{\boldsymbol{n}} \times \nabla\chi, \tag{4.80}$$

where ψ and χ are scalar functions (or potentials) on the sphere that are determined up to an additive constant. Written in component form in terms of intrinsic coordinates on the sphere we have

$$v^A = \nabla^A\psi + \epsilon^{AB}\nabla_B\chi, \tag{4.81}$$

where $A, B \in \{1, 2\}$ label the coordinates, ∇_A is the covariant derivative on the unit sphere and ϵ_{AB} is the Levi-Civita symbol. We have the identities $\nabla \times \nabla\psi = 0$ (curl-free) and $\nabla \cdot (\hat{\boldsymbol{n}} \times \nabla\chi) = 0$ (divergence-free), and by taking either the divergence or curl of (4.80), the potentials can be recovered from the following equations

$$\nabla \cdot \boldsymbol{v} = \nabla^2\psi, \tag{4.82a}$$

$$\nabla \times \boldsymbol{v} = \nabla \times (\hat{\boldsymbol{n}}' \times \nabla\chi). \tag{4.82b}$$

In the context of a boost we set $\boldsymbol{v} = \boldsymbol{\alpha}$, then substitute into (4.82a) above to obtain the first equation

$$\nabla^2\psi = -\nabla \cdot [\big(\hat{\boldsymbol{n}}' \cdot \boldsymbol{\beta}\big)\ \hat{\boldsymbol{n}}']. \tag{4.83}$$

Let us focus on the "source term" on the right-hand side. Expanding the right-hand side we find

$$-\nabla \cdot [\big(\hat{\boldsymbol{n}}' \cdot \boldsymbol{\beta}\big)\ \hat{\boldsymbol{n}}'] = -\hat{\boldsymbol{n}}' \cdot \nabla(\hat{\boldsymbol{n}}' \cdot \boldsymbol{\beta}) - (\hat{\boldsymbol{n}}' \cdot \boldsymbol{\beta})\nabla \cdot \hat{\boldsymbol{n}}' = -2\,\hat{\boldsymbol{n}}' \cdot \boldsymbol{\beta}, \tag{4.84}$$

where in the second equality we have used $\nabla \cdot \hat{\boldsymbol{n}}' = 2$ with

$$\nabla \equiv e_{\hat{\theta}}\,\partial_\theta + e_{\hat{\phi}}\,\frac{1}{\sin\theta}\partial_\phi, \tag{4.85}$$

being the gradient operator on the unit sphere. Here $e_{\hat{\theta}}$ and $e_{\hat{\phi}}$ form a local orthonormal basis and are tangent to lines of longitude and latitude respectively. Thus, we see that the right-hand side of (4.83) is a pure dipole (c.f. (4.24b)) so when expanded in spherical harmonics the only non-zero[5] $a_{\ell m}$ are those with $\ell = 1$:

$$-2\,\hat{\boldsymbol{n}}' \cdot \boldsymbol{\beta} = -2\sum_{m=-1}^{1} a_{1m}Y_{1m} = \sum_{m=-1}^{1} a_{1m}(-2Y_{1m}). \tag{4.86}$$

[5]Recall that the decomposition into spherical harmonics is unique.

Noting the following property of spherical harmonics

$$\nabla^2 Y_{\ell m} = -\ell(\ell+1) Y_{\ell m}, \tag{4.87}$$

we have

$$\sum_m a_{1m}(-2Y_{1m}) = \sum_m a_{1m}\nabla^2 Y_{1m} = \nabla^2 \sum_m a_{1m} Y_{1m} = \nabla^2 \left(\hat{\boldsymbol{n}}' \cdot \boldsymbol{\beta}\right). \tag{4.88}$$

Referring back to (4.83) we have shown $\nabla^2\psi = \nabla^2(\hat{\boldsymbol{n}}' \cdot \boldsymbol{\beta})$, from which it is easy to see that

$$\psi = \hat{\boldsymbol{n}}' \cdot \boldsymbol{\beta} + \text{constant}. \tag{4.89}$$

The constant, or monopole arises because the kernel of the operator ∇^2 is degenerate with a monopole, that is, constant functions are solutions to $\nabla^2 f = 0$. The potential ψ is, therefore, not observable while the aberration field $\boldsymbol{\alpha}$ is.

Next we determine the divergence-free vector field or equivalently the function $\chi = \chi(\theta, \phi)$ from (4.82b). Again, without loss of generality, we let the boost be directed along the z-axis so that the aberration is azimuthally symmetric, i.e., it is independent of ϕ.

Observe that

$$\boldsymbol{\alpha} \cdot \boldsymbol{\alpha} = \left(\boldsymbol{\beta} - (\hat{\boldsymbol{n}}' \cdot \boldsymbol{\beta})\,\hat{\boldsymbol{n}}'\right)^2 = \beta^2(1 - \cos^2\theta') = \beta^2 \sin^2\theta'. \tag{4.90}$$

From the azimuthal symmetry we deduce $\boldsymbol{\alpha} = -\beta \sin\theta'\, \hat{\boldsymbol{e}}_\theta$, where the minus sign appears because the deflection is towards the direction of the boost. However, we have $-\beta \sin\theta'\, \hat{\boldsymbol{e}}_\theta = \nabla(\hat{\boldsymbol{n}}' \cdot \boldsymbol{\beta}) = \nabla\psi$, which implies that $\hat{\boldsymbol{n}}' \times \nabla\chi = 0$ or $\chi = \text{constant}$. Hence

$$\boldsymbol{\alpha} = \nabla(\hat{\boldsymbol{n}}' \cdot \boldsymbol{\beta}), \tag{4.91}$$

meaning that, physically, the aberration effect does not induce any curl modes on the CMB beyond what is already present. We have therefore shown the aberrating field $\boldsymbol{\alpha}$ amounts to a curl-free vector field:

$$\hat{\boldsymbol{n}}' - \hat{\boldsymbol{n}} \simeq \nabla\left(\hat{\boldsymbol{n}}' \cdot \boldsymbol{\beta}\right). \tag{4.92}$$

The aberration is a purely kinematic effect, but is in fact very similar to the deflection caused by gravitational lensing, in this case, of a foreground structure. The lensing convergence [174], κ, is defined by

$$\kappa(\hat{\boldsymbol{n}}) \equiv \frac{1}{2}\nabla \cdot \boldsymbol{\alpha}. \tag{4.93}$$

The convergence is unique only up to a constant (or monopole), but this is often set to zero as we do here. In the case of a boost we have

$$\kappa = \frac{1}{2}\nabla \cdot \boldsymbol{\alpha} = \frac{1}{2}\nabla^2(\hat{\boldsymbol{n}}' \cdot \boldsymbol{\beta}) = -\hat{\boldsymbol{n}}' \cdot \boldsymbol{\beta}. \tag{4.94}$$

where we again used (4.87). Thus we expect $\kappa \sim 10^{-3}$ in the heliocentric frame.

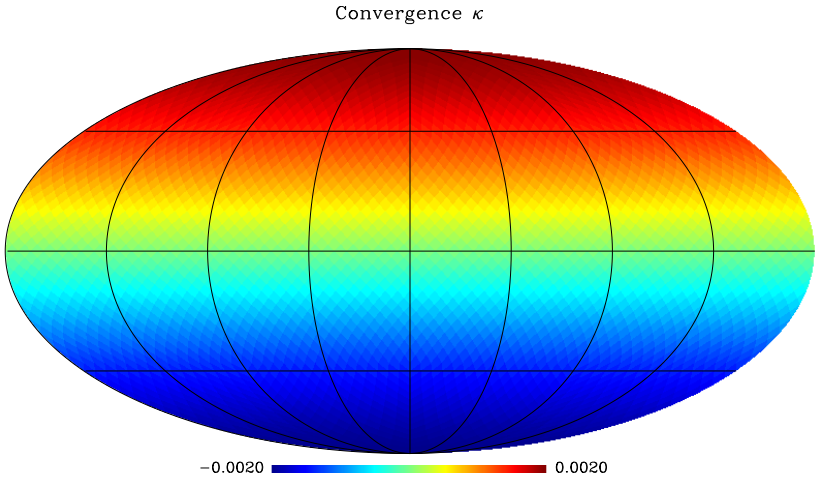

Figure 4.11: Map of the convergence for an off-centre observer located at $r_o = 28h^{-1}$ Mpc in the LTB model. Here we use $N_{\text{side}} = 16$. Note dipolar axis has been rotated onto the z-axis and the monopole has been subtracted.

4.6.1 Estimating the deflection

In order to quantify to what extent a local void can mimic the aberration effect of a local Lorentz boost we compute the convergence in the LTB model. As there is no explicit expression for the convergence for an LTB spacetime, we resort to numerical integration of the geodesic deviation equations, or the related Sachs optical equations [174].

We recall the Sachs optical equations are a set of coupled equations describing the effects of geometry (and thus matter) on a light beam. Here we will only need the equation

$$\frac{\mathrm{d}\hat{\theta}}{\mathrm{d}\lambda} + \hat{\theta}^2 + \hat{\sigma}^2 = -\frac{1}{2}\mathcal{R}_{\mu\nu}k^\mu k^\nu, \tag{4.95}$$

where $\hat{\theta} \equiv \frac{1}{2}\nabla_\mu k^\mu$ and $\hat{\sigma}^2 \equiv \frac{1}{2}\nabla_\mu k_\nu \nabla^\mu k^\nu - \hat{\theta}^2$ are the null expansion and shear scalars respectively. This equation can be recast in terms of the angular diameter distance D_A, by noting the relation

$$\hat{\theta} = \frac{\mathrm{d}}{\mathrm{d}\lambda}\ln D_A. \tag{4.96}$$

Thus (4.95) becomes

$$\frac{\mathrm{d}^2 D_A}{\mathrm{d}\lambda^2} + \left(\hat{\sigma}^2 + \frac{1}{2}\mathcal{R}_{\mu\nu}k^\mu k^\nu\right) D_A = 0. \tag{4.97}$$

The shear term, $\hat{\sigma}^2$, is associated with the Weyl curvature and its effect on a geodesic beam is subdominant to the Ricci term in our models. We therefore neglect it in the following and work in the Ricci focusing regime. (See [175] for justification.) Observe that (4.95) and (4.97) are purely geometrical equations. They can be related to the matter content by inserting Einstein's equations as

$$\mathcal{R}_{\mu\nu} = 8\pi\left(T_{\mu\nu} - \frac{1}{2}T g_{\mu\nu}\right) - \Lambda g_{\mu\nu} = 8\pi\rho\left(u_\mu u_\nu + \frac{1}{2}g_{\mu\nu}\right) - \Lambda g_{\mu\nu} \tag{4.98}$$

where $T = T_{\mu\nu}\, g^{\mu\nu}$ and $u_\mu = \delta_{\mu t}$ in comoving coordinates. Twice contracting (4.98) with the null tangent vector, (4.95) becomes

$$\frac{\mathrm{d}^2 D_A}{\mathrm{d}\lambda^2} + 4\pi\rho (k^t)^2 D_A = 0, \tag{4.99}$$

which we solve simultaneously with the null geodesic equations. We remark that, although Λ vanishes, the effect of Λ still persists through ρ, whose evolution depends on it by (3.5). Although the type of structures under study are in the nonlinear density regime, the size of the deflection angle α is small (arc minutes) [176]. We are therefore justified in working in the *weak lensing regime* [125], in which we are able to refer to an unlensed ray—the direction the ray would be measured at, in the absence of the void.

In the weak lensing regime, the main object of interest is the amplification matrix,

$$A = \begin{pmatrix} 1-\kappa-\gamma_1 & \gamma_2-\omega \\ \gamma_2+\omega & 1-\kappa+\gamma_1 \end{pmatrix}, \tag{4.100}$$

and all lensing effects are described by the convergence (as above), γ_1 and γ_2, the shear and ω, the vorticity. These lensing variables are related to the optical scalars $\hat{\theta}$ and $\hat{\sigma}$ while observable quantities are related to invariants of the matrix (e.g. trace, eigenvalues, determinant etc). Here we will only be interested in the magnification, which is given by

$$\mu = \frac{\overline{D}_A^2}{D_A^2} = (\det A)^{-1} = \left[(1-\kappa)^2 + \gamma^2\right]^{-1}, \tag{4.101}$$

where $\overline{D}_A$ is the angular diameter distance of the FLRW background. In the case of the LTB model under study, the convergence and shear are small,[6] (i.e. $|\kappa| \ll 1$ and $\gamma_1^2 + \gamma_2^2 \ll 1$) so we can relate the angular diameter distance to the convergence to leading order:

$$\mu = \frac{\overline{D}_A^2}{D_A^2} \simeq 1 + 2\kappa \implies \kappa \simeq \frac{1}{2}(\mu - 1). \tag{4.102}$$

Following [176] we take the angular diameter distance of the FLRW background to be

$$\overline{D}_A^2 = a^2(t)(r^2 + r_o^2 - 2\, r r_o \cos\vartheta), \tag{4.103}$$

for an off-centre observer at $r = r_o$, $\vartheta = 0$ and $\varphi = \pi/2$. This formula reduces to the familiar expression, $\overline{D}_A = a(t)r$, by centring the coordinates at the position of the observer, rather than the would-be void's centre. (It can also be shown to solve (4.99) with $\rho = \overline{\rho}$ and $k^t = a^{-1}$.) The comoving coordinate r in (4.103) is set to the radial distance reached by the beam in the LTB spacetime and computed using the null geodesic equations. Each light beam is integrated backwards, starting from the observer and terminating when the elapsed time has reached $400\,\mathrm{Mpc}/c$. The convergence is shown as a map in fig. 4.11. As can be seen in (4.94), the convergence has a dipole structure, much like a boost, and further, κ_{10} matches the corresponding boost value well (see fig. 4.12).

[6] This is more often the case than not (see §1.5 of [125]).

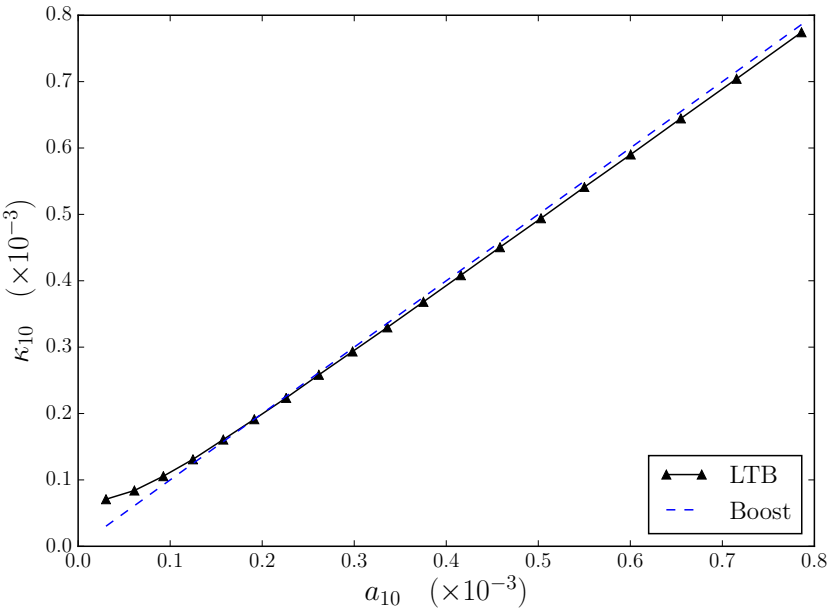

Figure 4.12: Plot of the convergence coefficient κ_{10} as a_{10} is varied by increasing the density contrast parameter δ_0 (each marker represents a different δ_0 with underdense values toward the right). Here the observer is placed at a distance $r_o = 5h^{-1}$ Mpc. For reference we show the boost prediction, $\kappa_{10} = \beta \cdot \hat{\boldsymbol{n}}$, as the dashed line. Note the slight rise of the LTB curve is due to numerical errors when our LTB model approaches the FLRW limit and should therefore be ignored.

4.7 Modulation in the LTB model

Having seen that the LTB model induces a deflection of the same order of magnitude as a local Lorentz boost, we now turn our attention to whether a modulation effect is present for an off-centre observer.

Recall the observed CMB for an observer boosted relative to the CMB rest frame with boost vector $\boldsymbol{\beta}$, is given by (1.17), with $1 + \boldsymbol{\beta} \cdot \hat{\boldsymbol{n}}$ representing the modulation and $\hat{\boldsymbol{n}}$ the direction of observation in the boosted frame. Notice for the hemisphere in which $\boldsymbol{\beta}$ points $1 + \boldsymbol{\beta} \cdot \hat{\boldsymbol{n}} > 1$ while on the opposite hemisphere $1 + \boldsymbol{\beta} \cdot \hat{\boldsymbol{n}} < 1$. Since $\beta \sim 10^{-3}$ the effect on the primordial fluctuations, $\delta T(\hat{\boldsymbol{n}}) \sim 10^{-5}$ K, induces a modulation at the level of

$$(1 + \boldsymbol{\beta} \cdot \hat{\boldsymbol{n}})\, \delta T - \delta T \sim 10^{-8}\,\mathrm{K}. \tag{4.104}$$

The modulation serves to break the statistical isotropy of the primordial fluctuations and induce a power asymmetry on the sky. The modulation effect is closely related to the empirical dipole modulation [177], $1 + \boldsymbol{A} \cdot \hat{\boldsymbol{n}}$, used to explain the observed power asymmetry. However, the modulation given by a boost, $1 + \boldsymbol{\beta} \cdot \hat{\boldsymbol{n}}$, is only degenerate with the empirical modulation at linear order.

The difficulty in constructing a modulation for our LTB model comes from the fact that we require a reference sky on which the modulation acts. In the case of a boost

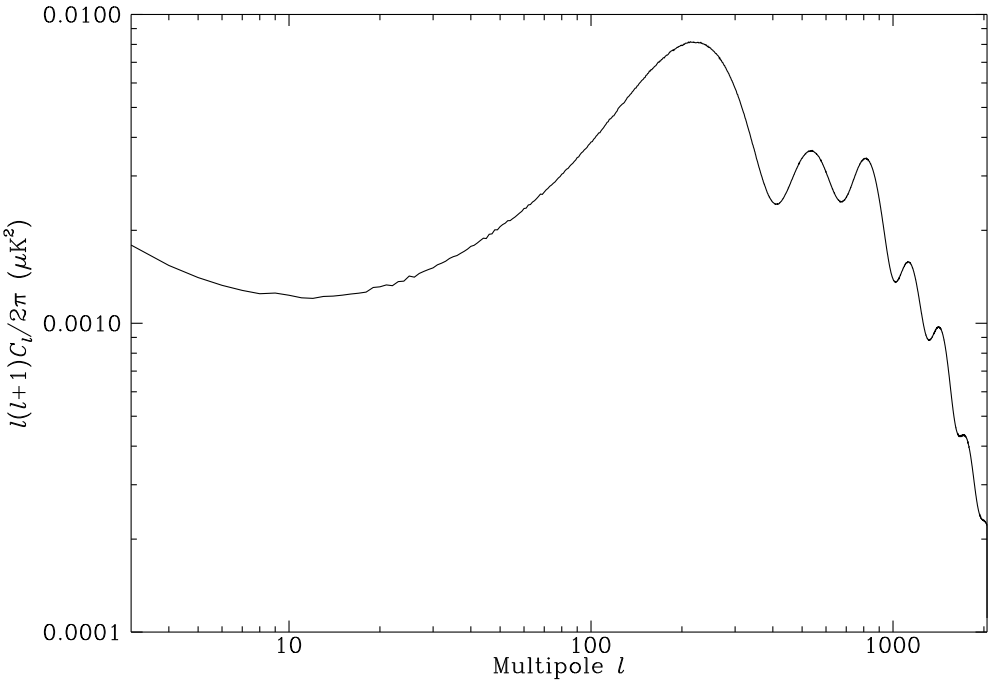

Figure 4.13: Residual power spectrum of a modulated and unmodulated temperature map. The temperature maps are generated as Gaussian realisations of the *Planck* best-fit power spectrum. Shown is the average over 1000 realisations.

this is simply the CMB observed in the CMB rest frame. By deboosting to the CMB rest frame we 'undo' the induced dipole (as well as other small contributions to higher multipoles). While an off-centre observer will see a large dipole, this is not due to the "peculiar motion" but rather that photons traversing the void are redshifted by different amounts depending on the trajectory taken.

The underlying (or unmodulated) CMB will be chosen in the following way. We first assume a reference FLRW model, which we take to be the *Planck* 2013 ΛCDM model (see (4.9)) and denote by $\overline{T}_o(\hat{\boldsymbol{n}})$ the temperature of the unmodulated sky seen by a generic observer in this model. Because of spatial homogeneity and isotropy the intersection of the observer's past light cone and the last scattering surface (which we assume to be a $t = t_{\rm lss} = \text{const}$ hypersurface) forms a sphere. We assume the CMB anisotropies are generated on the surface of last scattering. We denote by $\overline{z}_{\rm lss} = \text{const}$ the redshift to this surface. Assuming the CMB anisotropies are laid down on this surface then

$$\frac{T_{\rm lss}(\hat{\boldsymbol{n}})}{\overline{T}_o(\hat{\boldsymbol{n}})} = 1 + \overline{z}_{\rm lss}, \tag{4.105}$$

where $T_{\rm lss}(\hat{\boldsymbol{n}})$ is the temperature of the CMB blackbody at the time of last scattering.

Since in our LTB model there are no decaying modes (as we chose $t_b(r) = \text{const}$), the universe becomes more spatially homogeneous further back in time. At a redshift of

$\overline{z}_{\rm lss} \simeq 1100$ we identify the last scattering surface with the last scattering surface in the reference FLRW model. The temperature at last scattering in both models will then be $T_{\rm lss}(\hat{\boldsymbol{n}})$. We denote by $T_o(\hat{\boldsymbol{n}})$ the temperature observed by an off-centre observer at time t_0 and $z(\hat{\boldsymbol{n}})$ the redshift determined by propagating the null geodesic, according to the LTB model, in the direction $\hat{\boldsymbol{n}}$ back to $t = t_{\rm lss}$ from an observer who receives the photon at $t = t_0$. In the LTB model we thus have

$$\frac{T_{\rm lss}(\hat{\boldsymbol{n}})}{T_o(\hat{\boldsymbol{n}})} = 1 + z(\hat{\boldsymbol{n}}). \tag{4.106}$$

Note we have not taken into account the bending of photon trajectories as we expect such deflections are small in view of the previous section (§4.6). Thus we simply identify a point $\hat{\boldsymbol{n}} = \hat{\boldsymbol{n}}(\theta, \phi)$ on the last scattering sphere with a point $\hat{\boldsymbol{n}} = \hat{\boldsymbol{n}}(\theta, \phi)$ on the observer's celestial sphere allowing us to isolate the modulation from lensing effects. We remark we can always ensure the deflection is small by placing the observer closer to the origin; at the centre we have no deflection since trajectories are radial on account of the spherical symmetry of the model. With this assumption we find

$$\frac{T_{\rm lss}(\hat{\boldsymbol{n}})}{T_o(\hat{\boldsymbol{n}})} = 1 + z(\hat{\boldsymbol{n}}) \iff \frac{\overline{T}_o(\hat{\boldsymbol{n}})\,(1 + \overline{z}_{\rm lss})}{T_o(\hat{\boldsymbol{n}})} = 1 + z(\hat{\boldsymbol{n}}), \tag{4.107}$$

and therefore

$$T_o(\hat{\boldsymbol{n}}) = \overline{T}_o(\hat{\boldsymbol{n}}) \left[\frac{1 + \overline{z}_{\rm lss}}{1 + z(\hat{\boldsymbol{n}})}\right] = g(\hat{\boldsymbol{n}})\,\overline{T}_o(\hat{\boldsymbol{n}}), \tag{4.108}$$

where

$$g(\hat{\boldsymbol{n}}) \equiv \frac{1 + \overline{z}_{\rm lss}}{1 + z(\hat{\boldsymbol{n}})}. \tag{4.109}$$

In the nonlinear regime we do not have an analytic form for $g(\hat{\boldsymbol{n}})$, but we can, however, analyse its limiting behaviour by checking that it reduces to familiar expressions in the linear regime. As we will see this term is analogous to the modulation factor $1 + \boldsymbol{\beta} \cdot \hat{\boldsymbol{n}}$.

We recall the redshift (2.56) from linear theory, which we rewrite in terms of $\hat{\boldsymbol{n}}$ as

$$\frac{1}{1 + z(\hat{\boldsymbol{n}})} = \frac{a(t_{\rm lss})}{a(t_0)} \left\{1 - \left[\boldsymbol{\beta} \cdot (-\hat{\boldsymbol{n}}) + \Phi\right]_{t_{\rm lss}}^{t_0} + I(\hat{\boldsymbol{n}})\right\}, \tag{4.110}$$

where I is the ISW term with the integral taken over the line of sight (hence the $\hat{\boldsymbol{n}}$ dependence). Clearly such terms vanish in the FLRW limit, however, more subtle is the peculiar velocity $\boldsymbol{v} = c\boldsymbol{\beta}$, which depends on the density field through

$$\boldsymbol{v}(t, \boldsymbol{r}) = \frac{a(t) f(t) H}{4\pi} \int \delta(\boldsymbol{r}') \frac{\boldsymbol{r} - \boldsymbol{r}'}{|\boldsymbol{r} - \boldsymbol{r}'|^3}\, \mathrm{d}^3\boldsymbol{r}'. \tag{4.111}$$

It is clear $\boldsymbol{v} \to 0$ as $\delta \to 0$, from which it follows $g \to 1$ in the homogeneous limit.

In the background we have $a(t_0)/a(t_{\rm lss}) = 1 + \overline{z}_{\rm lss}$ so (4.110) may be rewritten

$$\frac{1 + \overline{z}_{\rm lss}}{1 + z(\hat{\boldsymbol{n}})} = 1 + \boldsymbol{\beta} \cdot \hat{\boldsymbol{n}} + \ldots. \tag{4.112}$$

Here we have assumed that at last scattering $\boldsymbol{\beta}\cdot\hat{\boldsymbol{n}}$ is zero (or negligible) and we omitted the other terms since they are at least two orders or magnitude smaller than the kinematic term. Clearly the right-hand side of (4.112) is just the Lorentz boost to linear order:

$$\frac{1}{\gamma(1-\boldsymbol{\beta}\cdot\hat{\boldsymbol{n}})} = 1+\boldsymbol{\beta}\cdot\hat{\boldsymbol{n}}+\ldots. \tag{4.113}$$

Thus, in the linear regime, $g(\hat{\boldsymbol{n}})$ reduces to the linear modulation

$$g(\hat{\boldsymbol{n}}) \simeq 1+\boldsymbol{\beta}\cdot\hat{\boldsymbol{n}}. \tag{4.114}$$

In fig. 4.13 we illustrate the power modulation induced by our model void on a fiducial *Planck* best-fit power spectrum.[7]

4.7.1 Multipole couplings induced by $g(\hat{\boldsymbol{n}})$

Although we do not have an analytic form for $g(\hat{\boldsymbol{n}})$ we can still estimate the effect on the power spectrum. Like the a boost, the modulation $g(\hat{\boldsymbol{n}})$ also induces couplings between multipoles, which we make explicit below.

As usual, we expand the temperatures in spherical harmonics:

$$T_o(\hat{\boldsymbol{n}}) = \sum_{\ell m} a_{\ell m} Y_{\ell m}(\hat{\boldsymbol{n}}) \quad \text{and} \quad \overline{T}_o(\hat{\boldsymbol{n}}) = \sum_{\ell m} \overline{a}_{\ell m} Y_{\ell m}(\hat{\boldsymbol{n}}), \tag{4.115}$$

but now

$$\begin{aligned} a_{\ell m} &= \int \mathrm{d}\hat{\boldsymbol{n}}\, T_o(\hat{\boldsymbol{n}})\, Y^*_{\ell m}(\hat{\boldsymbol{n}}) = \int \mathrm{d}\hat{\boldsymbol{n}}\, g(\hat{\boldsymbol{n}}) \overline{T}_o(\hat{\boldsymbol{n}})\, Y^*_{\ell m}(\hat{\boldsymbol{n}}) \\ &= \sum_{\ell' m'} \overline{a}_{\ell' m'} \int \mathrm{d}\hat{\boldsymbol{n}}\, g(\hat{\boldsymbol{n}})\, Y_{\ell' m'}(\hat{\boldsymbol{n}})\, Y^*_{\ell m}(\hat{\boldsymbol{n}}) \\ &= \sum_{\ell' m'} \mathcal{A}_{\ell' m' \ell m}\, \overline{a}_{\ell' m'} \end{aligned} \tag{4.116}$$

and in the last line we define the mode coupling matrix

$$\mathcal{A}_{\ell' m' \ell m} \equiv \int \mathrm{d}\hat{\boldsymbol{n}}\, g(\hat{\boldsymbol{n}})\, Y_{\ell' m'}(\hat{\boldsymbol{n}})\, Y^*_{\ell m}(\hat{\boldsymbol{n}}), \tag{4.117}$$

in much the same way as for a boost [109]. The details of the coupling will depend on the details of the local void being studied and the difference between the LTB and Szekeres models will manifest in $\mathcal{A}_{\ell' m' \ell m}$. We remark that if $g = 1$ we recover the orthogonality relation:

$$\mathcal{A}_{\ell' m' \ell m} = \delta_{\ell \ell'} \delta_{m m'}, \tag{4.118}$$

so that $a_{\ell m} = \overline{a}_{\ell m}$ (no coupling).

[7] See `http://pla.esac.esa.int/pla/`.

Without loss of generality we align $g(\hat{\boldsymbol{n}})$ with the observer's z-axis so that we only need to consider the zonal modes $g_{\ell 0}$. Thus with

$$g(\hat{\boldsymbol{n}}) = \sum_{\ell 0} g_{\ell 0}\, Y_{\ell 0}(\hat{\boldsymbol{n}}), \tag{4.119}$$

equation (4.117) becomes

$$\begin{aligned}\mathcal{A}_{\ell_1 m_1 \ell_2 m_2} &= \sum_{\ell} g_{\ell 0} \int \mathrm{d}\hat{\boldsymbol{n}}\, Y_{\ell 0}(\hat{\boldsymbol{n}})\, Y_{\ell_1 m_1}(\hat{\boldsymbol{n}})\, Y^*_{\ell_2 m_2}(\hat{\boldsymbol{n}}) \\ &= \sum_{\ell} g_{\ell 0} \sqrt{\frac{(2\ell+1)(2\ell_1+1)(2\ell_2+1)}{4\pi}} \\ &\qquad \times (-1)^{m_2} \begin{pmatrix} \ell_1 & \ell_2 & \ell \\ 0 & 0 & 0 \end{pmatrix} \begin{pmatrix} \ell_1 & \ell_2 & \ell \\ m_1 & -m_2 & 0 \end{pmatrix},\end{aligned} \tag{4.120}$$

where $\begin{pmatrix} \ell_1 & \ell_2 & \ell_3 \\ m_1 & m_2 & m_3 \end{pmatrix}$ is the Wigner 3j symbol (see Appendix D). The Wigner 3j symbols have several useful properties but for now it suffices to say they are non-zero if both

$$m_1 + m_2 + m_3 = 0, \tag{4.121}$$

and the triangle inequality,

$$|\ell_1 - \ell_2| \leq \ell_3 \leq \ell_1 + \ell_2, \tag{4.122}$$

are satisfied. By (4.121) we must have $m_1 = m_2$ for the Wigner 3j symbol to be non-zero. In addition we also have the property that if $\begin{pmatrix} \ell_1 & \ell_2 & \ell \\ 0 & 0 & 0 \end{pmatrix}$ is non-zero then $\ell_1 + \ell_2 + \ell$ is even. This result comes from the fact that the Wigner 3j symbol picks up a factor $(-1)^{\ell_1+\ell_2+\ell_3}$ on odd permutations of its columns.

Using these properties of the Wigner 3j symbols, we can show how the multipole couplings affect the power spectrum. Note the following are standard results for when $g(\hat{\boldsymbol{n}}) = 1 + \boldsymbol{\beta}\cdot\hat{\boldsymbol{n}}$. However, in the case of our LTB model we do not have an analytic form for $g(\hat{\boldsymbol{n}})$.

Consider

$$\left\langle a_{\ell_1 m_2} a^*_{\ell_2 m_2} \right\rangle = \sum_{\ell_1' m_1'} \sum_{\ell_2' m_2'} \mathcal{A}_{\ell_1' m_1' \ell_1 m_1}\, \mathcal{A}^*_{\ell_2' m_2' \ell_2 m_2} \left\langle \overline{a}_{\ell_1' m_1'} \overline{a}^*_{\ell_2' m_2'} \right\rangle, \tag{4.123}$$

We remind the reader angle brackets without 'Ω' denote the ensemble average. Given that we only need to consider the zonal modes $g_{\ell 0}$ we see from (4.120) that the coupling matrix must also be real: $\mathcal{A}^*_{\ell_1' m_1' \ell_1 m_1} = \mathcal{A}_{\ell_1' m_1' \ell_1 m_1}$. Assuming the underlying, unmodulated power spectrum, $\overline{C}_\ell$, is statistically isotropic (i.e. $\langle \overline{a}_{\ell_1' m_1'} \overline{a}^*_{\ell_2' m_2'} \rangle = \overline{C}_{\ell_1'} \delta_{\ell_1' \ell_2'}\, \delta_{m_1' m_2'}$), we find

$$\begin{aligned}\left\langle a_{\ell_1 m_2} a^*_{\ell_2 m_2} \right\rangle &= \sum_{\ell_1' m_1'} \sum_{\ell_2' m_2'} \mathcal{A}_{\ell_1' m_1' \ell_1 m_1}\, \mathcal{A}_{\ell_2' m_2' \ell_2 m_2}\, \overline{C}_{\ell_1'}\, \delta_{\ell_1' \ell_2'}\, \delta_{m_1' m_2'} \\ &= \sum_{\ell_1' m_1'} \mathcal{A}_{\ell_1' m_1' \ell_1 m_1}\, \mathcal{A}_{\ell_1' m_1' \ell_2 m_2}\, \overline{C}_{\ell_1'}\end{aligned} \tag{4.124}$$

Applying the selection rule (4.121), the first and second coupling matrices are non-vanishing when $m_1' = m_1$ and $m_1' = m_2$ respectively. Thus

$$\begin{aligned}\left\langle a_{\ell_1 m_2} a^*_{\ell_2 m_2} \right\rangle &= \sum_{\ell_1'} \mathcal{A}_{\ell_1' m_1 \ell_1 m_1}\, \mathcal{A}_{\ell_1' m_1 \ell_2 m_2}\, \overline{C}_{\ell_1'} \\ &= \delta_{m_1 m_2} \sum_{\ell_1'} \mathcal{A}_{\ell_1' m_1 \ell_1 m_1}\, \mathcal{A}_{\ell_1' m_1 \ell_2 m_1}\, \overline{C}_{\ell_1'} \end{aligned} \tag{4.125}$$

It is clear from the last line that $\langle a_{\ell_1 m_2} a^*_{\ell_2 m_2} \rangle$ is a linear combination of the $\overline{C}_\ell$ and therefore need not vanish for $\ell_1 \neq \ell_2$. The axial symmetry of an off-centre observer manifests in the Kronecker delta $\delta_{m_1 m_2}$. No such simplification will occur for a generic Szekeres observer since in general $g_{\ell m} \neq 0$ for $m \neq 0$ implying that $\left\langle a_{\ell_1 m_2} a^*_{\ell_2 m_2} \right\rangle \neq 0$ for $m_1 \neq m_2$.

In the LTB model we find

$$\begin{aligned} g_{00} &= 3.545 \\ g_{10} &= 4.238 \times 10^{-3} \\ g_{20} &= 4.390 \times 10^{-6} \end{aligned}$$

with contributions from higher ℓ multipoles increasingly small. Thus $g(\hat{\boldsymbol{n}})$ has a similar multipole structure to the CMB anisotropy (4.43). This is not surprising given $g(\hat{\boldsymbol{n}}) \propto (1+z)^{-1} \sim \Delta T/T$ (see (4.17)). The multipole structure of $g(\hat{\boldsymbol{n}})$ is that of a dominant dipole, with a small quadrupole moment that may be dropped.[8] Thus

$$\begin{aligned} g(\hat{\boldsymbol{n}}) &\approx g_{00}\, Y_{00} + g_{10}\, Y_{10} \\ &= \frac{1}{\sqrt{4\pi}}\, g_{00} + g_{10} \sqrt{\frac{3}{4\pi}}\, \cos\theta \\ &\approx 1 + g_{10} \sqrt{\frac{3}{4\pi}}\, \cos\theta \end{aligned} \tag{4.126}$$

where we have used $g_{00}/\sqrt{4\pi} = g_{00} Y_{00} = \left\langle g(\hat{\boldsymbol{n}}) \right\rangle_\Omega = 1.000026 \approx 1$. The last line can then be identified as a modulation effect.

Formulae for an (exact) modulation,

$$g(\hat{\boldsymbol{n}}) = (1 + \boldsymbol{A} \cdot \hat{\boldsymbol{n}}), \tag{4.127}$$

where $\boldsymbol{A}$ is some general direction on the sky (not necessarily the boost vector) are well known [178]. In the case of our model the coupling formula is

$$\left\langle a_{\ell m} a^*_{\ell+1 m} \right\rangle \approx g_{10}\, (\overline{C}_\ell + \overline{C}_{\ell+1}) \sqrt{\frac{(\ell - m + 1)(\ell + m + 1)}{(2\ell+3)(2\ell+1)}}. \tag{4.128}$$

As we can see a modulations couples the ℓ and $\ell + 1$ modes.

[8] The modulation, $1 + \boldsymbol{\beta} \cdot \hat{\boldsymbol{n}}$, also has corrections from the quadrupole if we keep terms of order β^2.

Chapter 5

Conclusion

The physical origin of the CMB dipole needs to be re-examined from the principles of general relativity. While a local Lorentz boost might be a natural candidate to explain the dipole, there is no *a priori* reason this has to be so. The recent work by Bolejko et al. [1] using exact cosmological models suggests a different picture to that of peculiar motion relative to a rigidly expanding FLRW background. Rather, the late epoch universe characterised by nonlinear structure formation, modelled using full general relativity, naturally gives rise to a notion of *differential expansion of space*. This feature is often overlooked in the standard framework but is a generic feature of exact inhomogeneous solutions of Einstein's equations. Nevertheless, it has immediate consequences beyond the Hubble expansion anisotropy that was studied in [1]. In particular, it points to a CMB dipole that is not caused entirely by a boost and thus has a non-kinematic component arising instead from the local expansion gradients. This was the conclusion that was reached in [1] and in this thesis we aimed to investigate the non-kinematic CMB dipole by computing the magnitude and characterising its associated effects.

In order to estimate the non-kinematic CMB dipole in the heliocentric frame, we derived to second order in β formulae for the monopole and dipole. These formulae allow us to circumvent the technical difficulty related to boosting maps in pixel space. As we mentioned in §4.5 this stems from the aberration effect on individual pixels and results in a map with pixels that are no longer equally spaced (and means the dipole cannot be computed in HEALPix).

Using these formulae we found a non-kinematic dipole of $\Delta D_{\rm nk} = -0.12 \pm 0.22\,\mathrm{mK}$. While this value is consistent with zero we note that this estimate is based on values of $\beta_{\rm Sun-LG}$ and $\hat{\boldsymbol{\beta}}_{\rm Sun-LG}$ derived from an using Newtonian velocity addition [68]. The uncertainties of $\beta_{\rm Sun-LG}$ and $\hat{\boldsymbol{\beta}}_{\rm Sun-LG}$ will need to be improved in the future as they are as yet too large for any precise determination of a non-zero non-kinematic dipole to be made. It is conceivable to construct a model in which $\boldsymbol{\beta}_{\rm Sun-LG}$ is known exactly and the non-kinematic dipole is non-vanishing. However, such an exercise amounts to fine tuning the boost velocity and the parameters of the LTB model.

As well as inducing a large dipole, a boost is associated with two other effects: (i) the aberration effect causing a lensing-like deflection on the CMB and (ii) a modulation of the primordial CMB anisotropies. At linear order in $\boldsymbol{\beta}$, a boost breaks statistical isotropy by inducing correlations among ℓ and $\ell \pm 1$ multipoles, as is well known [109,110]. These effects were detected by the *Planck* collaboration, who measured the boost velocity by analysing the multipole couplings that such effects induce. If the CMB dipole is induced by a local void then it must be able to reconcile these couplings with other physical processes.

In view of this, we have shown that an effect similar to the aberration effect of a local Lorentz boost is also present. This is not surprising given that the aberration is degenerate with the gravitational deflection from the lensing of structures. In the case of an off-centre observer in the LTB model the lensing is from a spherically symmetric foreground inhomogeneity. Since the off-centre observer sees a CMB sky that is axially symmetric about the axis defined by the radial line connecting the observer to the origin, the deflection field is also axially symmetric, and the convergence, κ, can be decomposed entirely in terms of the zonal harmonics, $Y_{\ell 0}(\hat{\boldsymbol{n}})$. Like a boost, the deflection field $\boldsymbol{\alpha}$ is a gradient of a scalar on account of the axial symmetry for an off-centre observer in the LTB model.

Assuming the deflection is small (a few arc seconds) the deflection can be treated in the weak lensing regime. In computing the convergence, κ, for the off-centre LTB observer, we require a reference FLRW model in order to define the magnification $\mu \equiv (\overline{D}_A/D_A)^2$, where $\overline{D}_A$ is the angular diamter distance of the reference model. This is taken to be the FLRW background in which the void is embedded.

The angular diameter distance for an observer in the background is then given by (4.103). This is equivalent to the more familiar $\overline{D}_A = a(t)r$, only now the coordinates are centred at the void's centre, hence the unconventional form. In the case of the Szekeres metric, while we can define spherical coordinates, r, θ, ϕ, there is no "origin" to speak of as in the LTB model. Consequently the angular diameter distance of the background cannot be defined in the same way. As such we have only computed the deflection in the LTB model. However, in the Szekeres model we expect the deflection field to contain both gradient and curl terms (c.f. (4.80)) due to the absence of axial symmetry for generic observers who do not lie on the axis of the density gradient.

We find the convergence is of the same order of magnitude as the convergence for a local Lorentz boost, i.e., $\kappa \sim 10^{-3}$. Indeed the dipole of the convergence is proportional to the dipole of CMB just as with a boost for which $k_{10} \sim \beta$ and $a_{10} \sim \beta$. While we have not computed how such a deflection impacts the full CMB temperature power spectrum, given the similarity of the deflection with the aberration of local boosts, we expect these effects to be highly degenerate with the boost interpretation.[1]

[1]Lensing effects generically break statistical isotropy of the CMB temperature (see the review [125]).

While the LTB metric is an exact solution, in the limit that the density contrasts are small ($|\delta_0| \ll 1$), the metric can be made to resemble the perturbed FLRW metric in the Newtonian gauge by making a suitable coordinate transformation [180–182]. Thus it should be no surprise that the LTB model is highly degenerate with perturbed FLRW models in this limit. (See for example fig. 4.8.) One can therefore 'decompose' the CMB anisotropy in the form of (2.58), identifying a peculiar velocity contribution, ISW contribution etc. The coordinate transformation can only be done in the linear regime so it is no surprise that this identification breaks down for nonlinear voids, such as those considered in this thesis.

Since the linearly perturbed FLRW model can always be mapped to an LTB model we expect the LTB model, even in the nonlinear regime, to also induce aberration and modulation effects, associated with the peculiar velocity term of (2.58). However the aberration effect has a different physical mechanism, namely lensing by the local void.

In §4.7 we made some tentative steps towards making explicit the modulation of the LTB model. This allows us to investigate the couplings between multipoles in the same way as for a boost. We demonstrated that local voids can also give rise to a modulation effect and that we recover the usual modulation, $1 + \boldsymbol{\beta} \cdot \hat{\boldsymbol{n}}$, in the limit the LTB model is in the linear regime.

Towards the end of this research, we became aware of a recently uploaded `arXiv` eprint by Cusin et al. [115], "*Are we living near the centre of a void?*", investigating the "geometrical origin" of the CMB dipole, that is, whether a local void can mimic the effects caused by a local Lorentz boost. Though they study a toy void model described by a Kottler metric embedded in a FLRW background, their analytic results show that lensing of the local void induces correlations among *all* multipoles,[2] a signature they say that distinguishes itself from a boost. This is an interesting development that deserves further research in the context of more realistic void models, such as the observationally constrained models used in this work.

In this work we have concentrated mainly on the simpler LTB model, but the fact there is no axial symmetry seen by generic observers in the Szekeres model would seem to suggest that there would be lensing and modulation effects not accounted for in spherically symmetric models such as the Kottler embedded FLRW model of [115] and generic LTB models. For the Szekeres model this could potentially show up in the structure of the off-diagonal correlations used in [115]. Moreover because of the lack of symmetry of Szekeres models, such effects, if present, will thus depend on the position of the observer in relation to the underdensity and neighbouring overdensity.

To date, Szekeres models have received little interest as models of cosmic structures. The additional free functions of the Szekeres solution allows much more realistic mod-

[2] Off-diagonal correlators can be constructed, that are non-vanishing when statistical isotropy is broken.

els. Indeed, more sophisticated Szekeres models have recently been developed [183] that advances the cosmic web picture of the universe. Cosmic structures have most typically been approximated as spherical using the LTB model. While this might be suitable for isolated structures it does not take into account expansion gradients that arise between structures such as voids and adjacent superclusters. How non-spherical structures affect the CMB has not been widely studied but in our view, when confronted with data, these models have a lot to offer.

Bibliography

[1] K. Bolejko, M. A. Nazer and D. L. Wiltshire, *Differential cosmic expansion and the Hubble flow anisotropy*, JCAP **06** (2016) 035, [arXiv:1512.07364].

[2] M. G. Aartsen *et al.* [IceCube Collaboration], *Observation of High-Energy Astrophysical Neutrinos in Three Years of IceCube Data*, Phys. Rev. Lett. **113** (2014) 101101, [arXiv:1405.5303].

[3] B. P. Abbott *et al.* [LIGO Scientific and Virgo Collaborations], *Observation of Gravitational Waves from a Binary Black Hole Merger*, Phys. Rev. Lett. **116** (2016) 061102, [arXiv:1602.03837].

[4] M. Visser, *Jerk and the cosmological equation of state*, Class. Quant. Grav. **21** (2004) 2603, [gr-qc/0309109].

[5] C. L. Bennett *et al.* [WMAP Collaboration], *Nine-Year Wilkinson Microwave Anisotropy Probe (WMAP) Observations: Final Maps and Results*, Astrophys. J. Suppl. **208** (2013) 20, [arXiv:1212.5225].

[6] P. A. R. Ade *et al.* [Planck Collaboration], *Planck 2013 results. XVI. Cosmological parameters*, Astron. Astrophys. **571** (2014) A16, [arXiv:1303.5076].

[7] J. T. Nielsen, A. Guffanti and S. Sarkar, *Marginal evidence for cosmic acceleration from Type Ia supernovae*, Sci. Rep. **6** (2016) 35596, [arXiv:1506.01354].

[8] T. Buchert, A. A. Coley, H. Kleinert, B. F. Roukema and D. L. Wiltshire, *Observational Challenges for the Standard FLRW Model*, Int. J. Mod. Phys. D **25** (2016) 1630007, [arXiv:1512.03313].

[9] R. H. Cyburt, B. D. Fields and K. A. Olive, *An Update on the big bang nucleosynthesis prediction for Li-7: The problem worsens*, JCAP **11** (2008) 012, [arXiv:0808.2818].

[10] R. H. Cyburt, J. Ellis, B. D. Fields, F. Luo, K. A. Olive and V. C. Spanos, *Gravitino Decays and the Cosmological Lithium Problem in Light of the LHC Higgs and Supersymmetry Searches*, JCAP **05** (2013) 014, [arXiv:1303.0574].

[11] C. Cattoën and M. Visser, *Cosmographic Hubble fits to the supernova data*, Phys. Rev. D **78** (2008) 063501, [arXiv:0809.0537].

[12] A. G. Riess *et al.* [Supernova Search Team Collaboration], *Observational evidence from supernovae for an accelerating universe and a cosmological constant*, Astron. J. **116** (1998) 1009, [astro-ph/9805201].

[13] S. Perlmutter *et al.* [Supernova Cosmology Project Collaboration], *Measurements of Omega and Lambda from 42 high redshift supernovae*, Astrophys. J. **517** (1999) 565, [astro-ph/9812133].

[14] G. Efstathiou, W. J. Sutherland and S. J. Maddox, *The cosmological constant and cold dark matter*, Nature **348** (1990) 705.

[15] M. Fukugita, F. Takahara, K. Yamashita and Y. Yoshii, *Test For The Cosmological Constant With The Number Count Of Faint Galaxies*, Astrophys. J. 361, L1-4.

[16] P. de Bernardis *et. al.* [Boomerang Collaboration], *A Flat universe from high resolution maps of the cosmic microwave background radiation*, Nature **404** (2000) 955, [astro-ph/0004404].

[17] G. W. Gibbons, Phantom matter and the cosmological constant, (2003) [arXiv:hep-th/0302199].

[18] T. Clifton, P. G. Ferreira, A. Padilla and C. Skordis, *Modified Gravity and Cosmology*, Phys. Rept. **513** (2012) 1, [arXiv:1106.2476].

[19] T. Buchert, *Dark Energy from Structure: A Status Report*, Gen. Rel. Grav. **40** (2008) 467, [arXiv:0707.2153].

[20] S. Sarkar, *Is the evidence for dark energy secure?*, Gen. Rel. Grav. **40** (2008) 269, [arXiv:0710.5307].

[21] S. Weinberg, *The Cosmological Constant Problem*, Rev. Mod. Phys. **61** (1989) 1.

[22] D. J. Fixsen, *The Temperature of the Cosmic Microwave Background*, Astrophys. J. **707** (2009) 916 [arXiv:0911.1955].

[23] V. Mukhanov, *Physical Foundations of Cosmology*, Cambridge University Press, Cambridge, 2005.

[24] D. J. Fixsen, E. S. Cheng, J. M. Gales, J. C. Mather, R. A. Shafer and E. L. Wright, *The Cosmic Microwave Background spectrum from the full COBE FIRAS data set*, Astrophys. J. **473** (1996) 576, [astro-ph/9605054].

[25] D. L. Wiltshire, *What is dust? - Physical foundations of the averaging problem in cosmology*, Class. Quant. Grav. **28** (2011) 164006, [arXiv:1106.1693].

[26] S. J. Aarseth, *Gravitational N-body simulations: tools and algorithms*, Cambridge University Press, Cambridge, 2003.

[27] J. E. Forero-Romero, Y. Hoffman, S. Gottloeber, A. Klypin and G. Yepes, *A Dynamical Classification of the Cosmic Web*, Mon. Not. Roy. Astron. Soc. **396** (2009) 1815, [arXiv:0809.4135].

[28] J. Einasto, *Yakov Zeldovich and the Cosmic Web Paradigm*, in R. van de Weygaert, S. Shandarin, E. Saar, J. Einasto (eds.), Proc. IAU Symp. **308** (Cambridge Univ. Press, 2017) in press, [arXiv:1410.6932].

[29] D. C. Pan, M. S. Vogeley, F. Hoyle, Y. Y. Choi and C. Park, *Cosmic Voids in Sloan Digital Sky Survey Data Release 7*, Mon. Not. Roy. Astron. Soc. **421** (2012) 926, [arXiv:1103.4156].

[30] P. J. E. Peebles, *The void phenomenon*, Astrophys. J. **557** (2001) 495 [arXiv:astro-ph/0101127].

[31] P. J. E. Peebles and A. Nusser, *Clues from nearby galaxies to a better theory of cosmic evolution*, Nature **465** (2010) 565 [arXiv:1001.1484].

[32] Y. C. Cai, N. Padilla and B. Li, *Testing Gravity using Cosmic Voids*, Mon. Not. Roy. Astron. Soc. **451** (2015) 1036, [arXiv:1410.1510].

[33] J. Clampitt and B. Jain, *Lensing Measurements of the Mass Distribution in SDSS Voids*, Mon. Not. Roy. Astron. Soc. **454** (2015) 3357, [arXiv:1404.1834].

[34] F. Hoyle and M. S. Vogeley, *Voids in the Point Source Catalogue Survey and the Updated Zwicky Catalog*, Astrophys. J. **566** (2002) 641, [astro-ph/0109357].

[35] F. Hoyle and M. S. Vogeley, *Voids in the Two-degree Field Galaxy Redshift Survey*, Astrophys. J. **607** (2004) 751.

[36] C. Clarkson, G. F. R. Ellis, A. Faltenbacher, R. Maartens, O. Umeh and J. P. Uzan, *(Mis-)Interpreting supernovae observations in a lumpy universe*, Mon. Not. Roy. Astron. Soc. **426** (2012) 1121, [arXiv:1109.2484].

[37] K. Bolejko, *Weak lensing and the Dyer-Roeder approximation*, Mon. Not. Roy. Astron. Soc. **412** (2011) 1937, [arXiv:1011.3876].

[38] Y. B. Zel'dovich, *Observations in a Universe Homogeneous in the Mean*, Sov. Astron. **8** (1964) 13.

[39] C. C. Dyer and R. C. Roeder, *Distance-Redshift Relations for Universes with Some Intergalactic Medium*, Astrophys. J. **180** (1973) L31.

[40] P. Fleury, H. Dupuy and J. P. Uzan, *Interpretation of the Hubble diagram in a nonhomogeneous universe*, Phys. Rev. D **87** (2013) 123526, [arXiv:1302.5308].

[41] P. Fleury, *Swiss-cheese models and the Dyer-Roeder approximation*, JCAP **06** (2014) 054, [arXiv:1402.3123].

[42] G. Lemaître, *The expanding universe*, Annales Soc. Sci. Brux. Ser. I Sci. Math. Astron. Phys. A **53** (1933) 51.

[43] R. C. Tolman, *Effect of imhomogeneity on cosmological models*, Proc. Nat. Acad. Sci. **20** (1934) 169.

[44] H. Bondi, *Spherically symmetrical models in general relativity*, Mon. Not. Roy. Astron. Soc. **107** (1947) 410.

[45] H. Alnes, M. Amarzguioui and O. Gron, *An inhomogeneous alternative to dark energy?*, Phys. Rev. D **73** (2006) 083519, [astro-ph/0512006].

[46] K. Enqvist and T. Mattsson, *The effect of inhomogeneous expansion on the supernova observations*, JCAP **02** (2007) 019. [astro-ph/0609120].

[47] M. N. Celerier, K. Bolejko and A. Krasinski, *A (giant) void is not mandatory to explain away dark energy with a Lemaitre – Tolman model*, Astron. Astrophys. **518** (2010) A21, [arXiv:0906.0905].

[48] J. P. Zibin, A. Moss and D. Scott, *Can we avoid dark energy?*, Phys. Rev. Lett. **101** (2008) 251303, [arXiv:0809.3761].

[49] G. F. R. Ellis, *Inhomogeneity effects in Cosmology*, Class. Quant. Grav. **28** (2011) 164001, [arXiv:1103.2335].

[50] S. Räsänen, *Backreaction: directions of progress*, Class. Quant. Grav. **28** (2011) 164008, [arXiv:1102.0408].

[51] E. W. Kolb, *Backreaction of inhomogeneities can mimic dark energy*, Class. Quant. Grav. **28** (2011) 164009.

[52] C. Clarkson, G. Ellis, J. Larena and O. Umeh, *Does the growth of structure affect our dynamical models of the universe? The averaging, backreaction and fitting problems in cosmology*, Rept. Prog. Phys. **74** (2011) 112901, [arXiv:1109.2314].

[53] T. Buchert, *On Average Properties of Inhomogeneous Fluids in General Relativity: Dust Cosmologies*, Gen. Rel. Grav. **32** (2000) 105, [gr-qc/9906015].

[54] T. Buchert, *On Average Properties of Inhomogeneous Fluids in General Relativity: Perfect Fluid Cosmologies*, Gen. Rel. Grav. **33** (2001) 1381, [gr-qc/0102049].

[55] T. Buchert *et al.*, *Is there proof that backreaction of inhomogeneities is irrelevant in cosmology?*, Class. Quant. Grav. **32** (2015) 215021, [arXiv:1505.07800].

[56] S. R. Green and R. M. Wald, *A new framework for analyzing the effects of small scale inhomogeneities in cosmology*, Phys. Rev. D **83** (2011) 084020, [arXiv:1011.4920].

[57] S. R. Green and R. M. Wald, *Newtonian and Relativistic Cosmologies*, Phys. Rev. D **85** (2012) 063512, [arXiv:1111.2997].

[58] S. R. Green and R. M. Wald, *Examples of backreaction of small scale inhomogeneities in cosmology*, Phys. Rev. D **87** (2013) 124037, [arXiv:1304.2318].

[59] S. R. Green and R. M. Wald, *Comments on Backreaction*, [arXiv:1506.06452].

[60] A. Ishibashi and R. M. Wald, *Can the acceleration of our universe be explained by the effects of inhomogeneities?*, Class. Quant. Grav. **23** (2006) 235, [gr-qc/0509108].

[61] D. L. Wiltshire, *Cosmic clocks, cosmic variance and cosmic averages*, New. J. Phys. **9** (2007) 377, [gr-qc/0702082].

[62] D. L. Wiltshire, *Cosmological equivalence principle and the weak-field limit*, Phys. Rev. D **78** (2008) 084032, [arXiv:0809.1183].

[63] D. W. Hogg, D. J. Eisenstein, M. R. Blanton, N. A. Bahcall, J. Brinkmann, J. E. Gunn and D. P. Schneider, *Cosmic homogeneity demonstrated with luminous red galaxies*, Astrophys. J. **624** (2005) 54, [astro-ph/0411197].

[64] F. S. Labini, N. L. Vasilyev, L. Pietronero and Y. V. Baryshev, *Absence of self-averaging and of homogeneity in the large scale galaxy distribution*, Europhys. Lett. **86** (2009) 49001, [arXiv:0805.1132].

[65] M. Scrimgeour *et al.*, *The WiggleZ Dark Energy Survey: the transition to large-scale cosmic homogeneity*, Mon. Not. Roy. Astron. Soc. **425** (2012) 116, [arXiv:1205.6812].

[66] B. F. Roukema, T. Buchert, H. Fujii and J. J. Ostrowski, *Is the baryon acoustic oscillation peak a cosmological standard ruler?*, Mon. Not. Roy. Astron. Soc. **456** (2016) L45, [arXiv:1506.05478].

[67] A. Gabrielli, F. Sylos Labini, M. Joyce and L. Pietronero, *Statistical physics for cosmic structures*, Springer, Berlin, 2005.

[68] R. B. Tully, E. J. Shaya, I. D. Karachentsev, H. M. Courtois, D. D. Kocevski, L. Rizzi and A. Peel, *Our Peculiar Motion Away from the Local Void*, Astrophys. J. **676** (2008) 184, [arXiv:0705.4139].

[69] Y. Hoffman, D. Pomarède, R. B. Tully and H. M. Courtois, *The dipole repeller*, Nature Astron. **1** (2017) 0036.

[70] P. J. E. Peebles, *The large-scale structure of the universe*, Princeton University Press, Princeton, 1980.

[71] S. Hess and F. S. Kitaura, *Cosmic flows and the expansion of the local Universe from non-linear phasespace reconstructions*, Mon. Not. Roy. Astron. Soc. **456** (2016) 4247, [arXiv:1412.7310].

[72] W. A. Hellwing, A. Nusser, M. Feix and M. Bilicki, *Not a Copernican observer: biased peculiar velocity statistics in the local Universe*, [arXiv:1609.07120].

[73] R. Watkins, H. A. Feldman and M. J. Hudson, *Consistently Large Cosmic Flows on Scales of* $100\,h^{-1}$ *Mpc: a challenge for the standard* Λ*CDM cosmology*, Mon. Not. Roy. Astron. Soc. **392** (2009) 743, [arXiv:0809.4041].

[74] H. A. Feldman, R. Watkins and M. J. Hudson, *Cosmic Flows on* $100\,h^{-1}$ *Mpc Scales: Standardized Minimum Variance Bulk Flow, Shear and Octupole Moments*, Mon. Not. Roy. Astron. Soc. **407** (2010) 2328, [arXiv:0911.5516].

[75] A. Kashlinsky, F. Atrio-Barandela, H. Ebeling, A. Edge and D. Kocevski, *A new measurement of the bulk flow of X-ray luminous clusters of galaxies*, Astrophys. J. **712** (2010) L81, [arXiv:0910.4958].

[76] G. Lavaux, R. B. Tully, R. Mohayaee and S. Colombi, *Cosmic flow from 2MASS redshift survey: The origin of CMB dipole and implications for LCDM cosmology*, Astrophys. J. **709** (2010) 483, [arXiv:0810.3658].

[77] A. Nusser and M. Davis, *The cosmological bulk flow: consistency with* Λ*CDM and* $z \approx 0$ *constraints on* σ_8 *and* γ, Astrophys. J. **736** (2011) 93, [arXiv:1101.1650].

[78] S. J. Turnbull, M. J. Hudson, H. A. Feldman, M. Hicken, R. P. Kirshner and R. Watkins, *Cosmic flows in the nearby universe from Type Ia Supernovae*, Mon. Not. Roy. Astron. Soc. **420** (2012) 447, [arXiv:1111.0631].

[79] G. Lavaux, N. Afshordi and M. J. Hudson, *First measurement of the bulk flow of nearby galaxies using the cosmic microwave background*, Mon. Not. Roy. Astron. Soc. **430** (2013) 1617, [arXiv:1207.1721].

[80] Y. Z. Ma and D. Scott, *Cosmic bulk flows on* $50h^{-1}$ *Mpc scales: A Bayesian hyper-parameter method and multi-shells likelihood analysis*, Mon. Not. Roy. Astron. Soc. **428** (2013) 2017, [arXiv:1208.2028].

[81] P. A. R. Ade *et al.* [Planck Collaboration], *Planck intermediate results. XIII. Constraints on peculiar velocities*, Astron. Astrophys. **561** (2014) A97, [arXiv:1303.5090].

[82] F. Atrio-Barandela, *On the Statistical Significance of the Bulk Flow Measured by the PLANCK Satellite*, Astron. Astrophys. **557** (2013) A116, [arXiv:1303.6614].

[83] Y. Hoffman, H. M. Courtois and R. B. Tully, *Cosmic Bulk Flow and the Local Motion from Cosmicflows-2*, Mon. Not. Roy. Astron. Soc. **449** (2015) 4494, [arXiv:1503.05422].

[84] J. Carrick, S. J. Turnbull, G. Lavaux and M. J. Hudson, *Cosmological parameters from the comparison of peculiar velocities with predictions from the 2M++ density field*, Mon. Not. Roy. Astron. Soc. **450** (2015) 317, [arXiv:1504.04627].

[85] P. Erdoğdu *et al.*, *Reconstructed Density and Velocity Fields from the 2MASS Redshift Survey*, Mon. Not. Roy. Astron. Soc. **373** (2006) 45, [astro-ph/0610005]

[86] U. Feindt *et al.*, *Measuring cosmic bulk flows with Type Ia Supernovae from the Nearby Supernova Factory*, Astron. Astrophys. **560** (2013) A90, [arXiv:1310.4184]

[87] D. L. Wiltshire, P. R. Smale, T. Mattsson and R. Watkins, *Hubble flow variance and the cosmic rest frame*, Phys. Rev. D **88** (2013) 083529, [arXiv:1201.5371].

[88] J. H. McKay and D. L. Wiltshire, *Defining the frame of minimum non-linear Hubble expansion variation*, Mon. Not. Roy. Astron. Soc. **457** (2016) 3285; err. ibid. **463** (2016) 3113, [arXiv:1503.04192].

[89] N. Li and D. J. Schwarz, *Scale dependence of cosmological backreaction*, Phys. Rev. D **78** (2008) 083531, [arXiv:0710.5073].

[90] M. L. McClure and C. C. Dyer, *Anisotropy in the Hubble constant as observed in the HST Extragalactic Distance Scale Key Project results*, New Astron. **12** (2007) 533, [astro-ph/0703556].

[91] R. B. Tully *et al.*, *Cosmicflows-2: The Data*, Astron. J. **146** (2013) 86, [arXiv:1307.7213].

[92] A. G. Riess *et al.*, *A 3% Solution: Determination of the Hubble Constant with the Hubble Space Telescope and Wide Field Camera 3*, Astrophys. J. **730** (2011) 119; err. ibid. **732** (2011) 129, [arXiv:1103.2976].

[93] D. Kraljic and S. Sarkar, *Frames of most uniform Hubble flow*, JCAP **10** (2016) 016, [arXiv:1607.07377].

[94] P. Szekeres, *A Class of Inhomogeneous Cosmological Models*, Commun. Math. Phys. **41** (1975) 55.

[95] M. Tegmark, A. de Oliveira-Costa and A. Hamilton, *A high resolution foreground cleaned CMB map from WMAP*, Phys. Rev. D **68** (2003) 123523, [astro-ph/0302496].

[96] H. K. Eriksen, F. K. Hansen, A. J. Banday, K. M. Gorski and P. B. Lilje, *Asymmetries in the Cosmic Microwave Background anisotropy field*, Astrophys. J. **605** (2004) 14; Err. ibid. **609** (2004) 1198, [astro-ph/0307507].

[97] H. K. Eriksen, A. J. Banday, K. M. Gorski, F. K. Hansen and P. B. Lilje, *Hemispherical power asymmetry in the three-year Wilkinson Microwave Anisotropy Probe sky maps*, Astrophys. J. **660** (2007) L81, [astro-ph/0701089].

[98] J. Hoftuft, H. K. Eriksen, A. J. Banday, K. M. Gorski, F. K. Hansen and P. B. Lilje, *Increasing evidence for hemispherical power asymmetry in the five-year WMAP data*, Astrophys. J. **699** (2009) 985, [arXiv:0903.1229].

[99] A. de Oliveira-Costa, M. Tegmark, M. Zaldarriaga and A. Hamilton, *The Significance of the largest scale CMB fluctuations in WMAP*, Phys. Rev. D **69** (2004) 063516, [astro-ph/0307282].

[100] D. J. Schwarz, G. D. Starkman, D. Huterer and C. J. Copi, *Is the low-l microwave background cosmic?*, Phys. Rev. Lett. **93** (2004) 221301, [astro-ph/0403353].

[101] C. J. Copi, D. Huterer, D. J. Schwarz and G. D. Starkman, *On the large-angle anomalies of the microwave sky*, Mon. Not. Roy. Astron. Soc. **367** (2006) 79, [astro-ph/0508047].

[102] A. Rakic, S. Räsänen and D. J. Schwarz, *Microwave sky and the local Rees-Sciama effect*, Mon. Not. Roy. Astron. Soc. **369** (2006) L27, [astro-ph/0601445].

[103] K. T. Inoue and J. Silk, *Local voids as the origin of large-angle cosmic microwave background anomalies I*, Astrophys. J. **648** (2006) 23, [astro-ph/0602478].

[104] J. Kim and P. Naselsky, *Anomalous parity asymmetry of the Wilkinson Microwave Anisotropy Probe power spectrum data at low multipoles*, Astrophys. J. **714** (2010) L265, [arXiv:1001.4613].

[105] P. A. R. Ade *et al.* [Planck Collaboration], *Planck 2013 results. XXIII. Isotropy and statistics of the CMB*, Astron. Astrophys. **571** (2014) A23, [arXiv:1303.5083].

[106] D. J. Schwarz, C. J. Copi, D. Huterer and G. D. Starkman, *CMB Anomalies after Planck*, Class. Quant. Grav. **33** (2016) 184001, [arXiv:1510.07929].

[107] P. E. Freeman, C. R. Genovese, C. J. Miller, R. C. Nichol and L. Wasserman, *Examining the effect of the map-making algorithm on observed power asymmetry in wmap data*, Astrophys. J. **638** (2006) 1, [astro-ph/0510406].

[108] N. Aghanim *et al.* [Planck Collaboration], *Planck 2013 results. XXVII. Doppler boosting of the CMB: Eppur si muove*, Astron. Astrophys. **571** (2014) A27, [arXiv:1303.5087].

[109] A. Kosowsky and T. Kahniashvili, *The Signature of Proper Motion in the Microwave Sky*, Phys. Rev. Lett. **106** (2011) 191301, [arXiv:1007.4539].

[110] L. Amendola, R. Catena, I. Masina, A. Notari, M. Quartin and C. Quercellini, *Measuring our peculiar velocity on the CMB with high-multipole off-diagonal correlations*, JCAP **07** (2011) 027, [arXiv:1008.1183].

[111] H. Alnes and M. Amarzguioui, *CMB anisotropies seen by an off-center observer in a spherically symmetric inhomogeneous Universe*, Phys. Rev. D **74** (2006) 103520, [astro-ph/0607334].

[112] T. Biswas, A. Notari and W. Valkenburg, *Testing the Void against Cosmological data: fitting CMB, BAO, SN and H_0*, JCAP **11** (2010) 030, [arXiv:1007.3065].

[113] A. Meszaros and Z. Molnar, *On the alternative origin of the dipole anisotropy of microwave background due to the Rees-Sciama effect*, Astrophys. J. **470** (1996) 49.

[114] O. Roldan, A. Notari and M. Quartin, *Interpreting the CMB aberration and Doppler measurements: boost or intrinsic dipole?*, JCAP **06** (2016) 026, [arXiv:1603.02664].

[115] G. Cusin, C. Pitrou and J. P. Uzan, *Are we living near the center of a local void?*, [arXiv:1609.02061].

[116] J. P. Zibin, *Scalar Perturbations on Lemaître-Tolman-Bondi Spacetimes*, Phys. Rev. D **78** (2008) 043504, [arXiv:0804.1787].

[117] C. Clarkson, T. Clifton and S. February, *Perturbation Theory in Lemaître-Tolman-Bondi Cosmology*, JCAP **06** (2009) 025, [arXiv:0903.5040].

[118] R. Durrer, *The Cosmic Microwave Background*, Cambridge University Press, Cambridge, 2009.

[119] D. J. Heath, *The growth of density perturbations in zero pressure Friedmann–Lemaître universes*, Mon. Not. Roy. Astron. Soc. **179** (1977) 351.

[120] K. Tomita, *Relativistic second-order perturbations of nonzero-Λ flat cosmological models and CMB anisotropies*, Phys. Rev. D **71** (2005) 083504, [astro-ph/0501663].

[121] O. Lahav, P. B. Lilje, J. R. Primack and M. J. Rees, *Dynamical effects of the cosmological constant*, Mon. Not. Roy. Astron. Soc. **251** (1991) 128.

[122] R. K. Sachs and A. M. Wolfe, *Perturbations of a cosmological model and angular variations of the microwave background*, Astrophys. J. **147** (1967) 73.

[123] M. J. Rees and D. W. Sciama, *Large scale Density Inhomogeneities in the Universe*, Nature **217** (1968) 511.

[124] A. Lewis and A. Challinor, *Weak gravitational lensing of the CMB*, Phys. Rept. **429** (2006) 1, [astro-ph/0601594].

[125] A. Lewis and A. Challinor, *Weak Gravitational Lensing of the CMB*, Phys. Rept. **429** (2006) 1, [astro-ph/0601594].

[126] G. F. R. Ellis, *Relativistic cosmology: its nature, aims and problems*, in B. Bertotti, F. de Felice and A. Pascolini (eds.), *General Relativity and Gravitation*, (D. Reidel Publishing Co., Dordrecht, Holland, 1984) pp. 215–288.

[127] G. F. R. Ellis and W. Stoeger, *The 'fitting problem' in cosmology*, Class. Quant. Grav. **4** (1987) 1697.

[128] V. Marra, L. Amendola, I. Sawicki and W. Valkenburg, *Cosmic variance and the measurement of the local Hubble parameter*, Phys. Rev. Lett. **110** (2013) 241305, [arXiv:1303.3121].

[129] E. U. Condon and G. H. Shortley, *The Theory of Atomic Spectra*, Cambridge University Press, Cambridge, 1970.

[130] K. Bolejko, *in preparation.*

[131] E. Hivon, K. M. Gorski, C. B. Netterfield, B. P. Crill, S. Prunet and F. Hansen, *MASTER of the Cosmic Microwave Background Anisotropy Power Spectrum: A Fast Method for Statistical Analysis of Large and Complex Cosmic Microwave Background Data Sets*, Astrophys. J. **567** (2002) 2, [astro-ph/0105302].

[132] F.-X. Dupe, A. Rassat, J.-L. Starck and M. J. Fadili, *Measuring the Integrated Sachs-Wolfe Effect*, Astron. Astrophys. **534** (2011) A51, [arXiv:1010.2192].

[133] S. Weinberg, *Cosmology*, Oxford University Press, Oxford, 2009.

[134] R. G. Crittenden and N. Turok, *Looking for a Cosmological constant with the Rees-Sciama Effect*, Phys. Rev. Lett. **76** (1996) 575.

[135] N. Kaiser, *On the Spatial correlations of Abell clusters*, Astrophys. J. **284** (1984) L9.

[136] A. J. Nishizawa, *The integrated Sachs-Wolfe effect and the Rees-Sciama effect*, Prog. Theor. Exp. Phys. **2014** (2014) 06B110, [arXiv:1404.5102].

[137] T. Giannantonio, R. Scranton, R. G. Crittenden, R. C. Nichol, S. P. Boughn, A. D. Myers and G. T. Richards, *Combined analysis of the integrated Sachs-Wolfe effect and cosmological implications*, Phys. Rev. D **77** (2008) 123520, [arXiv:0801.4380].

[138] B. R. Granett, M. C. Neyrinck and I. Szapudi, *An Imprint of Super-Structures on the Microwave Background due to the Integrated Sachs-Wolfe Effect*, Astrophys. J. **683** (2008) L99, [arXiv:0805.3695].

[139] P. A. R. Ade *et al.* [Planck Collaboration], *Planck 2015 results. XXI. The integrated Sachs-Wolfe effect*, Astron. Astrophys. **594** (2016) A21 [arXiv:1502.01595].

[140] S. Nadathur, S. Hotchkiss and S. Sarkar, *The integrated Sachs-Wolfe imprints of cosmic superstructures: a problem for ΛCDM*, JCAP **06** (2012) 042, [arXiv:1109.4126].

[141] J. M. Bardeen, J. R. Bond, N. Kaiser and A. S. Szalay, *The Statistics of Peaks of Gaussian Random Fields*, Astrophys. J. **304** (1986) 15.

[142] Y. C. Cai, S. Cole, A. Jenkins and C. S. Frenk, *Full-sky map of the ISW and Rees-Sciama effect from Gpc simulations*, Mon. Not. Roy. Astron. Soc. **407** (2010) 201, [arXiv:1003.0974].

[143] S. Flender, S. Hotchkiss and S. Nadathur, *The stacked ISW signal of rare superstructures in ΛCDM*, JCAP **02** (2013) 013, [arXiv:1212.0776].

[144] S. Nadathur and R. Crittenden, *A detection of the integrated Sachs-Wolfe imprint of cosmic superstructures using a matched-filter approach*, Astrophys. J. **830** (2016) L19, [arXiv:1608.08638].

[145] I. Szapudi *et al.*, *Detection of a Supervoid Aligned with the Cold Spot of the Cosmic Microwave Background*, Mon. Not. Roy. Astron. Soc. **450** (2015) 288, [arXiv:1405.1566].

[146] F. Finelli, J. Garcia-Bellido, A. Kovacs, F. Paci and I. Szapudi, *Supervoids in the WISE-2MASS catalogue imprinting Cold Spots in the Cosmic Microwave Background*, [arXiv:1405.1555].

[147] S. Nadathur, M. Lavinto, S. Hotchkiss and S. Räsänen, *Can a supervoid explain the Cold Spot?*, Phys. Rev. D **90** (2014) 10, 103510, [arXiv:1408.4720].

[148] W. A. Watson *et al.*, *The Jubilee ISW Project I: Simulated ISW and weak lensing maps and initial power spectra results*, Mon. Not. Roy. Astron. Soc. **438** (2014) 412, [arXiv:1307.1712].

[149] F. Pretorius, *Evolution of binary black hole spacetimes*, Phys. Rev. Lett. **95** (2005) 121101, [gr-qc/0507014].

[150] J. T. Giblin, J. B. Mertens and G. D. Starkman, *Departures from the Friedmann-Lemaître-Robertston-Walker Cosmological Model in an Inhomogeneous Universe: A Numerical Examination*, Phys. Rev. Lett. **116** (2016) 251301, [arXiv:1511.01105].

[151] E. Bentivegna and M. Bruni, *Effects of nonlinear inhomogeneity on the cosmic expansion with numerical relativity*, Phys. Rev. Lett. **116** (2016) 251302, [arXiv:1511.05124].

[152] T. Baumgarte and S. L. Shapiro, *Numerical relativity: solving Einstein's equations on the computer*, Cambridge University Press, Cambridge, 2010.

[153] J. Ehlers, *Contributions to the relativistic mechanics of continuous media*, Abh. Akad. Wiss. Lit. Mainz. Nat. Kl. **11** (1961) 793.

[154] G. F. R. Ellis, *Relativistic cosmology*, Proceedings of the International School of Physics "Enrico Fermi", Academic Press, New York and London, 1971 pp. 104-182.

[155] W. Valkenburg, *Complete solutions to the metric of spherically collapsing dust in an expanding spacetime with a cosmological constant*, Gen. Rel. Grav. **44** (2012) 2449, [arXiv:1104.1082].

[156] K. Bolejko, A. Krasinski, C. Hellaby and M. N. Celerier, *Structures in the Universe by Exact Methods: Formation, Evolution, Interactions*, Cambridge University Press, Cambridge, 2009.

[157] A. Krasinski and C. Hellaby, *Structure formation in the Lemaitre-Tolman model*, Phys. Rev. D **65** (2002) 023501.

[158] A. Krasinski and C. Hellaby, *More examples of structure formation in the Lemaitre-Tolman model*, Phys. Rev. D **69** (2004) 023502.

[159] J. Wainwright and S. Andrews, *The Dynamics of Lemaitre-Tolman cosmologies*, Class. Quant. Grav. **26** (2009) 085017.

[160] J. Silk, *Large-scale Inhomogeneity of the Universe: Spherically Symmetric Models*. Astron. Astrophys. **59** (1977) 53.

[161] C. Hellaby and K. Lake, *Shell crossings and the Tolman model*, Astrophys. J. **290** (1985) 381.

[162] D. A. Szafron, *Inhomogeneous cosmologies: New exact solutions and their evolution*, J. Math. Phys. **18** (1977) 1673.

[163] J. Plebanski and A. Krasinski, *An Introduction to General Relativity and Cosmology*, Cambridge University Press, Cambridge, 2006.

[164] C. Hellaby, *The null and KS limits of the Szekeres model*, Class. Quant. Grav. **13** (1996) 2537.

[165] A. Einstein and E. G. Straus, *The influence of the expansion of space on the gravitation fields surrounding the individual stars*, Rev. Mod. Phys. **17** (1945) 120.

[166] G. Darmois, *Les équations de la gravitation einsteinienne*, Ch. V, Mémorial de Sciences Mathématiques, Fascicule XXV (1927).

[167] W. Israel, *Singular hypersurfaces and thin shells in general relativity*, Nuovo Cim. B **44** (1966) 1.

[168] K. Bolejko, *Evolution of cosmic structures in different environments in the quasispherical Szekeres model*, Phys. Rev. D **75** (2007) 043508, [astro-ph/0610292].

[169] A. Krasinski and K. Bolejko, *Redshift propagation equations in the $\beta' \neq 0$ Szekeres models*, Phys. Rev. D **83** (2011) 083503, [arXiv:1007.2083].

[170] K. Bolejko, *in preparation.*

[171] E. Hivon, K. M. Gorski, C. B. Netterfield, B. P. Crill, S. Prunet and F. Hansen, *MASTER of the Cosmic Microwave Background Anisotropy Power Spectrum: A Fast Method for Statistical Analysis of Large and Complex Cosmic Microwave Background Data Sets*, Astrophys. J. **567** (2002) 2, [astro-ph/0105302].

[172] C. J. Copi, D. Huterer and G. D. Starkman, *Multipole vectors: A new representation of the CMB sky and evidence for statistical anisotropy or non-Gaussianity at $2 \leq \ell \leq 8$*, Phys. Rev. D **70** (2004) 043515, [astro-ph/0310511].

[173] R. Catena and A. Notari, *Cosmological parameter estimation: impact of CMB aberration*, JCAP **04** (2013) 028, [arXiv:1210.2731].

[174] P. Schneider, J. Ehlers, and E. E. Falco, *Gravitational Lenses*, Springer-Verlag, Berlin, 1992.

[175] K. Bolejko and P. G. Ferreira, *Ricci focusing, shearing, and the expansion rate in an almost homogeneous Universe*, JCAP **05** (2012) 003, [arXiv:1204.0909].

[176] G. Fanizza and F. Nugier, *Lensing in the geodesic light-cone coordinates and its (exact) illustration to an off-center observer in Lemaître-Tolman-Bondi models*, JCAP **02** (2015) 002, [arXiv:1408.1604].

[177] C. Gordon, W. Hu, D. Huterer and T. M. Crawford, *Spontaneous isotropy breaking: a mechanism for cmb multipole alignments*, Phys. Rev. D **72** (2005) 103002, [arXiv:astro-ph/0509301].

[178] S. Prunet, J. P. Uzan, F. Bernardeau and T. Brunier, *Constraints on mode couplings and modulation of the CMB with WMAP data*, Phys. Rev. D **71** (2005) 083508, [arXiv:astro-ph/0406364].

[179] P. K. Rath and P. Jain, *Testing the Dipole Modulation Model in CMBR*, JCAP **12** (2013) 014, [arXiv:1308.0924].

[180] K. Van Acoleyen, *LTB solutions in Newtonian gauge: from strong to weak fields*, JCAP **10** (2008) 028, [arXiv:0808.3554].

[181] A. Paranjape and T. P. Singh, *Structure Formation, Backreaction and Weak Gravitational Fields*, JCAP **03** (2008) 023, [arXiv:0801.1546].

[182] K. Yamamoto, V. Marra, V. Mukhanov and M. Sasaki, *Perturbed Newtonian description of the Lematre model with non-negligible pressure*, JCAP **03** (2016) 030, [arXiv:1512.04240].

[183] R. A. Sussman, I. Delgado Gaspar and J. C. Hidalgo, *Coarse-grained description of cosmic structure from Szekeres models*, JCAP **03** (2016) 012; Err. ibid. **06** (2016) E03, [arXiv:1507.02306].

[184] D. A. Varshalovich, A. N. Moskalev and V. K. Khersonsky, *Quantum Theory of Angular Momentum: Irreducible Tensors, Spherical Harmonics, Vector Coupling Coefficients, 3nj Symbols*, World Scientific, Singapore, 1988.

Appendix A

Christoffel symbols and the null geodesic equations

For completeness we collect here the elements needed in the ray tracing code.

The non-zero LTB Christoffel symbols are

$$\Gamma^t{}_{rr} = \frac{R'\dot{R}'}{1+2E}, \qquad \Gamma^t{}_{\theta\theta} = R\dot{R}, \qquad \Gamma^t{}_{\phi\phi} = \dot{R}R\sin^2\theta,$$
$$\Gamma^r{}_{tr} = \frac{\dot{R}'}{R'}, \qquad \Gamma^r{}_{rr} = \frac{R''}{R'} - \frac{E'}{1+2E}, \qquad \Gamma^r{}_{\theta\theta} = -(1+2E)\frac{R}{R'},$$
$$\Gamma^r{}_{\phi\phi} = -(1+2E)\frac{R}{R'}\sin^2\theta,$$
$$\Gamma^\theta{}_{\theta t} = \Gamma^\phi{}_{\phi t} = \frac{\dot{R}}{R}, \qquad \Gamma^\theta{}_{\theta r} = \Gamma^\phi{}_{\phi r} = \frac{R'}{R}, \qquad \Gamma^\theta{}_{\phi\phi} = -\sin\theta\cos\theta, \qquad \Gamma^\phi{}_{\theta\phi} = \cot\theta.$$

The LTB null geodesic equations are

$$\frac{\mathrm{d}^2t}{\mathrm{d}\lambda^2} - \frac{J^2}{R^2}\left(\frac{\dot{R}'}{R'} - \frac{\dot{R}}{R}\right) + \frac{\dot{R}'}{R'}\left(\frac{\mathrm{d}t}{\mathrm{d}\lambda}\right)^2 = 0, \tag{A.1}$$

$$\frac{\mathrm{d}^2r}{\mathrm{d}\lambda^2} - (1+2E)\frac{R}{R'}\left(\frac{\mathrm{d}\phi}{\mathrm{d}\lambda}\right)^2 + \left(\frac{R''}{R'} - \frac{E'}{1+2E}\right)\left(\frac{\mathrm{d}r}{\mathrm{d}\lambda}\right)^2 + 2\frac{\dot{R}'}{R'}\,\frac{\mathrm{d}t}{\mathrm{d}\lambda}\,\frac{\mathrm{d}r}{\mathrm{d}\lambda} = 0, \tag{A.2}$$

$$\frac{\mathrm{d}^2\phi}{\mathrm{d}\lambda^2} + \frac{1}{R}\,\frac{\mathrm{d}R}{\mathrm{d}\lambda}\,\frac{\mathrm{d}\phi}{\mathrm{d}\lambda} + \cot\theta\,\frac{\mathrm{d}\phi}{\mathrm{d}\lambda}\,\frac{\mathrm{d}\theta}{\mathrm{d}\lambda} = 0, \tag{A.3}$$

$$\frac{\mathrm{d}^2\theta}{\mathrm{d}\lambda^2} + \frac{1}{R}\,\frac{\mathrm{d}R}{\mathrm{d}\lambda}\,\frac{\mathrm{d}\theta}{\mathrm{d}\lambda} - \sin\theta\cos\theta\left(\frac{\mathrm{d}\phi}{\mathrm{d}\lambda}\right)^2 = 0. \tag{A.4}$$

These reduce to a system of two equations (with $k_\phi =$ constant and $k^\theta = 0$) by assuming the geodesic curve lies on the $\theta = \pi/2$ plane.

The Szekeres null geodesic equations in spherical coordinates $\{t, r, \theta, \phi\}$ are tedious to compute. However, in coordinates $\{t, r, x, y\}$ they can be found in Appendix A of [169].

They are

$$\frac{\mathrm{d}^2t}{\mathrm{d}\lambda^2}+\frac{\dot{\Phi}'-\dot{\Phi}\,\mathcal{E}'/\mathcal{E}}{\epsilon-k}(\Phi'-\Phi\mathcal{E}'/\mathcal{E})\left(\frac{\mathrm{d}r}{\mathrm{d}\lambda}\right)^2+\frac{\Phi\dot{\Phi}}{\mathcal{E}^2}\left[\left(\frac{\mathrm{d}x}{\mathrm{d}\lambda}\right)^2+\left(\frac{\mathrm{d}y}{\mathrm{d}\lambda}\right)^2\right]=0, \tag{A.5}$$

$$\begin{aligned}\frac{\mathrm{d}^2r}{\mathrm{d}\lambda^2}&+2\frac{\dot{\Phi}'-\dot{\Phi}\,\mathcal{E}'/\mathcal{E}}{\Phi'-\Phi\,\mathcal{E}'/\mathcal{E}}\frac{\mathrm{d}t}{\mathrm{d}\lambda}\frac{\mathrm{d}r}{\mathrm{d}\lambda}+\left(\frac{\Phi''-\Phi\,\mathcal{E}''/\mathcal{E}}{\Phi'-\Phi\,\mathcal{E}'/\mathcal{E}}-\frac{\mathcal{E}'}{\mathcal{E}}+\frac{1}{2}\frac{k'}{\epsilon-k}\right)\left(\frac{\mathrm{d}r}{\mathrm{d}\lambda}\right)^2\\&+2\frac{\Phi}{\mathcal{E}^2}\frac{\mathcal{E}'\,\mathcal{E}_{,x}-\mathcal{E}\mathcal{E}'_{,x}}{\Phi'-\Phi\,\mathcal{E}'/\mathcal{E}}\frac{\mathrm{d}r}{\mathrm{d}\lambda}\frac{\mathrm{d}x}{\mathrm{d}\lambda}+2\frac{\Phi}{\mathcal{E}^2}\frac{\mathcal{E}'\,\mathcal{E}_{,y}-\mathcal{E}\mathcal{E}'_{,y}}{\Phi'-\Phi\,\mathcal{E}'/\mathcal{E}}\frac{\mathrm{d}r}{\mathrm{d}\lambda}\frac{\mathrm{d}y}{\mathrm{d}\lambda}\\&-\frac{\Phi}{\mathcal{E}^2}\frac{\epsilon-k}{\Phi'-\Phi\,\mathcal{E}'/\mathcal{E}}\left[\left(\frac{\mathrm{d}x}{\mathrm{d}\lambda}\right)^2+\left(\frac{\mathrm{d}y}{\mathrm{d}\lambda}\right)^2\right]=0,\end{aligned} \tag{A.6}$$

$$\begin{aligned}\frac{\mathrm{d}^2x}{\mathrm{d}\lambda^2}&+2\frac{\dot{\Phi}}{\Phi}\frac{\mathrm{d}t}{\mathrm{d}\lambda}\frac{\mathrm{d}x}{\mathrm{d}\lambda}-\frac{1}{\Phi}\frac{\Phi'-\Phi\,\mathcal{E}'/\mathcal{E}}{\epsilon-k}(\mathcal{E}'\,\mathcal{E}_{,x}-\mathcal{E}\,\mathcal{E}'_{,x})\left(\frac{\mathrm{d}r}{\mathrm{d}\lambda}\right)^2\\&+\frac{2}{\Phi}(\Phi'-\Phi\,\mathcal{E}'/\mathcal{E})\frac{\mathrm{d}r}{\mathrm{d}\lambda}\frac{\mathrm{d}x}{\mathrm{d}\lambda}-\frac{\mathcal{E}_{,x}}{\mathcal{E}}\left(\frac{\mathrm{d}x}{\mathrm{d}\lambda}\right)^2-2\frac{\mathcal{E}_{,y}}{\mathcal{E}}\frac{\mathrm{d}x}{\mathrm{d}\lambda}\frac{\mathrm{d}y}{\mathrm{d}\lambda}+\frac{\mathcal{E}_{,x}}{\mathcal{E}}\left(\frac{\mathrm{d}y}{\mathrm{d}\lambda}\right)^2=0,\end{aligned} \tag{A.7}$$

$$\begin{aligned}\frac{\mathrm{d}^2y}{\mathrm{d}\lambda^2}&+2\frac{\dot{\Phi}}{\Phi}\frac{\mathrm{d}t}{\mathrm{d}\lambda}\frac{\mathrm{d}y}{\mathrm{d}\lambda}-\frac{1}{\Phi}\frac{\Phi'-\Phi\,\mathcal{E}'/\mathcal{E}}{\epsilon-k}(\mathcal{E}'\,\mathcal{E}_{,y}-\mathcal{E}\,\mathcal{E}'_{,y})\left(\frac{\mathrm{d}r}{\mathrm{d}\lambda}\right)^2\\&+\frac{2}{\Phi}(\Phi'-\Phi\,\mathcal{E}'/\mathcal{E})\frac{\mathrm{d}r}{\mathrm{d}\lambda}\frac{\mathrm{d}y}{\mathrm{d}\lambda}-\frac{\mathcal{E}_{,y}}{\mathcal{E}}\left(\frac{\mathrm{d}x}{\mathrm{d}\lambda}\right)^2-2\frac{\mathcal{E}_{,x}}{\mathcal{E}}\frac{\mathrm{d}x}{\mathrm{d}\lambda}\frac{\mathrm{d}y}{\mathrm{d}\lambda}+\frac{\mathcal{E}_{,y}}{\mathcal{E}}\left(\frac{\mathrm{d}y}{\mathrm{d}\lambda}\right)^2=0,\end{aligned} \tag{A.8}$$

with dots and primes denoting partial derivatives of t and r respectively,

Appendix B

Details of the initial condition method

In this section we present in greater detail the steps outlined in §4.2.1 needed to compute the initial conditions.

First we determine the local orthonormal basis $\{\boldsymbol{e}_{\hat{a}}\}$. Note the line element in a local orthonormal frame reads

$$\mathrm{d}s^2 = g_{\mu\nu}\,\mathrm{d}x^\mu\,\mathrm{d}x^\nu = \eta_{\hat{a}\hat{b}}\boldsymbol{\omega}^{\hat{a}}\boldsymbol{\omega}^{\hat{b}}, \tag{B.1}$$

where $\eta_{\hat{a}\hat{a}} = \mathrm{diag}(-1,1,1,1)$ and the 1-forms $\{\boldsymbol{\omega}^{\hat{a}}\}$ are dual to $\{\boldsymbol{e}_{\hat{a}}\}$, i.e.,

$$\boldsymbol{\omega}^{\hat{a}}(\boldsymbol{e}_{\hat{b}}) = \omega^{\hat{a}}{}_{\mu}e_{\hat{b}}{}^{\mu} = \delta^{\hat{a}}{}_{\hat{b}}, \tag{B.2}$$

with $\omega^{\hat{a}}{}_{\mu}$ the components of $\boldsymbol{\omega}^{\hat{a}}$.

The Szekeres line element with the choice of functions (4.6) becomes

$$\begin{aligned}\mathrm{d}s^2 = &-\mathrm{d}t^2 + \frac{1}{1+2E}\left[R' + \frac{R}{S}(S'\cos\theta)\right]^2\mathrm{d}r^2 + R^2\left(\frac{S'}{S}\right)^2\sin^2\theta\,\mathrm{d}r^2\\ &- 2R^2\,\frac{S'}{S}\sin\theta\,\mathrm{d}r\,\mathrm{d}\theta + R^2(\mathrm{d}\theta^2 + \sin^2\theta\,\mathrm{d}\phi^2).\end{aligned} \tag{B.3}$$

The 1-forms are easily obtained by inspecting the line element (B.3). They are

$$\boldsymbol{\omega}^{\hat{0}} = \mathrm{d}t, \tag{B.4a}$$

$$\boldsymbol{\omega}^{\hat{1}} = \frac{R}{\sqrt{1+2E}}\left(\frac{R'}{R} + \frac{S'}{S}\cos\theta\right)\mathrm{d}r, \tag{B.4b}$$

$$\boldsymbol{\omega}^{\hat{2}} = -R\frac{S'}{S}\sin\theta\,\mathrm{d}r + R\,\mathrm{d}\theta, \tag{B.4c}$$

$$\boldsymbol{\omega}^{\hat{3}} = R\sin\theta\,\mathrm{d}\theta. \tag{B.4d}$$

From this the orthonormal basis can be recovered by solving (B.2), i.e., by inverting $\omega^{\hat{a}}{}_{\mu}$.

We find

$$\boldsymbol{e}_{\hat{0}} = \partial_t, \tag{B.5a}$$

$$\boldsymbol{e}_{\hat{1}} = \frac{\sqrt{1+2E}}{R}\left(\frac{R'}{R} + \frac{S'}{S}\cos\theta\right)^{-1}\left(\partial_r + \frac{S'}{S}\sin\theta\,\partial_\theta\right), \tag{B.5b}$$

$$\boldsymbol{e}_{\hat{2}} = \frac{1}{R}\partial_\theta, \tag{B.5c}$$

$$\boldsymbol{e}_{\hat{3}} = \frac{1}{R\sin\theta}\,\partial_\phi. \tag{B.5d}$$

In component form we have

$$e_{\hat{a}}{}^{\mu} = \begin{pmatrix} 1 & 0 & 0 & 0 \\ 0 & \Gamma & 0 & 0 \\ 0 & \Gamma\frac{S'}{S}\sin\theta & \frac{1}{R} & 0 \\ 0 & 0 & 0 & \frac{1}{R\sin\theta} \end{pmatrix}, \tag{B.6}$$

where

$$\Gamma \equiv \frac{\sqrt{1+2E}}{R}\left(\frac{R'}{R} + \frac{S'}{S}\cos\theta\right)^{-1}. \tag{B.7}$$

The initial null vectors are prescribed by

$$k_0^{\mu} = k^{\hat{a}} e_{\hat{a}}{}^{\mu}|_{t=t_0} = \begin{pmatrix} -1 \\ \Gamma\hat{n}^x \\ \Gamma\frac{S'}{S}\sin\theta\,\hat{n}^x + \frac{1}{R}\hat{n}^y \\ \frac{1}{R\sin\theta}\hat{n}^z \end{pmatrix}_{t=t_0}. \tag{B.8}$$

Appendix C

Justification for excluding quadrupole terms in (4.59)

Here we will demonstrate why the quadrupole can be neglected when we make the approximation in (4.59). We do this by revisiting (4.51), stated here for convenience:

$$\left\langle T'(\hat{\boldsymbol{n}}')\right\rangle_{\Omega'} \simeq \left\langle T(\hat{\boldsymbol{n}})\right\rangle_{\Omega}(1-\frac{1}{2}\beta^2) - \left\langle T(\hat{\boldsymbol{n}})\boldsymbol{\beta}\cdot\hat{\boldsymbol{n}}\right\rangle_{\Omega} + \left\langle(\boldsymbol{\beta}\cdot\hat{\boldsymbol{n}})^2 T(\hat{\boldsymbol{n}})\right\rangle_{\Omega}. \tag{C.1}$$

We shall simplify this by evaluating the second and third terms. (The first is trivial.) Thus we insert

$$T(\hat{\boldsymbol{n}}) = \sum_{\ell m} a_{\ell m} Y_{\ell m}(\hat{\boldsymbol{n}}), \tag{C.2}$$

in (C.1) but we make no assumptions on the size of the dipole, quadrupole etc.

The second term of (C.1) becomes

$$\begin{aligned}
\left\langle T(\hat{\boldsymbol{n}})\,\boldsymbol{\beta}\cdot\hat{\boldsymbol{n}}\right\rangle_{\Omega} &= \sum_{\ell m} a_{\ell m}\left\langle Y_{\ell m}(\hat{\boldsymbol{n}})(\boldsymbol{\beta}\cdot\hat{\boldsymbol{n}})\right\rangle_{\Omega} \\
&= \sum_{\ell m}\sum_{m'=-1}^{1} a_{\ell m} b^*_{1m'}\left\langle Y_{\ell m}(\hat{\boldsymbol{n}})Y^*_{1m'}(\hat{\boldsymbol{n}})\right\rangle_{\Omega} \\
&= \frac{1}{4\pi}\sum_{\ell m}\sum_{m'=-1}^{1} a_{\ell m} b^*_{1m'}\delta_{\ell 1}\delta_{mm'} \\
&= \frac{1}{4\pi}\sum_{m=-1}^{1} a_{1m} b^*_{1m} = \frac{1}{3}\boldsymbol{\beta}\cdot\boldsymbol{d}
\end{aligned} \tag{C.3}$$

where $\boldsymbol{\beta}\cdot\hat{\boldsymbol{n}} = \sum_m b_{1m}Y_{1m}(\hat{\boldsymbol{n}})$, (i.e., a pure dipole), and we have used (2.62) in the third equality. The last equality comes about using

$$\boldsymbol{d} = (d_x,\, d_y,\, d_z) = \sqrt{\frac{3}{4\pi}}(-\sqrt{2}a^{re}_{11},\, \sqrt{2}a^{im}_{11},\, a_{10}), \tag{C.4}$$

and some straightforward algebra:

$$\begin{aligned}\sum_{m=-1}^{1} a_{1m}b_{1m}^{*} &= a_{11}\,b_{11}^{*} + a_{10}\,b_{10} + a_{1-1}\,b_{1-1}^{*}\\ &= a_{11}\,b_{1-1} + a_{11}^{*}\,b_{1-1}^{*} + a_{10}\,b_{10}\\ &= a_{11}\,b_{1-1} + (a_{11}\,b_{1-1})^{*} + a_{10}\,b_{10}\\ &= 2\,\mathrm{Re}(a_{11}\,b_{1-1}) + a_{10}\,b_{10}\\ &= 2\left(a_{11}^{re}\,b_{1-1}^{re} + i^{2}a_{11}^{im}\,b_{1-1}^{im}\right) + a_{10}\,b_{10}\\ &= 2\left(a_{11}^{re}\,b_{11}^{re} + a_{11}^{im}\,b_{11}^{im}\right) + a_{10}\,b_{10}\\ &= (-\sqrt{2}b_{11}^{re},\,\sqrt{2}b_{11}^{im},\,b_{10})\cdot(-\sqrt{2}a_{11}^{re},\,\sqrt{2}a_{11}^{im},\,a_{10})\\ &= \frac{4\pi}{3}\boldsymbol{\beta}\cdot\boldsymbol{d}\end{aligned} \tag{C.5}$$

We define the quadrupole as

$$Q(\hat{\boldsymbol{n}}) = \sum_{m=-2}^{2} a_{2m}\,Y_{2m}(\hat{\boldsymbol{n}}). \tag{C.6}$$

The third term of (C.1) becomes

$$\begin{aligned}\left\langle(\boldsymbol{\beta}\cdot\hat{\boldsymbol{n}})^{2}\,T(\hat{\boldsymbol{n}})\right\rangle_{\Omega} &= \left\langle(\boldsymbol{\beta}\cdot\hat{\boldsymbol{n}})^{2}\right\rangle_{\Omega}\left\langle T(\hat{\boldsymbol{n}})\right\rangle_{\Omega} + \left\langle(\boldsymbol{\beta}\cdot\hat{\boldsymbol{n}})^{2}(\boldsymbol{d}\cdot\hat{\boldsymbol{n}}\right\rangle_{\Omega} + \left\langle(\boldsymbol{\beta}\cdot\hat{\boldsymbol{n}})^{2}\,Q(\hat{\boldsymbol{n}})\right\rangle_{\Omega} + \ldots\\ &= \frac{1}{3}\beta^{2}\left\langle T(\hat{\boldsymbol{n}})\right\rangle_{\Omega} + \left\langle(\boldsymbol{\beta}\cdot\hat{\boldsymbol{n}})^{2}\,Q(\hat{\boldsymbol{n}})\right\rangle_{\Omega} + \ldots\end{aligned} \tag{C.7}$$

where the second term of (C.7) is zero because

$$\left\langle(\boldsymbol{u}\cdot\hat{\boldsymbol{n}})(\boldsymbol{v}\cdot\hat{\boldsymbol{n}})(\boldsymbol{w}\cdot\hat{\boldsymbol{n}})\right\rangle_{\Omega} = 0, \tag{C.8}$$

for any vectors $\boldsymbol{u}$, $\boldsymbol{v}$ and $\boldsymbol{w}$. As an aside, the last term involving $Q(\hat{\boldsymbol{n}})$ involves the product of three $Y_{\ell m}$ and as such is not zero, but can be evaluated using the formula

$$\begin{aligned}\int \mathrm{d}\hat{\boldsymbol{n}}\,Y_{\ell_1 m_1}(\hat{\boldsymbol{n}})Y_{\ell_2 m_2}(\hat{\boldsymbol{n}})Y_{\ell_3 m_3}(\hat{\boldsymbol{n}}) &= \sqrt{\frac{(2\ell_1+1)(2\ell_2+1)(2\ell_3+1)}{4\pi}}\\ &\quad\times\begin{pmatrix}\ell_1 & \ell_2 & \ell_3\\ 0 & 0 & 0\end{pmatrix}\begin{pmatrix}\ell_1 & \ell_2 & \ell_3\\ m_1 & m_2 & m_3\end{pmatrix}\end{aligned} \tag{C.9}$$

where $\begin{pmatrix}\ell_1 & \ell_2 & \ell_3\\ m_1 & m_2 & m_3\end{pmatrix}$ is the Wigner 3j symbol. We remark $\left\langle(\boldsymbol{\beta}\cdot\hat{\boldsymbol{n}})^{2}(\boldsymbol{d}\cdot\hat{\boldsymbol{n}})\right\rangle_{\Omega}$ also involves the product of three Y_{1m} and this term can be shown to vanish using (C.9) with $\ell_1 = \ell_2 = \ell_3 = 1$ and the property that $\begin{pmatrix}\ell_1 & \ell_2 & \ell_3\\ 0 & 0 & 0\end{pmatrix}$ is zero if $\ell_1 + \ell_2 + \ell_3$ is an odd number.

Thus, (C.1) becomes

$$\begin{aligned}\left\langle T'(\hat{\boldsymbol{n}}')\right\rangle_{\Omega'} &= \left\langle T(\hat{\boldsymbol{n}})\right\rangle_{\Omega}\left(1-\frac{1}{2}\beta^2\right)-\frac{1}{3}\boldsymbol{\beta}\cdot\boldsymbol{d}+\frac{1}{3}\beta^2\left\langle T(\hat{\boldsymbol{n}})\right\rangle_{\Omega}+\left\langle(\boldsymbol{\beta}\cdot\hat{\boldsymbol{n}})^2\,Q(\hat{\boldsymbol{n}})\right\rangle_{\Omega}+\ldots \\ &= \left\langle T(\hat{\boldsymbol{n}})\right\rangle_{\Omega}\left(1-\frac{1}{6}\beta^2\right)-\frac{1}{3}\boldsymbol{\beta}\cdot\boldsymbol{d}+\left\langle(\boldsymbol{\beta}\cdot\hat{\boldsymbol{n}})^2\,Q(\hat{\boldsymbol{n}})\right\rangle_{\Omega}+\ldots \qquad \text{(C.10)}\end{aligned}$$

Note this formula is entirely general, i.e., no assumptions on $T(\hat{\boldsymbol{n}})$ have been made. Here the ellipsis represents octupole and higher ℓ multipoles and since $T(\hat{\boldsymbol{n}})$ is generic these terms are not necessarily small. However, for our LTB and Szekeres models only the monopole and dipole (and to a lesser extent the quadrupole) are significant so we have not explicitly included these in the expansions above.

In the case of our models, we have $|\boldsymbol{d}| \sim 1\,\mathrm{mK}$ and $Q(\hat{\boldsymbol{n}}) \sim 1\,\mu\mathrm{K}$ and so the term $\left\langle(\boldsymbol{\beta}\cdot\hat{\boldsymbol{n}})^2\,Q(\hat{\boldsymbol{n}})\right\rangle_{\Omega}$, while not zero, is very small ($\sim 10^{-12}\,\mathrm{K}$). This term can therefore be dropped, furnishing the final expression (4.61), relating the monopole temperature in the boosted frame with that in the unboosted frame.

Appendix D

Spherical harmonics and the Wigner 3j symbols

For the purposes of keeping this thesis as self-contained as possible we list the spherical harmonics needed in Chapter 4:

$$Y_{00}(\theta,\phi) = \frac{1}{\sqrt{4\pi}}, \tag{D.1}$$

$$Y_{10}(\theta,\phi) = \sqrt{\frac{3}{4\pi}}\cos\theta, \tag{D.2}$$

$$Y_{20}(\theta,\phi) = \frac{1}{4}\sqrt{\frac{5}{\pi}}(3\cos^2\theta - 1), \tag{D.3}$$

$$Y_{30}(\theta,\phi) = \frac{1}{4}\sqrt{\frac{7}{\pi}}(5\cos^3\theta - 3\cos\theta), \tag{D.4}$$

and

$$Y_{1-1}(\theta,\phi) = \sqrt{\frac{3}{8\pi}}\,\mathrm{e}^{-i\phi}\sin\theta, \tag{D.5}$$

$$Y_{11}(\theta,\phi) = -\sqrt{\frac{3}{8\pi}}\,\mathrm{e}^{i\phi}\sin\theta. \tag{D.6}$$

D.1 Wigner 3j symbols

We give here some elementary properties of the Wigner 3j symbols (see [184] for more details). The Wigner 3j symbols are related to the Clebsch-Gordan coefficients as follows:

$$\begin{pmatrix} \ell_1 & \ell_2 & \ell_3 \\ m_1 & m_2 & -m_3 \end{pmatrix} \equiv \frac{(-1)^{\ell_1-\ell_2+m_3}}{\sqrt{2\ell_3+1}}\langle \ell_1 m_1 \ell_2 m_2 | (\ell_1\ell_2)\ell_3 m_3\rangle. \tag{D.7}$$

They are non-zero if all of the following conditions hold:

(i) $\ell_1+\ell_2+\ell_3$ is a non-negative integer;

(ii)

$$|m_1| \leq \ell_1, \quad |m_2| \leq \ell_2, \quad |m_3| \leq \ell_3; \tag{D.8}$$

(iii)

$$m_1 + m_2 = m_3; \tag{D.9}$$

(iv)

$$|\ell_1 - \ell_2| \leq \ell_3 \leq \ell_1 + \ell_2. \tag{D.10}$$

They have the following properties. Under an even permutation of columns:

$$\begin{pmatrix} \ell_1 & \ell_2 & \ell_3 \\ m_1 & m_2 & m_3 \end{pmatrix} = \begin{pmatrix} \ell_2 & \ell_3 & \ell_1 \\ m_2 & m_3 & m_1 \end{pmatrix} = \begin{pmatrix} \ell_3 & \ell_1 & \ell_2 \\ m_3 & m_1 & m_2 \end{pmatrix}. \tag{D.11}$$

Under an odd permutation of columns:

$$\begin{pmatrix} \ell_1 & \ell_2 & \ell_3 \\ m_1 & m_2 & m_3 \end{pmatrix} = (-1)^{\ell_1+\ell_2+\ell_3} \begin{pmatrix} \ell_2 & \ell_1 & \ell_3 \\ m_2 & m_1 & m_3 \end{pmatrix} \tag{D.12}$$

$$= (-1)^{\ell_1+\ell_2+\ell_3} \begin{pmatrix} \ell_1 & \ell_3 & \ell_2 \\ m_1 & m_3 & m_2 \end{pmatrix}. \tag{D.13}$$

Sign inversion:

$$\begin{pmatrix} \ell_1 & \ell_2 & \ell_3 \\ -m_1 & -m_2 & -m_3 \end{pmatrix} = (-1)^{\ell_1+\ell_2+\ell_3} \begin{pmatrix} \ell_1 & \ell_2 & \ell_3 \\ m_1 & m_2 & m_3 \end{pmatrix}. \tag{D.14}$$

Formulae for Wigner 3j symbols are in general complicated. However, in the special case $m_1 = m_2 = m_3 = 0$ and $\ell_1 + \ell_2 + \ell_3$ is even the formula is relatively simple:

$$\begin{pmatrix} \ell_1 & \ell_2 & \ell_3 \\ 0 & 0 & 0 \end{pmatrix} = (-1)^{-(\ell_1+\ell_2+\ell_3)/2} \frac{\left(\frac{\ell_1+\ell_2+\ell_3}{2}\right)!}{\left(\frac{-\ell_1+\ell_2+\ell_3}{2}\right)! \left(\frac{\ell_1-\ell_2+\ell_3}{2}\right)! \left(\frac{\ell_1+\ell_2-\ell_3}{2}\right)!}$$

$$\times \sqrt{\frac{(-\ell_1+\ell_2+\ell_3)!(\ell_1-\ell_2+\ell_3)!(\ell_1+\ell_2-\ell_3)!}{(\ell_1+\ell_2+\ell_3+1)!}}. \tag{D.15}$$